Spring 2007

Formation of RDX nanoparticles by rapid expansion of supercritical solution : in situ characterization by laser scattering

Takuya Matsunaga
New Jersey Institute of Technology

ABSTRACT

FORMATION OF RDX NANOPARTICLES BY RAPID EXPANSION OF SUPERCRITICAL SOLUTION: *IN SITU* CHARACTERIZATION BY LASER SCATTERING

by
Takuya Matsunaga

Cyclo-1,3,5-trimethylene-2,4,6-trinitramine (RDX), a well-known energetic material, is highly explosive. Reduction of the sensitivity of RDX is desired for safe handling and storage in military applications. Data on the sensitivity of RDX in the 10-1000 μm crystal size range suggested that the impact sensitivity could be further reduced by reduction of the crystal size to the sub-micron or nano-scale (Armstrong, 1990). Recent research with nano-RDX obtained using Rapid Expansion of Supercritical Solutions (RESS) confirmed these expectations (Stepanov, 2005).

RESS process appeared to be one out of a few techniques of production of nano-scale energetic materials free of the risk of explosion. Current research was aimed at the understanding of the fundamentals of the RESS process and the mechanism of nanoparticle formation via an *in situ* particle monitoring and characterization in the RESS jet combined with the characterization of the final product.

In this research, nanoparticles of RDX generated by RESS using supercritical CO_2 were characterized *in situ* by a pulse laser light scattering imaging technique using gated ICCD camera. The sensitivity was determined using Rayleigh scattering from air as well as light scattering from standard polystyrene spheres. The size distribution functions of the particles formed in the RESS jet were determined using the calibrated sensitivity. The final diameter of RDX particles at the pre-expansion pressure of 180 bar was 73 nm at the

maximum of the size distribution function. Assuming that the particles near the nozzle consisted mainly of CO_2 and the log-normal size distribution, the diameter of the particles near the nozzle (7.5 mm from the nozzle) at the distribution maximum was 3.3 μm at the pre-expansion pressure of 180 bar. The number densities of the particles in the RESS jet were determined by counting individual particles in the light scattering images. Based on the measured particle size distributions and the number density of particles along the RESS jet, the mechanism of particle formation in the RESS is discussed. The homogeneous nucleation mechanism is rejected as it fails to explain the large particle size experimentally observed. Instead, a modified "spray-drying" mechanism is suggested.

FORMATION OF RDX NANOPARTICLES BY RAPID EXPANSION OF SUPERCRITICAL SOLUTION: *IN SITU* CHARACTERIZATION BY LASER SCATTERING

by
Takuya Matsunaga

A Dissertation
Submitted to the Faculty of
New Jersey Institute of Technology
in Partial Fulfillment of the Requirements for the Degree of
Doctor of Philosophy in Materials Science and Engineering

Interdisciplinary Program in Materials Science and Engineering

May 2007

APPROVAL PAGE

FORMATION OF RDX NANOPARTICLES BY RAPID EXPANSION OF SUPERCRITICAL SOLUTION: *IN SITU* CHARACTERIZATION BY LASER SCATTERING

Takuya Matsunaga

Dr. Lev N. Krasnoperov, Dissertation Advisor — Date
Professor, Department of Chemistry and Environmental Science, NJIT

Dr. Haim Grebel, Committee Member — Date
Professor, Department of Electrical and Computer Engineering, NJIT

Dr. Zafar Iqbal, Committee Member — Date
Research Professor, Department of Chemistry and Environmental Science, NJIT

Dr. Frank J. Owens, Committee Member — Date
Senior Research Scientist, Armament Research, Development and Engineering Center, Picatinny, New Jersey

Dr. Leonid Tsybeskov, Committee Member — Date
Associate Professor, Department of Electrical and Computer Engineering, NJIT

BIOGRAPHICAL SKETCH

Author: Takuya Matsunaga

Degree: Doctor of Philosophy

Date: May 2007

Undergraduate and Graduate Education:

- Doctor of Philosophy in Materials Science and Engineering, New Jersey Institute of Technology, Newark, NJ, 2007
- Master of Science in Materials Engineering, University of Wisconsin-Milwaukee, Milwaukee, WI, 1999
- Master of Science in Biological Science, Hokkaido University, Sapporo, Japan, 1996
- Bachelor of Science in Polymer Science, Hokkaido University, Sapporo, Japan, 1994

Major: Materials Science and Engineering

Publications and Presentations:

T. Matsunaga, A. V. Chernyshev, E. N. Chesnokov, and L. N. Krasnoperov, "*In situ* optical monitoring of RDX nanoparticles formation during rapid expansion of supercritical CO_2 solutions", Physical Chemistry Chemical Physics (to be submitted).

T. Matsunaga, A. Chernyshev, L. Krasnoperov, "*In situ* optical characterization of nanoparticles in the RESS process", in *25th Regional Meeting on Kinetics and Dynamics*, Albany, 2007.

T. Matsunaga, A. V. Chernyshev, L. N. Krasnoperov, "Formation of nanoparticles by rapid expansion of supercritical solutions: *In situ* characterization by laser scattering", in *6th International Conference on Chemical Kinetics*, Gaithersburg, 2005.

T. Matsunaga, A. Chernyshev, L. Krasnoperov, "Formation of nano-particles by rapid expansion of supercritical solutions: *In situ* characterization by laser scattering", in *37th American Chemical Society Mid-Atlantic Regional Meeting*, Piscataway, 2005.

To my wife, Shuyan, who gives me love, support, and encouragement.

To my daughter, Mari, who makes my everyday life happy and colorful.

To my parents, Tsuyoshi and Emiko, who have showed me their endless love and support throughout my life.

ACKNOWLEDGEMENT

I wish to express my sincere gratitude to my advisor, Dr. Lev N. Krasnoperov, for his invaluable guidance, enthusiastic encouragement, and precious advice. His knowledge and insight guided me throughout my doctoral research and gave me countless valuable lessons. I also wish to give my thanks to Dr. Andrei Chernyshev, Dr. Evgeni Chesnokov, and Dr. Inga Elkina for their technical support and helpful discussions.

I am greatly thankful to Dr. Haim Grebel, Dr. Zafar Iqbal, Dr. Frank J. Owens, and Dr. Leonid Tsybeskov for their efforts and valuable comments as members of the committee. It is my honor to have them as my committee members. I am very grateful to Dr. Xueyan Zhang for evaluating my samples by TEM imaging. My special thanks go to Victor Stepanov and other graduate / undergraduate students in the group for the warm friendship.

At last, I am very thankful to the teaching assistantship from NJIT, which financially supported me for completing my 4-year graduate study, and the US Army project (DAAE30-02-C-1140) for financial support during summers.

TABLE OF CONTENTS

TABLE OF CONTENTS
(Continued)

TABLE OF CONTENTS
(Continued)

TABLE OF CONTENTS
(Continued)

TABLE OF CONTENTS
(Continued)

LIST OF TABLES

LIST OF FIGURES

LIST OF FIGURES
(Continued)

LIST OF FIGURES
(Continued)

LIST OF FIGURES
(Continued)

LIST OF FIGURES
(Continued)

CHAPTER 1

INTRODUCTION

1.1 Energetic Materials

1.1.1 Explosives

"Explosives" can be defined broadly as energetic materials that can react chemically accompanied with heat, light and gas emission,[1] but in order to distinguish explosives from propellants, it is better to narrow the definition of explosives as the energetic materials that can detonate. Some of the most common pure explosives are TNT (2,4,6-Trinitrotoluene), RDX (Cyclo-1,3,5-trimethylene-2,4,6-trinitramine), and HMX (Cyclotetramethylene-tetranitramine). Although these compounds in pure form are used in some applications, in most cases they are mixed with other energetic materials to improve their properties or processibility that are not achievable using the pure materials. As an example of such explosive formulations, Composition B is a blend of 60 % RDX and 40 % TNT.

Although some explosive energetic materials are used as propellants, generally speaking, propellants burn but should not detonate. Propellants differ from explosives in that the reaction rates (burn rates) of propellants are very low compared to the reaction rates (detonation rates) of explosives. Propellants also produce gas and heat during the reaction as explosives do.

1.1.2 Initiation

Initiation, a process of starting a detonation (or burning) reaction, takes place once the reaction becomes self-sustaining. The process is explained by so-called "hot-spot theory".[1] Consider an energetic material that is locally heated. The material decomposes at this point. Locally, temperature rises due to the heat generated from the decomposition reaction if the heat generation is faster than the heat transfer into the surrounding. Increased temperature accelerates the reaction (increases the reaction rate) causing it self-sustainable.

The self-sustained reaction propagates through the material with certain rate depending upon physical properties of the materials including density, particle (or crystal) size and porosity, temperature, pressure, etc. Once the propagation rate reaches shock velocity, the process undergoes transition from deflagration to detonation. Detonation can be also caused by a shock wave. An incident shock wave compresses the explosive and causes a chemical reaction. If the initial shock is imposed with high pressure and long duration, it initiates detonation.

There are several sensitivity testing methods for impact as well as thermal and electrical initiation. Drop-weight test is one of the common tests for impact initiation.[1] A weight is dropped from a certain height on a sample of energetic material. The height at which initiation occur in 50 % of tests (H_{50}) serves as a measure of the material impact sensitivity. The larger H_{50} is, the lower the sensitivity.

1.1.3 Crystal Size Dependence of Sensitivity for Impact Initiation

Heavens and Field[2] studied the behavior of thin layer of explosives under drop-weight impact using a combination of high speed photographic imaging and measuring pressure-time profiles. In this research the sharp pressure drop was observed when the plastic deformation occurred, and at the same time the formation of hot spots leading to ignition of explosives was expected. Such a load drop behavior is associated with pile-up of dislocations in explosive crystals.[3] This is called "the dislocation pile-up avalanche model". Under loading conditions dislocation movement is brought about by shear stress and, when the critical point is reached, catastrophic failure of crystal occurs at the dislocation pile-up. Figure 1.1 is an illustration of the stress-time curve. The critical shear stress τ_c is implicitly determined by the following formula[4]:

$$\tau_2 = \tau_0 + l^{-1/2}\left(c\sqrt{G\tau_c b}\right) \tag{1.1}$$

where τ_0 is the shear stress required for intrinsic dislocation movement, τ_2 is defined in Figure 1.1, c is a numerical constant, G is the shear modulus, b is the dislocation Burgers vector, and l is the dislocation slip length.

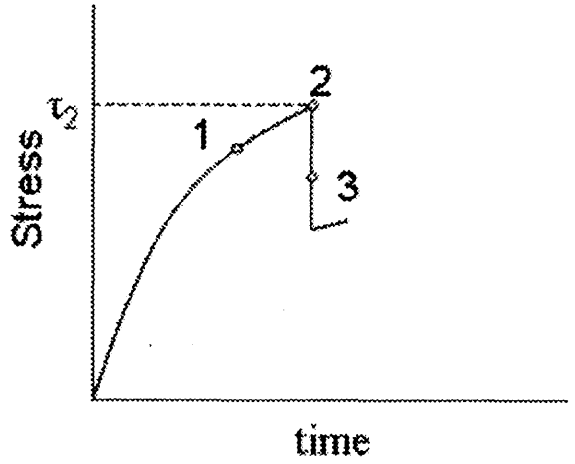

Figure 1.1 Illustration of stress-time curve for explosives.

Armstrong[4,5] investigated the drop-weight impact sensitivity as a function of $l^{-1/2}$ assuming the dislocation slip length l to be the crystal particle size. Figure 1.2 presents the drop-height for 50 % probability of initiation of RDX. It was clearly shown that the impact sensitivity was lowered by the size reduction of explosive crystals down to 10 μm diameter. Since lowering the sensitivity of highly explosive materials such as RDX are often desired in military pursuing safe handling of explosive weapons, further reduction of the crystal size is of great interest.

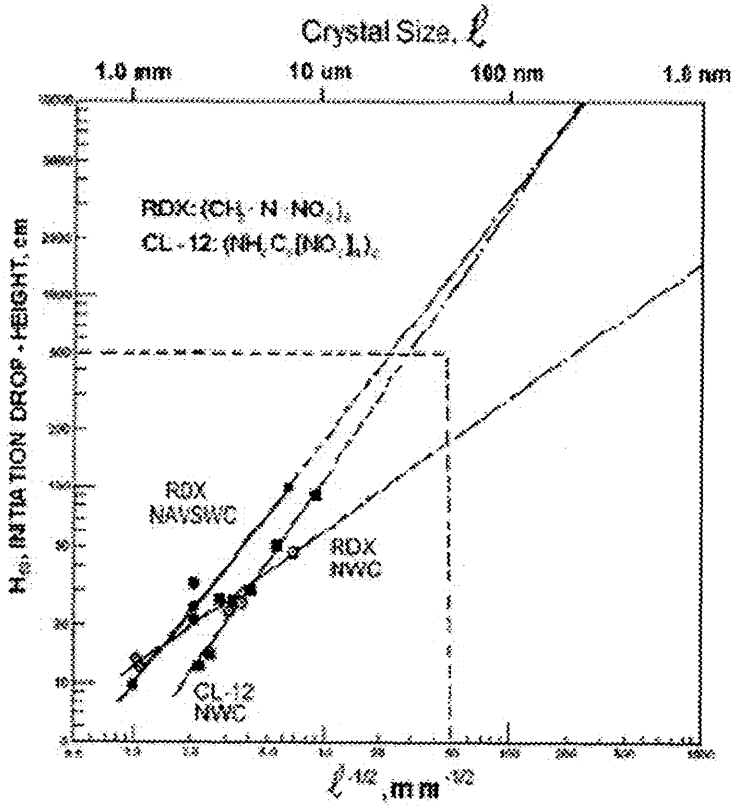

Figure 1.2 The drop-weight impact sensitivity of RDX as a function of $l^{-1/2}$.[4]

Stepanov et al.[6] investigate the impact sensitivity of nanocrystalline RDX of about 100 nm diameter by the drop weight test (H50). The reduction of the impact sensitivity of the nano-RDX crystals by more than a factor of five compared to class-5 RDX crystals was confirmed.

1.1.4 Size Reduction of Crystals

Crystal size reduction of explosives is usually achieved using appropriate milling or grinding methods. The processing should be performed under wet conditions because of safety requirement. Colloid mill, jet mill, ultrasonic grinding, rotor stator dispersing system, and annular gap mill have been used for size reduction of RDX crystals.[5] The typical final crystal size obtained by these techniques ranged from 1 to 10 μm in diameter. However, it appeared to be quite difficult to reduce the crystal size down to submicron level and obtain uniform size and shape by means of the mechanical processing.

1.2 Supercritical Fluid Technology for Particle Formations

1.2.1 Particle Formation from Supercritical Solutions

There is another possible approach to create submicron crystals of energetic materials, based on supercritical fluids. The supercritical fluid processing is a common technology to produce submicron to micron particles especially in the pharmaceutical,[7-9] nutraceutical, cosmetic, polymer[10,11] and some other chemical industries.[12,13] There are several types of techniques for particle formation using the supercritical fluid processing:[12] Rapid Expansion of Supercritical Solutions (RESS), Supercritical Anti-Solvent Process (SAS), Particles from Gas-Saturated Solutions/Suspensions (PGSS),

Aerosol Solvent Extraction System (ASES), and Solution Enhanced Dispersion by Supercritical Fluid (SEDS).

In the RESS process, a solvent must be highly pressurized to become a supercritical state at certain temperature and achieve sufficient solubility of a substance. Then the supercritical solution is rapidly depressurized via expansion through a nozzle. After depressurized, the solvent evaporates leaving the solute particles. In the SAS process, the supercritical fluid is added to a solution of the substance in order to decrease solubility in a solvent causing precipitation or recrystallization of the solute. The PGSS process consists of dissolving a supercritical fluid in a melted substance or a solution or suspension of the substance and depressurizing the mixture through a nozzle. In this process a variety of materials can be used to form the particles, even for polymeric materials which are not soluble in the supercritical fluid. The ASES process consists of spraying the solution from a nozzle as fine droplets into a supercritical fluid and dissolving the supercritical fluid into the droplets accompanied by a volume expansion of the droplets and solubility drop of the substance. In the SEDS process a mixture of the solution and supercritical fluid is expanded through a nozzle. In this process, the supercritical fluid works as "spray enhancer" to break up the solution into very small droplets, compared to the droplet size in the ASES process.

1.2.2 Application of Supercritical Fluid Technology to Energetic Materials

Compared to application of supercritical fluid technology to pharmaceutical materials, relatively small number of publications is available for the application to energetic materials. Pourmortazavi et al.[14] reviewed the research on the applications of supercritical

fluids to energetic material processing. RESS and SAS processes have been used for production of energetic materials.[15-20] SAS have been used for production of RDX particles utilizing the low solubility in supercritical CO_2 compared to the solubility in common organic solvents such as acetone, acetonitrile, nitroethane, and dimethyl sulfoxide. Gallagher et al.[15] used SAS process with various organic solvents to produce RDX crystals and to study the crystal shape and morphology. In these experiments, the crystal size was typically about 100 μm. The crystal shape varied as plates-like, needles-like, cubic, etc., depending upon the solvent used.

1.2.3 Rapid Expansion of Supercritical Solutions (RESS)

1.2.3.1 Theoretical Model of RESS Process and Particle Formation. Theoretical studies of particle formation by RESS process have been performed over the last 15 years.[21-29] The main aim of the theoretical studies was in the prediction of the particle size and the particle size distribution. Debenedetti and co-workers published the first comprehensive theoretical work for particle formation by the RESS process. In 1993, Kwauk and Debenedetti[22] presented a mathematical model of the nucleation and particle formation by RESS process. They calculated the particle size of phenanthrene formed by RESS from a subsonic converging nozzle. The trend of the particle size with the process parameters was predicted using this model: the particle size increases upon increasing the pre-expansion temperature and the particle size decreases upon increasing the extraction temperature and pressure. The nucleation and condensation of the solute were considered for the particle formation in the model. Coagulation associated with Brownian motion

was negligible according to the authors. The calculations suggest that the partial expansion lead to the mean particle sizes in the range of 15-50 nm.

In contrast to Kwauks' work, Shaub et al.[24] considered the flow in the supersonic free jet. They treated the adiabatic expansion of phenanthrene-CO_2 system into vacuum. The calculations showed that small particles (1.8 nm) can be achieved by operating the expansion at relatively low pre-expansion pressure of 14 MPa and pre-expansion temperature of 550 K. The basic trends could be predicted by these calculations. However, due to the lack of the experimental data in the range of the conditions used in both Kwauk and Shaub's studies at the time, these models could not be compared with the experiment.

Weber et al.[27] studied homogeneous nucleation and the growth of particles formed by RESS. The results of their simulations show that phenanthrene particles in subsonic capillaries with the length shorter than 1 m cannot be larger than 100 nm (number-based mean diameter), suggesting that the micron size particles, commonly observed in the RESS experiments, must grow in the transonic regions of the free jet. The subsequent growth of the particles along the free jet is driven by the condensation and coagulation processes. The coagulation was calculated based on the collision frequency associated with Brownian motion, and laminar and turbulent shear forces.[30,31]

Helfgen et al.[28] presented the theoretical model of the RESS process and the comparison with the experimental results. The simulations in their paper consist of the flow field modeling and the nucleation/growth modeling for solution of benzoic acid and griseofulvin. The one dimensional, steady-state flow field model which consists of mass, momentum and energy balance and the Bender Equation of state, produced the pressure

and temperature profiles along the expansion stream. These profile data were used for modeling of particle formation and growth. In the particle formation and growth model, the homogeneous nucleation was assumed and the growth by condensation and coagulation was taken into accounts. The particle sizes resulting from the simulations (ca. 800 nm for benzoic acid) were much larger than the experimentally observed (ca. 300 nm).

In spite of numerous attempts of modeling the RESS process, none of them was able to predict the particle sizes precisely consistent with experiment. The reason for this discrepancy is not established with certainty yet. It should be noted, however, that the experimental approaches used in the studies are open to criticism. In the majority of the studies, SEM (Scanning Electron Microscopy) characterization of particles collected as the final product was used for the determination of particle size, although some *in situ* characterization methods have been also suggested.

1.2.3.2 Characterization of RESS Process and Particles Formed by RESS. SEM is the most common method to characterize particles with respect to size, shape, and morphology. However, uniform collection (without the size discrimination) of particles from the RESS jet is questionable, because there could be difficulties in efficient collection of very small particles (below 100 nm in diameter). Then the particle size distributions determined from SEM are questionable, too. There are several techniques used for the *in situ* characterization of the RESS process such as the three-wavelength-extinction measurement (3-WEM),[28,29,32-34] Fourier transform infrared (FTIR) spectroscopy,[33,34] and the laser-based shadowgraphy (LABS).[32] In the 3-WEM technique the extinction of incident light due to the light scattering by the particles is measured

using three different wavelengths. Then, the particle size and the particle number density were estimated assuming a particular size distribution function. FTIR is a useful technique for investigating chemical compositions in the RESS jet. However, both 3-WEM and FTIR techniques can provide only rough estimates of the particle size and the number density because these techniques rely upon the assumption of particular shape of the size distribution functions. Moreover, the light scattering by the turbulent flow of CO_2 interferes with the measurements of scattered light from the particles. The LABS produces a magnified shadowgraph picture of individual particles. The particle size is determined by measuring the size of the shadow spots in the images. While in this technique *in situ* observation even of the shape of large particles is possible, small particles (with the diameters less than the wavelength of the incident light) cannot be monitored.

1.2.3.3 New Approach for the *In Situ* Characterization. In this study the *in situ* optical characterization for particle formation in RESS was developed by combining the light scattering with an imaging technique. In this approach the particle size detection limit is better than in the LABS, and the approach overcomes the weaknesses of the 3-WEM and FTIR. In the method, individual spots corresponding to light scattered from individual particles are processed to determine their integral intensities and, subsequently, particle sizes. The size distribution functions can be determined without an *a priori* assumption about their shapes. Another advantage is that the imaging technique differentiates scattering by particles from scattering by other sources such as turbulent flow of carbon dioxide. Using this direct approach, more reliable distribution functions can be obtained.

1.3 Objectives of Research

In the beginning of this chapter, the importance of crystal size reduction of energetic materials was described. This was the main reason why RESS and other supercritical fluid techniques have been attractive particularly to people who participate in science of energetic materials in military organizations. On the other hand, there is not sufficient experimental information available for understanding the particle formation during the RESS process and for the development of a reliable model for the particle formation. Using only the characterization of the final product, the particle formation mechanism in the RESS could be hardly understood due to the possible sampling size discrimination for the final product analysis. The mechanism of particle formation is required for the process development and optimization. Therefore, *in situ* characterization methods are to be designed. Such methods are expected to provide useful information for the development of reliable models of particle formation in the RESS process.

CHAPTER 2

LIGHT SCATTERING IMAGING SYSTEM

2.1 Theoretical Background of Light Scattering

2.1.1 Introduction

Blue sky, the yellow sun, and red sunset, all are phenomena as consequences of light scattering. The variation of color is due to a scattering from atmosphere and its dependence on wavelength such that the shorter wavelength light scatters more than the longer wavelength light. Blue scattered light in the sky and yellow light directly from the sun are observed. Because sun light in the evening has longer path than at day time, it has more chances to be scattered out by atmosphere and, therefore, the color becomes reddish.

Light scattering is a consequence of interaction of electromagnetic wave with matter. The electromagnetic wave invokes the dipole oscillation inside the matter at the same frequency as the incident field, resulting in secondary radiation. Such scattering from small particles (much smaller than the wavelength of the incident light) or molecules is called Rayleigh scattering.[35] The Rayleigh scattering theory could be derived as an approximation of the generalized scattering theory for small particle size, which is known as the Mie (scattering) theory.[36] The Mie theory provides an analytical solution of the Maxwell Equations for scattering from a spherical particle.

2.1.2 Stokes Parameters and Scattering Matrix

Stokes parameters[37] are a useful description of polarized light especially in light scattering problems. There are four elements in stokes parameters including the total irradiance (I), horizontally and vertically polarized components (Q), ± 45° polarized components (U), and circular polarized components (V). Consider the electric field **E** as

$$\mathbf{E} = \mathbf{E}_0 \exp\{i(\mathbf{k} \cdot x - wt)\} \tag{2.1}$$

where

$$\mathbf{E}_0 = E_{\parallel}\hat{\mathbf{e}}_{\parallel} + E_{\perp}\hat{\mathbf{e}}_{\perp} \tag{2.2}$$

Each of stokes parameter is expressed as follows:

$$I = E_{\parallel}E_{\parallel}^{*} + E_{\perp}E_{\perp}^{*} \tag{2.3}$$

$$Q = E_{\parallel}E_{\parallel}^{*} - E_{\perp}E_{\perp}^{*} \tag{2.4}$$

$$U = E_{\parallel}E_{\perp}^{*} + E_{\perp}E_{\parallel}^{*} \tag{2.5}$$

$$V = i(E_{\parallel}E_{\perp}^{*} - E_{\perp}E_{\parallel}^{*}) \tag{2.6}$$

The stokes parameters for different polarizations are listed in Table 2.1.

Table 2.1 Stokes Parameters for Polarized Light

Unpolarized	Linearly polarized				Circularly polarized	
	0°	90°	45°	-45°	Right	Left
$\begin{pmatrix}1\\0\\0\\0\end{pmatrix}$	$\begin{pmatrix}1\\1\\0\\0\end{pmatrix}$	$\begin{pmatrix}1\\-1\\0\\0\end{pmatrix}$	$\begin{pmatrix}1\\0\\1\\0\end{pmatrix}$	$\begin{pmatrix}1\\0\\-1\\0\end{pmatrix}$	$\begin{pmatrix}1\\0\\0\\1\end{pmatrix}$	$\begin{pmatrix}1\\0\\0\\-1\end{pmatrix}$

The amplitude of the scattered field from a particle is a linear function of the amplitude of the incident field, because the tangential components of **E** (and also magnetic field **H**) are continuous across the boundary between particle and medium.[36] Therefore, the amplitude of the scattered field can be written in matrix form

$$\begin{pmatrix} E_{\parallel s} \\ E_{\perp s} \end{pmatrix} = \frac{e^{ikr}}{-ikr} \begin{pmatrix} S_2 & S_3 \\ S_4 & S_1 \end{pmatrix} \begin{pmatrix} E_{\parallel i} \\ E_{\perp i} \end{pmatrix} \tag{2.7}$$

where k is the wave number in the medium. The 2 × 2 matrix in Equation 2.7 is called the amplitude scattering matrix, which is dependent on scattering angles. For spheres, the elements S_3 and S_4 are zero for any angle.

On the other hand, the stokes vector of the scattered light (I_s, Q_s, U_s, V_s) can be represented by using the 4 × 4 matrix, so called scattering matrix,[36] as

$$\begin{pmatrix} I_s \\ Q_s \\ U_s \\ V_s \end{pmatrix} = \frac{1}{k^2 r^2} \begin{pmatrix} S_{11} & S_{12} & S_{13} & S_{14} \\ S_{21} & S_{22} & S_{23} & S_{24} \\ S_{31} & S_{32} & S_{33} & S_{34} \\ S_{41} & S_{42} & S_{43} & S_{44} \end{pmatrix} \begin{pmatrix} I_i \\ Q_i \\ U_i \\ V_i \end{pmatrix} \tag{2.8}$$

Based on the definition of I in Equation 2.3 and Equation 2.7, S_{11} and S_{12} are written as

$$S_{11} = \frac{1}{2}\left(|S_1|^2 + |S_2|^2 + |S_3|^2 + |S_4|^2\right) \tag{2.9}$$

and

$$S_{12} = \frac{1}{2}\left(|S_2|^2 - |S_1|^2 + |S_4|^2 - |S_3|^2\right) \tag{2.10}$$

Since unpolarized laser light is used in this research, the stokes vector of incident light is (1 0 0 0). Therefore, only the element S_{11} of the scattering matrix is important to obtain the information of scattered light such as differential scattering cross section.

2.1.3 Scattering by a Sphere

The Mie theory gives the exact solution for the light scattering problem, which is an electromagnetic field of scattered light from a sphere (see APPENDIX A).[36] According to the Mie theory, the elements of the amplitude scattering matrix in Equation 2.7 are given by

$$S_1 = \sum_n \frac{2n+1}{n(n+1)}(a_n\pi_n + b_n\tau_n) \tag{2.11}$$

and

$$S_2 = \sum_n \frac{2n+1}{n(n+1)}(a_n\tau_n + b_n\pi_n) \tag{2.12}$$

where

$\pi_n = \frac{P_n^1}{\sin\theta}$, and $\tau_n = \frac{dP_n^1}{d\theta}$. P_n^1 is the first order associated Legendre function. a_n and b_n are known as the scattering coefficients, which are

$$a_n = \frac{\mu m^2 j_n(mx)[xj_n(x)]' - \mu_1 j_n(x)[mxj_n(mx)]'}{\mu m^2 j_n(mx)[xh_n^{(1)}(x)]' - \mu_1 h_n^{(1)}(x)[mxj_n(mx)]'} \tag{2.13}$$

and

$$b_n = \frac{\mu_1 j_n(mx)[xj_n(x)]' - \mu j_n(x)[mxj_n(mx)]'}{\mu_1 j_n(mx)[xh_n^{(1)}(x)]' - \mu h_n^{(1)}(x)[mxj_n(mx)]'} \tag{2.14}$$

where μ and μ_1 are the permeability of medium and particle, x is the size parameter and m is the relative index of refraction given by

$$x = \frac{2\pi N_1 a}{\lambda} \tag{2.15}$$

and

$$m = \frac{N_1}{N_2} \tag{2.16}$$

N_1 and N_2 are the indices of refraction of particle and medium, respectively. In Equation 2.15, a is the radius of particle. $j_n(x)$ is written as

$$j_n(x) = \sqrt{\frac{\pi}{2x}} J_{n+1/2}(x) \tag{2.17}$$

where $J(x)$ is the spherical Bessel function of the first kind. The spherical Bessel functions of the third kind (spherical Hankel function) $h_n(x)$ have a relationship with the spherical Bessel functions of the first and second kinds as

$$h_n^{(1)}(x) = j_n(x) + iy_n(x) \tag{2.18}$$

and

$$h_n^{(2)}(x) = j_n(x) - iy_n(x) \tag{2.19}$$

where $y_n(x)$ is the spherical Bessel function of the second kind.

2.1.4 Differential Scattering Cross Section

The differential scattering cross section is defined as the energy scattered per unit time into a unit solid angle which can be specified by two angles, the polar θ and azimuthal angle φ. Using the incident and scattered irradiance I_i and I_s, the differential scattering cross section is written as

$$\frac{dC_{sca}}{d\Omega} = \frac{r^2 I_s}{I_i} \tag{2.20}$$

If the incident light is unpolarized, using Equation 2.8,

$$\frac{dC_{sca}}{d\Omega} = \frac{S_{11}}{k^2} \tag{2.21}$$

Since the elements of the amplitude scattering matrix S3 and S4 are zero for a sphere, the differential scattering cross section for a sphere is given by

$$\frac{dC_{sca}}{d\Omega} = \frac{1}{2k^2}\left(|S_1|^2 + |S_2|^2\right) \tag{2.22}$$

Figure 2.1 presents, as an example, the differential scattering cross section as a function of size of a solid CO_2 sphere. The Fortran program, Chiral,[38] downloadable from internet was used as a Mie scattering code. The complex indices of refraction for RDX and CO_2[39] were taken as $1.678 + 0.645i$ and $1.475 + 0i$, respectively (see APPENDIX B).

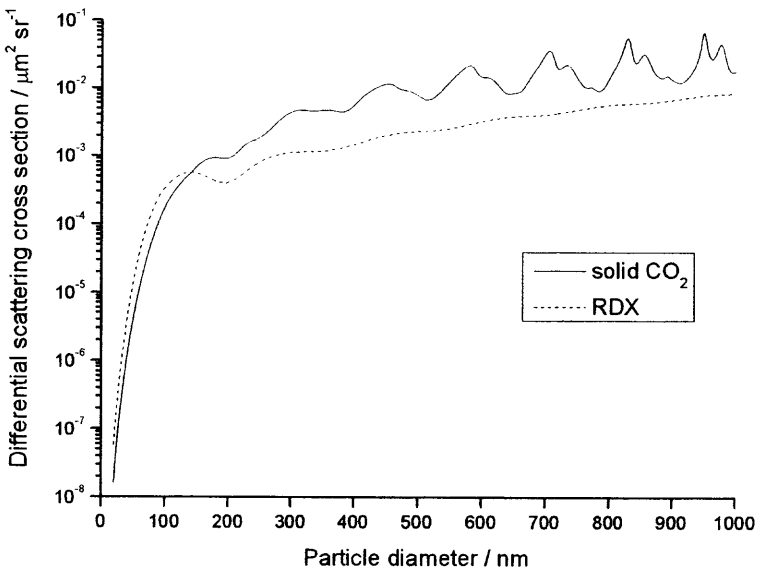

(a)

Figure 2.1 Differential scattering cross sections from spherical particles of solid CO_2 (solid line) and RDX (dashed line) at 90° to unpolarized incident light as a function of the particle diameter less than 1000 nm (a) and 10 μm (b).

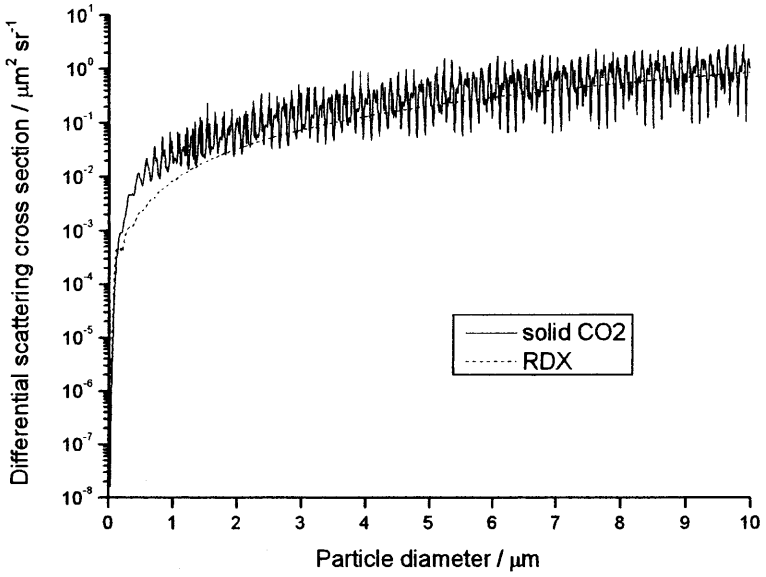

(b)

Figure 2.1 Differential scattering cross sections from spherical particles of solid CO_2 (solid line) and RDX (dashed line) at 90° to unpolarized incident light as a function of the particle diameter less than 1000 nm (a) and 10 μm (b).(Continued)

2.2 Principle of Imaging Scattered Light from a Particle

2.2.1 Introduction

The light scattering system developed in this research was combined with an imaging technique (ICCD camera) to probe individual particles present in the sampling volume. Since a spherical lens is used to project scattered light to the camera, the image of a point source is a circular spot of certain finite size depending on the optical geometry. The size of a spot is mainly controlled by spherical aberrations and diffraction. Spherical aberrations are inherent in optical systems using lens and become significant if the aperture of the lens increases. On the other hand, diffraction becomes significant if the

aperture size is reduced. Therefore, the optical system is optimized by balancing these two competing properties. Here the impact of the spherical aberrations on the resulting images and its correction was simulated, and the simulation results were compared with the images experimentally observed.

2.2.2 Fundamentals of Relevant Geometrical Optics

Consider a point source of light, a thin lens and the image plane. In this simple geometry, propagation of light (or wavefront) can be easily predicted if the refractive indices of the media are known. If the thin lens is thin enough and the surrounding medium is air, the famous equation for paraxial beams is derived as

$$\frac{1}{s_1}+\frac{1}{s_2}=(n_l-1)\left(\frac{1}{R_2}-\frac{1}{R_1}\right) \tag{2.23}$$

where n_l is the index of refraction of a lens material, R_1 and R_2 are radii of the lens surfaces, and s_1 and s_2 are the distances between the point source and the lens, and between the lens and the image plane. If s_1 is infinity (meaning that parallel light comes into the lens), the image distance s_2 becomes the focal length f. Similarly if s_2 is infinity, s_1 becomes f. Therefore, the right hand side of Equation 2.23 equals the reciprocal of f:

$$(n_l-1)\left(\frac{1}{R_2}-\frac{1}{R_1}\right)=\frac{1}{f} \tag{2.24}$$

and then

$$\frac{1}{s_1}+\frac{1}{s_2}=\frac{1}{f} \tag{2.25}$$

This is known as Gaussian lens formula.

However, the Gaussian lens formula does not always reflect the reality of lens optics. If the incident angle of rays near the center of the lens is so small that sine of the angle φ can be approximated as the angle itself. This is called the paraxial approximation or the first-order theory. Equation 2.25 can be applied only if the paraxial approximation is valid. On the other hand, the incident angle at the periphery of the lens may not be small enough to satisfy the paraxial approximation. In such a case, the sine of the angle φ can be approximated by the first several terms in the expansion,

$$\sin\varphi = \varphi - \frac{\varphi^3}{3!} + \frac{\varphi^5}{5!} - \frac{\varphi^7}{7!} + \cdots. \tag{2.26}$$

If the first two terms are taken for the approximation, there is the third-order theory to analyze the properties of geometrical optics including spherical aberrations, coma, astigmatism, and so on. In these properties, spherical aberration is the most important factor to design the optical system because the spot size (that is the size of the image of scattered light from a particle) is mainly determined by the spherical aberration of the lens. The details of the spherical aberrations will be discussed in the next section.

2.2.3 Simulation of Spot Size

2.2.3.1 Spot Size with a Single Lens. Simulation of spot size was done to optimize the geometry of the optical system. As described in section 2.2.2, the spot size is mainly limited by the spherical aberrations of the lens. Figure 2.2 shows longitudinal and lateral spherical aberrations of a thin lens. The distances a and b are related to f by the Gaussian lens formula. b' is a result of deviation from ideal (Gaussian optical) distance b.

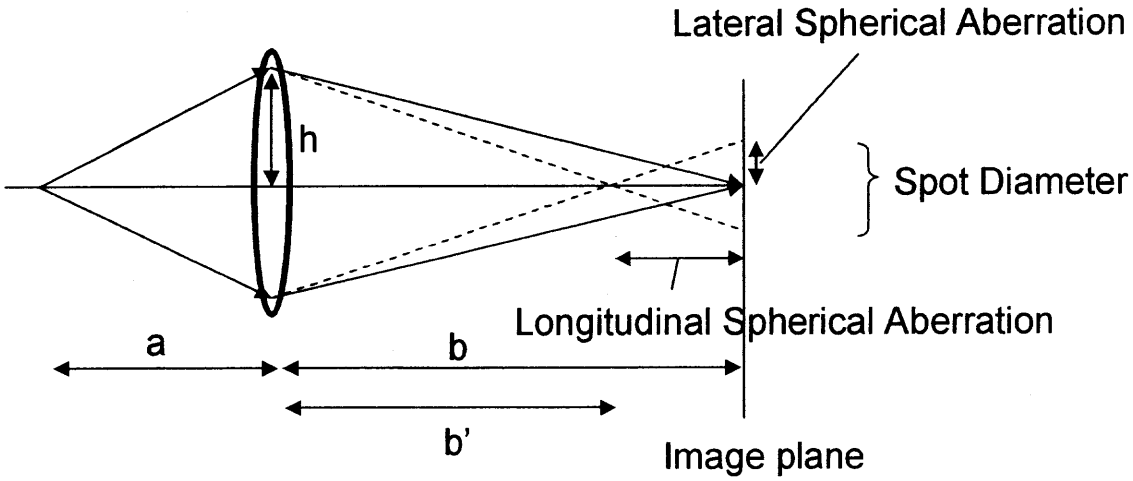

Figure 2.2 Longitudinal and lateral spherical aberrations of a thin lens.

Using the third-order theory in the approximation, the spherical aberration of the thin lens is given by[40]

$$\frac{1}{b'}-\frac{1}{b}=\frac{h^2}{8f^3}\frac{1}{n(n-1)}\left[\frac{n+2}{n-1}q^2+4(n+1)pq+(3n+2)(n-1)p^2+\frac{n^3}{n-1}\right] \tag{2.27}$$

where h is the radius of the aperture of the lens, n is the index of refraction of the lens, q is the shape factor of lens, and p is the position factor of lens. The longitudinal and lateral spherical aberrations are defined by

$$\text{Long. S. A.} \equiv b - b' \tag{2.28}$$

and

$$\text{Lateral S.A.} \equiv (b - b')\tan(\theta) \tag{2.29}$$

The lateral spherical aberration corresponds to the radius of the spot at the image plane. The shape factor q and the position factor p are given by

$$q = \frac{r_2 + r_1}{r_2 - r_1} \tag{2.30}$$

and

$$p = \frac{b - a}{b + a} \tag{2.31}$$

In this calculations, the shape factor q was taken as 0 for a symmetric double convex lens. Thus, the spot diameter d for a single ray can be written as

$$d = 2(b - b')\tan\theta = 2(b - b')\frac{h}{b'} \tag{2.32}$$

As b' is written as a function of h from Equation 2.27, d becomes a function of only h.

2.2.3.2 Circle of Least Confusion. As described above, h is the only variable for d if the positions of the lens and the camera are fixed. However, in order to achieve the best image, which is usually a smallest spot, the actual position of the image plane (that is the position of the photocathode of the camera) is optimized. The smallest spot is called the *Circle of least confusion.*

To calculate the size of the circle of least confusion denoted as α_{least}, a new variable b'' that is the position of the camera relative to the lens is introduced. The radius of the spot α at b'' is obtained as

$$\alpha = \left|(b'' - b')\tan(\theta)\right| = \left|h\left(\frac{b''}{b'} - 1\right)\right| \tag{2.33}$$

b' is a function of h. Hence, the radius α is a function of h and b''. On the basis of this derivation, a simple computer code was written using Mathematica to determine α_{least} in the following steps:

1) Find the maximum value of α at fixed distance b'' in the range of h from zero to h_{max}, which is equivalent to the radius of aperture of the lens.
2) Plot the maximum value of α against b''. The shape of the plot represents the outer ray of light passing through the lens to the camera.
3) Find the minimum point of the plot, (α_{least}, b''_{least}).

The calculations were performed using single lens which has the paraxial focal length 74 mm for 248 nm. The distance, a, was fixed at 92 mm. The shape factor of the lens is equal to zero because of its symmetry. The radius of the aperture, h_{max}, was 3 mm. Based on the calculation result, the radius of the circle of least confusion was 7 μm. This

was also confirmed by simulation using the commercial optical software, Optalix® (Optenso™, Germany). Figure 2.3 shows the spot produced by the ray tracing simulation in Optalix at the same configuration as used in the original calculations. The unit in the axes is mm. Both simulations results were consistent with each other. However, the spot diameter (14 μm) when the scattered light was perfectly focused, is less than the size of one pixel in the ICCD camera (26 μm). This is practically unfavorable because it is difficult to distinguish the single pixel spot from the noise. The actual spot size using the single lens was adjusted to 3 pixels in radius which is 78 μm (26 μm/pixel) by defocusing the scattered light.

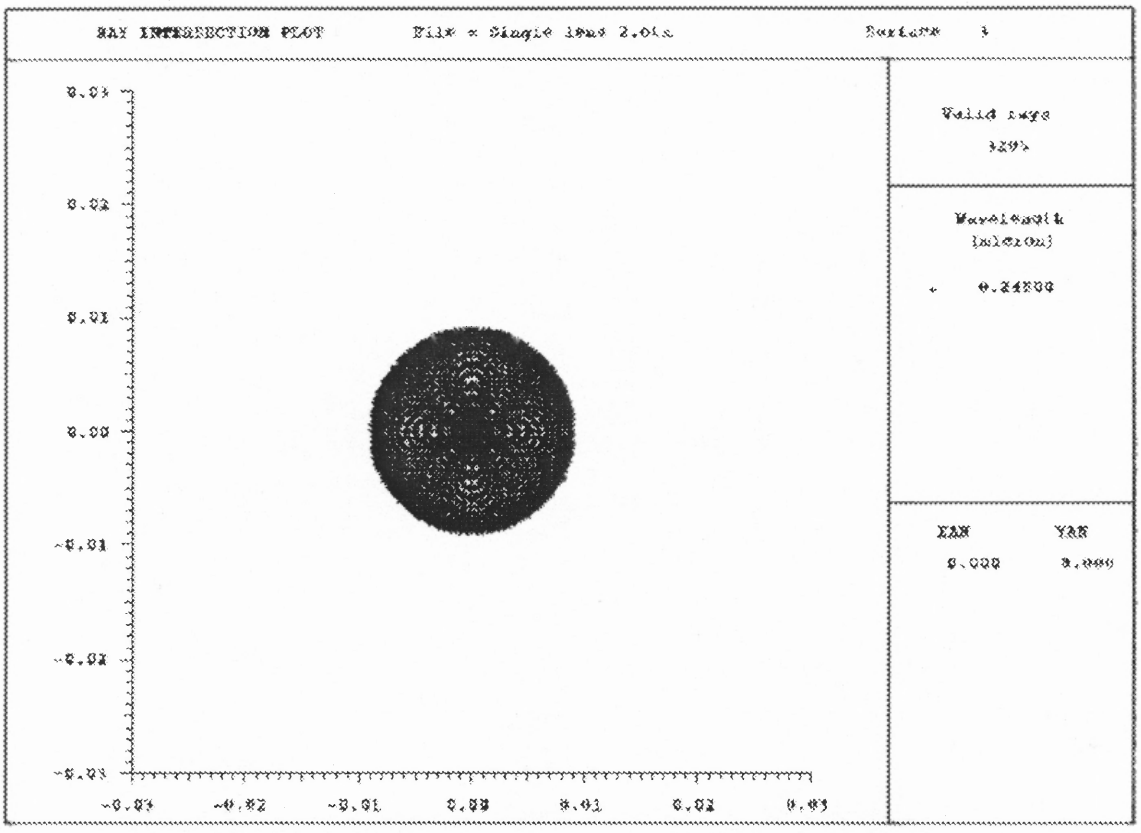

Figure 2.3 The simulation result for the spot image from single spherical lens.

The doublet lens (Part # 027-2220, OptoSigma Corporation) was designed to correct spherical aberrations. The focal length of the doublet is 50.8 mm. The spot size of the image of a point source projected by the doublet was simulated using Optalix. Figure 2.4 shows the comparison of spot size simulated using the doublet with the single lens. When the doublet is used, the solid angle for collection of scattered light can be increased due to the corrected spherical aberrations. The spot size based on the simulation is about 150 μm in radius when the aperture radius and the distance from the object to the doublet were 7.5 mm and 60 mm, respectively. The actual spot size in the measurement was six to eight pixels (150-200 μm). The simulation results are in good agreement with the experiment.

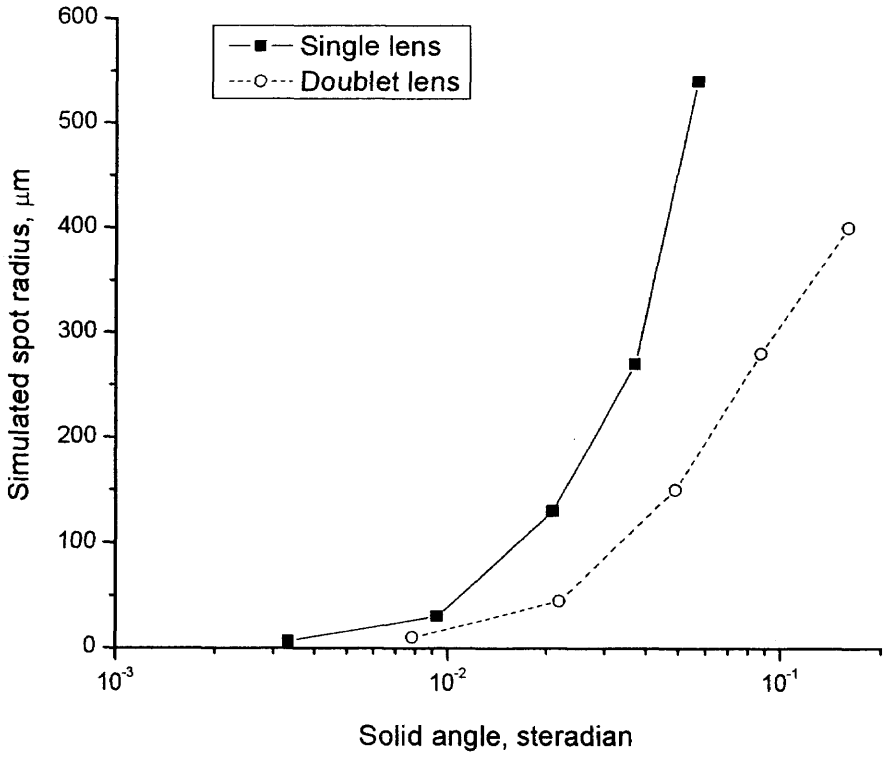

Figure 2.4 Simulated spot radius as a function of solid angle using the single lens and the doublet lens.

2.3 Approaches for Determination of Particle Sizes and Size Distribution Functions

2.3.1 Sensitivity of the Light Scattering Imaging System

Sensitivity of the optical system is a conversion factor from optical signal (scattered light from particles) to electrical signal (electric current at detector in camera) or vise versa. In this research the sensitivity is defined as the camera intensity (counts) per incident photon. In order to determine the sensitivity, calibration experiments were done before the *in situ* characterization of RDX nanoparticles. The details of the calibration experiment are discussed in Chapter 3. Using the sensitivity of the optical system and other parameters such as magnification and solid angle for light collection, the total intensity for individual spots which is measured directly from experiment is converted to the differential scattering cross section.

2.3.2 Determination of Particle Sizes and Size Distribution Functions

Particle size and the size distribution functions are to be determined from the intensity distribution functions for scattered light. The intensity in this case can be expressed as the differential scattering cross section of a particle calculated from the number of counts in the ICCD camera and the sensitivity. If the particles are spheres, the process of size determination can rely on the Mie theory, which gives the exact solution of Maxwell equations for the scattering problem. Based on the curves shown in Figure 2.1, a particle size corresponding to the scattering intensity (that is the differential scattering cross section determined from the experiment) is determined.

However, the curve at the region of large sphere size in Figure 2.1 becomes an oscillating function and gives multiple answers for the size determination. This is known

as the inverse light scattering problem,[41,42,43] which is normally inevitable unless there are other variables for the measurement such as scattered angles or incident wavelength in order to narrower the possible answers. The alternative method to resolve this problem is discussed in Chapter 4.

2.4 Design and Operation of the Light Scattering Imaging System

2.4.1 Setup of the Light Scattering Imaging System

The experimental setup of the light scattering imaging system is shown in Figure 2.5. The master pulse generator (Model 555, Berkeley Nucleonics Corporation) generates pulses that are sent to the pulse controller (Model DG535, Stanford Research Systems, Inc.) and two lasers: OPTex excimer laser (Lambda Physik Inc., KrF, wavelength 248 nm) and EX100 excimer laser (Gam Laser Inc., KrF, wavelength 248 nm). DG535 generates pulses which control the gate width and the delay time of the ICCD (Intensified CCD) camera (ICCD-MAX, Princeton Instruments Inc.). The pulse generator is controlled by a PC using a software WinSpec/32 (Roper Scientific Inc.). The laser pulses and the ICCD camera gate were synchronized in terms of the delay time and the gate width to capture the images.

The sampling zone shown in Figure 2.5 is illuminated perpendicular to the RESS jet by unpolarized light from two excimer pulse lasers passing through a rectangular slit. The two pulse lasers are used to characterize the velocity filed of RESS jet. The slit was used to ensure uniform intensity distribution over the cross section of the incident laser beam. The width and height (0.9 and 1.3 mm, respectively) was chosen to provide acceptable light intensity uniformity. According to the manufacturer's publication, the

original profile (that is to say, without the slit) along the short side of the rectangular cross section of the laser beam is a Gaussian distribution with 4 mm full width at half maximum. The error in the uniformity of the profile after the slit located at the center of the Gaussian profile was ± 3 % based on the estimation. This is rather small compared to the fluctuation of the laser energy, which was estimated experimentally to be ± 18 %.

The total energies of the two pulse lasers were measured by a laser energy meter (J50 LP-1, Molectron Detector Inc.). The light scattered by particles at 90° is focused by a fused silica lens (single or doublet type) to an intensified CCD (ICCD) camera (ICCD-MAX, Princeton Instruments Inc.). The doublet lens can be used to minimize spherical aberrations and, as a consequence, to be able to collect more scattered light than when the single lens was used by increasing the solid angle. The solid angle for the light collection was calculated from the aperture diameter and the distance between the sampling zone and the lens. When the doublet lens is used, the larger aperture diameter were installed because of less spherical aberrations of the doublet.

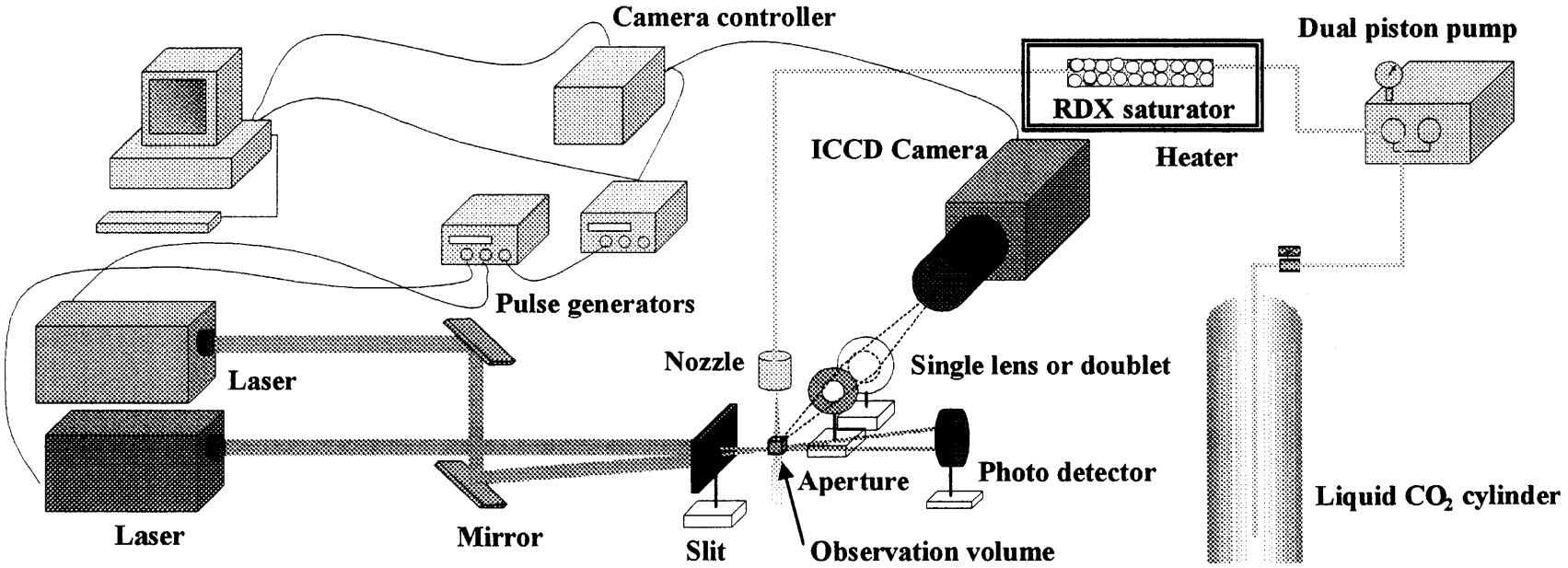

Figure 2.5 Experimental set up.

2.4.2 Measurements of Optical Magnification

The magnification of the optical system was determined to calculate the sampling volume for light scattering. The sampling volume is defined by multiplication of the cross sectional area of the incident laser beam by the length projected to the camera with magnification. The cross sectional area of the incident beam is equivalent to the opening area of the slit with neglecting diffraction of the incident light by the slit.

The measurements of the magnification were done as follows: (1) illuminate a thin wire and capture the focused image of the reflected light from the thin wire; (2) move the wire to the direction parallel to the incident beam and record the distance of the movement; (3) measure the corresponding distance for an image moved; (4) plot the distance of the image movement as a function of the actual distances to move the thin wire. The results are shown in Figure 2.6. The slopes of the straight lines fitted to the points expressed as pixels / mm were converted to the magnification 4.1 for the single lens and 3.1 for the doublet lens, respectively.

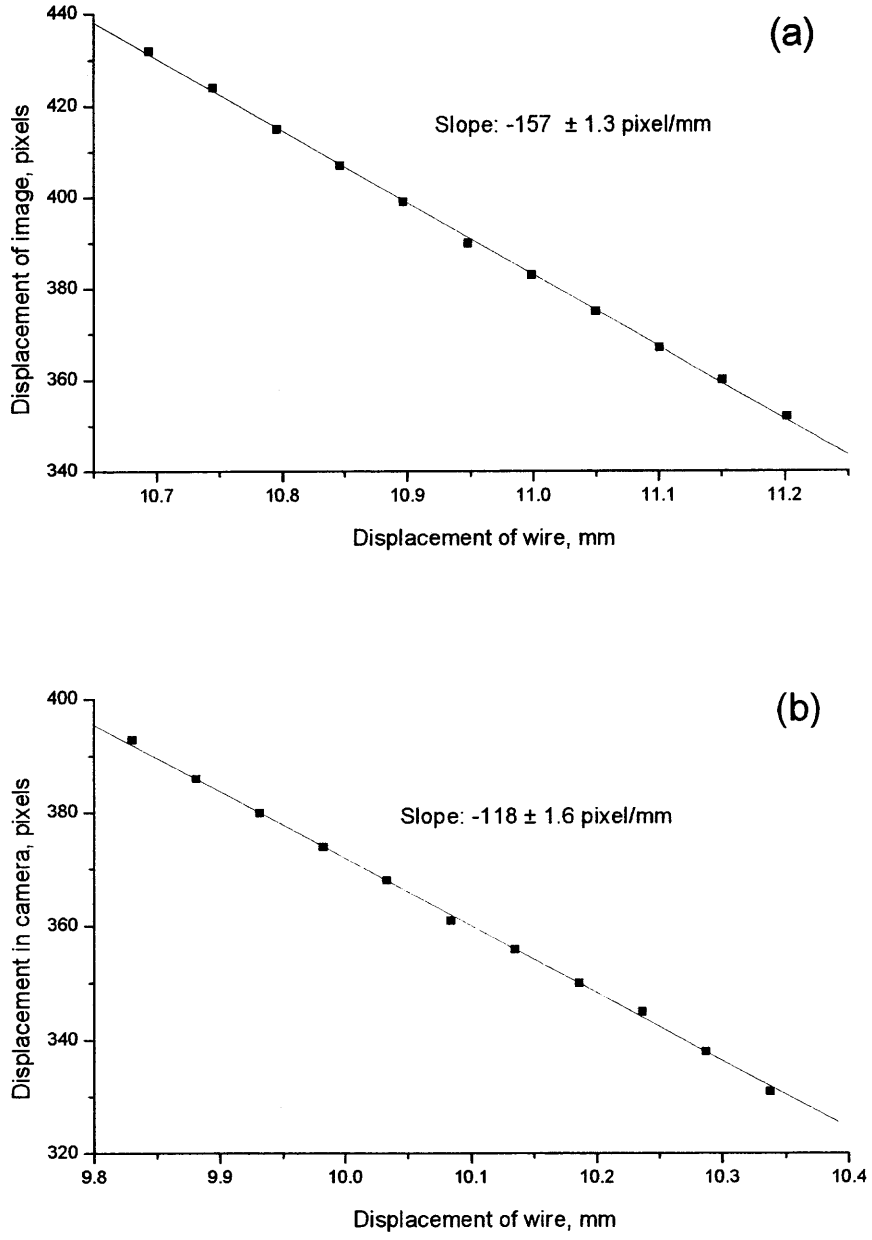

Figure 2.6 Determination of magnifications by measuring the displacement of the thin wire in the image: (a) single lens; (b) doublet lens.

2.4.3 Process of Image Analysis

The images captured by the ICCD camera were processed to determine the spot intensity distribution functions by using the program "Spot Counter" written by Dr. Evgeni N. Chesnokov (Institute of Chemical Kinetics and Combustion, Novosibirsk, Russia). The functions of this program are :

(1) reading and displaying the Winspec image file;

(2) subtracting the background of the image;

(3) searching for spots using the preset criteria;

(4) summing up the ICCD count intensity in each pixel composing a spot;

(5) accumulating the data for all spots trapped by the preset criteria in a frame;

(6) repeating the step (1) – (4) for many frames.

In the step (2), the two-dimensional Fourier transform was carried out on each frame to filter out the low frequency background. The order of Fourier transformation was set to 9. Then the program searched for the spot of which the central pixel had the maximum ICCD counts that was more than the preset criteria, that is, the preset number of the ICCD counts. The size of spot was set to 3 pixels for radius when the single lens was used. In the case of the doublet, the radius of the spot to be searched was 8. The preset criteria was changed as the resulting number of particles in a frame get equalized to the number of particles counted by the manual process. The intensity histograms were obtained by sorting the spot integral intensities into an appropriately binned intensity axis.

CHAPTER 3

CALIBRATIONS OF THE LIGHT SCATTERING IMAGING SYSTEM

3.1 Introduction

The light scattering imaging system designed in Chapter 2 needs to be calibrated before the characterization experiments in order to translate the measured signals (the scattered light intensity) to the physical quantities (particle size). The calibration in this research is equivalent to determination of the sensitivity of the ICCD camera, which is defined as the number of ICCD counts (arbitrary unit of intensity) per incident photon.

In this study, the light scattering imaging system was calibrated using standard latex particles with known diameter as well as Rayleigh scattering from air to determine the sensitivity. The standard latex particles are almost perfect spheres so that the Mie theory is ideally applicable. The calibration based on the Rayleigh scattering from air was done not only for verifying the sensitivity but also examining dependence of the sensitivity on the scattered light intensity. The intensity independency is suitable for the analysis because we can use a constant value of the sensitivity for any size of RDX particles.

3.2 Experimental

3.2.1 Calibration by Rayleigh Scattering from Air

The laser beam was focused by a spherical lens (focal length 200 mm at 248 nm), so that the focus was in the field of view of the optical system, which consisted of the imaging optics (the single lens) and the camera. The calibration then consisted of the accumulation of a number of pulses in a single frame, measuring the total laser energy, and processing of the beam image formed by Rayleigh scattering. The number of scattered photons was evaluated theoretically.

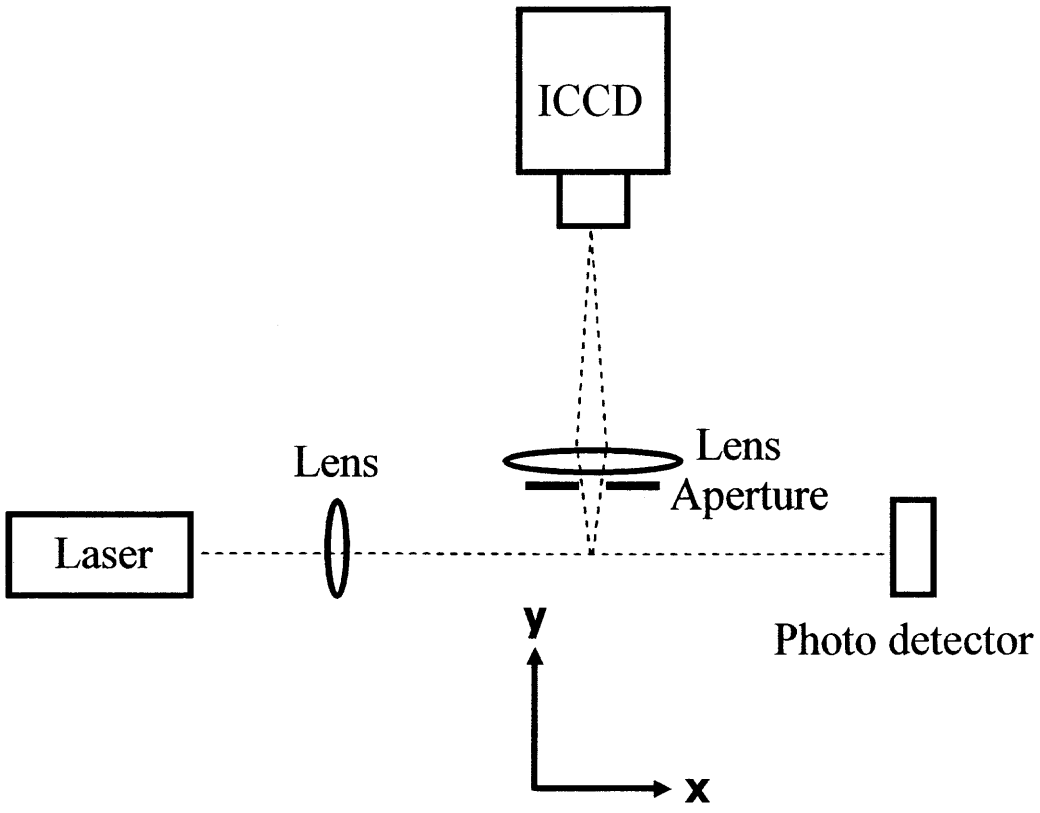

Figure 3.1 The Cartesian coordinates in the light scattering geometry.

Figure 3.1 shows the arrangement and the Cartesian coordinates used in the discussion. The Z axis is perpendicular to the beam and the observation direction. The optical system magnification was measured using thin wire as a scattering object and a translation stage to shift the wire by known distances. The magnification of the system was 5.1 ± 0.1.

When using Rayleigh scattering from air, the sensitivity was determined as:

$$\beta = \frac{N_{ICCD,Rayleigh}}{N_{sc,Rayleigh}} \tag{3.1}$$

where $N_{ICCD,Rayleigh}$ is the total number of counts per unit length along the X axis per pulse, and $N_{sc,Rayleigh}$ is the corresponding total number of scattered photons from unit length that hit the photocathode of the camera per pulse. Integrating the cross section curve along the Z-direction, the total number of counts per length of one pixel of the ICCD camera, $\tilde{N}_{ICCD,Rayleigh}$, is obtained. Then the $N_{ICCD,Rayleigh}$ is calculated using the magnification of the optical system as:

$$N_{ICCD,Rayleigh} = \tilde{N}_{ICCD,Rayleigh} \frac{M}{L} \tag{3.2}$$

where M is the magnification and L is the size of one pixel in the ICCD camera in the X-direction. $N_{sc,Rayleigh}$ is calculated as:

$$N_{sc,Rayleigh} = nN_{inc}\left(\frac{d\sigma}{d\Omega}\right)_{molecule} \Omega \tag{3.3}$$

where N_{inc} is the number of incident photons per pulse, n is the number density of molecules, σ is the Rayleigh scattering cross section, Ω is the solid angle for the light

collection, and $\left(\frac{d\sigma}{d\Omega}\right)_{molecule}$ is the differential scattering cross section of a molecule for unpolarized incident light at the observation angle of 90°. N_{inc} is given by

$$N_{inc} = \frac{E_{inc}\lambda}{hc} \tag{3.4}$$

where h is Plank's constant, c is the speed of light, E_{inc} is the energy of the incident laser light per pulse, and λ is the wavelength of the incident laser light.

From Equations 3.1 – 3.4, the sensitivity is calculated as follows:

$$\beta = \frac{hc\tilde{N}_{ICCD,Rayleigh}}{nE_{inc}\lambda\left(\frac{d\sigma}{d\Omega}\right)_{molecule}\Omega}\frac{M}{L}. \tag{3.5}$$

3.2.2 Calibration by Scattering from Standard Latex Particles

For the calibration using standard particles, the standard polystyrene spheres with known mean diameters of 102 and 152 nm (NANOSPHERE^{TM}, Catalog # 3100A and 3150A, Duke Scientific Corporation) were used. The original aqueous solution containing 1 wt. % of polystyrene particles with small amounts of a surfactant (< 0.1 wt. %), was diluted 2000 times by methanol. Then this solution was dispersed using an aerosol generator (ATM 225, Topas GmbH). Additional air flow was admixed downstream the aerosol generator to evaporate methanol droplets and carry airborne latex particles to the observation zone of the experimental setup. The setup for generation of latex particle flow is illustrated in Figure 3.2.

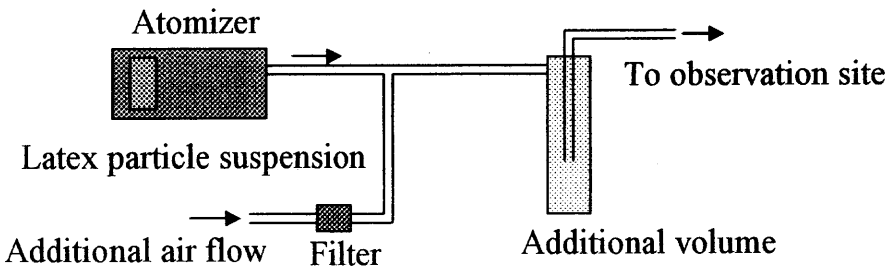

Figure 3.2 Illustration of particle flow generation.

The sensitivity was determined in the similar manner as done by Rayleigh scattering from air. The total number of counts per standard latex particle $N_{ICCD,latex}$ is obtained from the scattering images. Using the differential scattering cross section calculated using Mie theory, the total number of scattered photons from a single latex particle is

$$N_{sc,latex} = \frac{N_{inc}}{A}\left(\frac{d\sigma}{d\Omega}\right)_{particle}\Omega \tag{3.6}$$

where A is the cross sectional area of the incident laser beam. The cross sectional area was defined by the rectangular slit. The differential scattering cross section was calculated using the Fortran program, Chiral.[38] The index of refraction of 1.803+0.0072i (see Appendix B) for polystyrene was used for the calculation. The sensitivity is then calculated as:

$$\beta = \frac{hcAN_{ICCD,latex}}{E_{inc}\lambda\left(\frac{d\sigma}{d\Omega}\right)_{particle}\Omega}. \tag{3.7}$$

3.3 Results and Discussion

3.3.1 Sensitivity Determined by Rayleigh Scattering from Air

A sample image of Rayleigh scattering from air is shown in Figure 3.3 (a). In this image, 30 frames were summed up so that the intensity is 30 times larger than the intensity in a single frame.

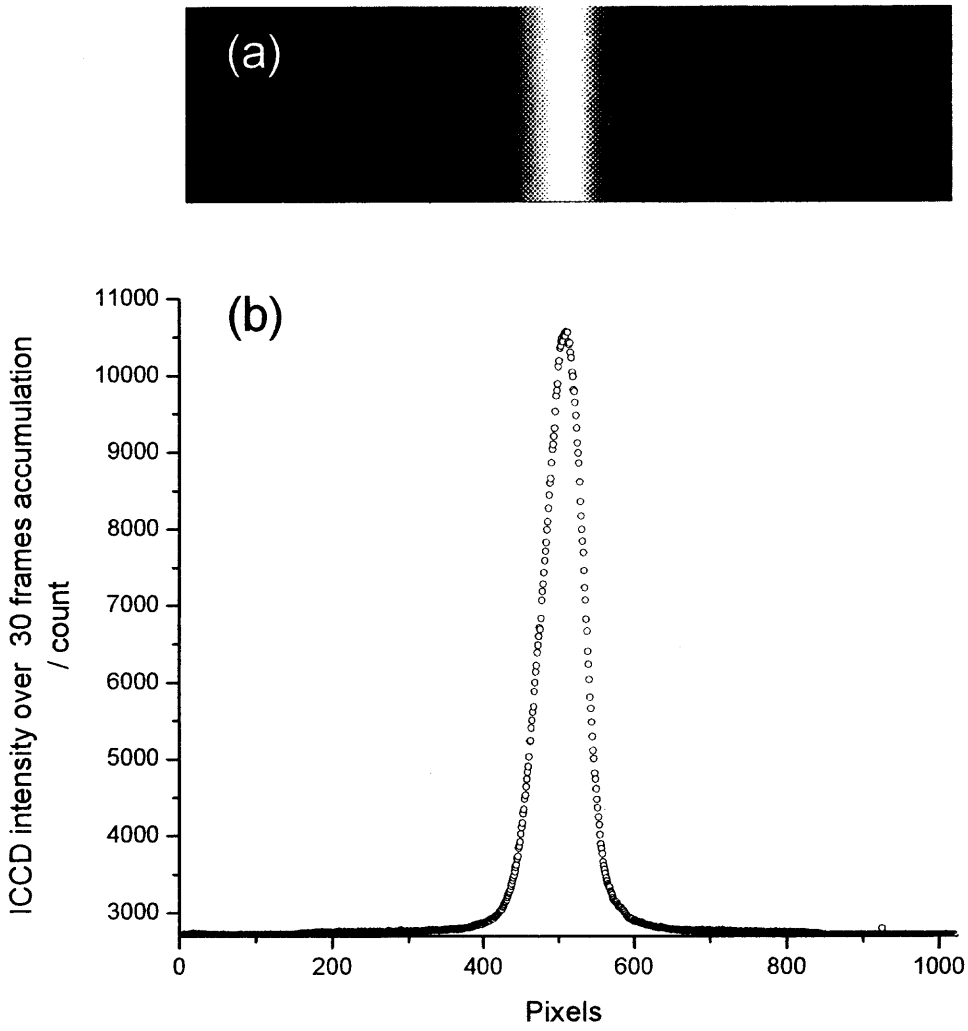

Figure 3.3 An image of Rayleigh scattering from air (a) and an average cross section of the image (b).

The white strip is the image of the laser beam produced by the Rayleigh scattering from air. Figure 3.3 (b) presents the cross section along the horizontal axis of this image (that corresponds to the Z-direction of Cartesian coordinate in Figure 3.1). The sensitivity of the ICCD camera was calculated by dividing the total intensity (the area below the curve) by the theoretical number of photons collected by the camera, as described in Section 3.2.1.

This was done for different intensities of the incident light, and the dependence of the sensitivity on the light intensity was determined (Figure 3.4).

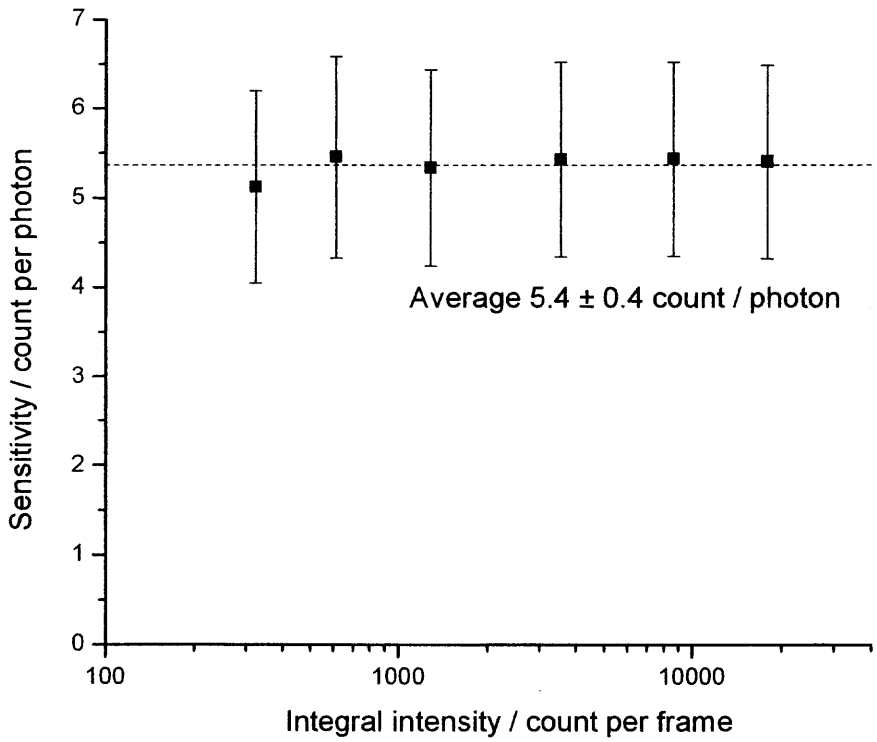

Figure 3.4 Sensitivity of ICCD camera as a function of total intensity collected by the camera.

Fig. 3.4 shows that the sensitivity of the ICCD camera is independent of the incident light intensity with about 20 % error that is attributed to the absolute accuracy for detecting laser energy. The 20 % error of the sensitivity is equivalent to 7 % of 100 nm diameter for a RDX particle and 5 % for a 70 nm RDX particle.

3.3.2 Sensitivity Determined by the Scattering from Standard Latex Spheres

A sample of the captured image of scattering from latex particles of 152 nm mean diameter is shown in Figure 3.5. The bright spots are scattered light from individual particles.

Figure 3.5 The image of scattered light from the standard latex spheres of 152 nm diameter.

The intensity distribution functions of scattered light from the standard polystyrene particles of 102 nm and 152 nm diameter are shown in Figure 3.6. It should be noted that the distribution functions in Figure 3.6 cannot be purely considered as those of the latex spheres because the formation of surfactant (dispersant) particles is inevitable and affects the distribution functions for the latex spheres. Moreover, the laser energy fluctuations (± 18 %) also cause a broadening of the distribution functions for the latex particles. The ± 18 % of error in fluctuation of the incident laser energy is equivalent to the ± 4 nm of error in the 102 nm latex particle size On the other hand, the manufacturer

has specified standard deviation for the distribution of the 102 nm polystyrene spheres as 4.5 nm.[44] However, the measurement using TEM resulted in standard deviation of 6 nm.[45] Taking ± 4 nm error from the fluctuation of the laser energy and ± 6 nm from the TEM measurement, the total error in the particle size was estimated as ± 7 nm for the 102 nm latex particles. The standard deviation in the scattered light intensity distribution function of the 102 nm latex particles presented in Figure 3.6 is approximately ± 40 % (determined by full width at half maximum of the function) which is equivalent to ± 10 nm of diameter. The error estimated based on the distribution curve in Figure 3.6 is slightly larger (3 nm). This could be due to the effect of surfactant particles.

The distribution function obtained from 150 nm the scattering intensity scale appears to be much narrower, which is due to much weaker dependence of the scattered light intensity on the particle diameter around 150 nm. The long tail on the size distribution functions is attributed to the wing of the surfactant particle distribution function. The dashed line in Figure 3.6 represents the detection limit. The particle size below this line cannot be determined using this experimental arrangement. According to the estimate, the surfactant which is present in the original latex particle suspension at the weight concentration 0.1 % and after the dilution of 2000 times, will form particles of about 6 nm in diameter assuming the size of droplets formed by the aerosol generator are 1 μm.

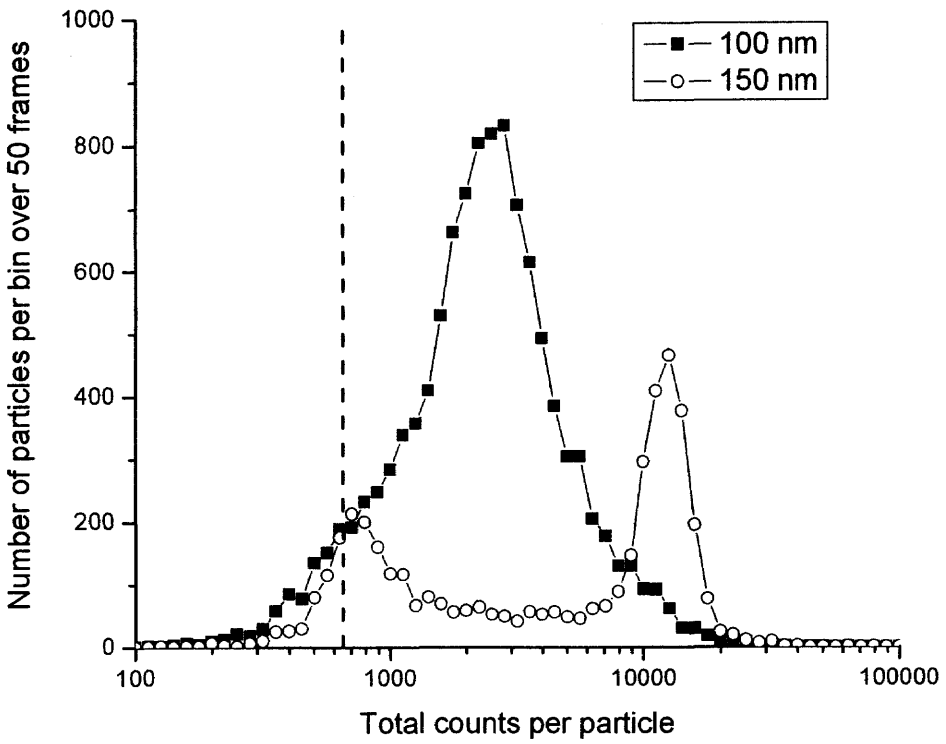

Figure 3.6 Distribution functions of the scattered light intensity from standard polystyrene spheres of 102 nm in diameter (filled squares) and 152 nm (open circles). The long tail for 152 nm particles is presumably caused by the particles of the surfactant (see text). The dashed line represents the cut-off for the small size limit of particle detection.

The sensitivity was calculated based on the differential scattering cross section at 90° for unpolarized light for a polystyrene spheres calculated using the Mie theory[36] and the ICCD intensity counts at the maximum of the intensity distributions in Figure 3.6. In these calculations, the complex index of refraction of polystyrene was taken as $1.803+0.0072i$, as evaluated from the dielectric constants of polystyrene.[46] The details of these calculations are described in Appendix B. The Fortran program, Chiral,[38] downloadable from internet was used as a Mie scattering code. The sensitivity determined from the calibration using the polystyrene spheres was 5.2 ± 0.4 count per

incident photon, in good agreement with the results of the Rayleigh scattering calibration (5.4 ± 0.3 count per incident photon).

3.4 Summary

The sensitivity of the ICCD camera was determined via a calibration of the light scattering imaging system using scattering from air and the latex particles. Both calibrations give the consistent results for the sensitivity. The independency of the sensitivity on the intensity of scattered light was observed by the calibration using Rayleigh scattering from air. In other words, the linear relationship between the ICCD camera signal and the number of photons coming into the camera was confirmed. Thus, in the light scattering measurements, the size determination process can be simplified by using the constant sensitivity.

CHAPTER 4

IN SITU DETRMINATION OF RDX PARTICLE SIZE DISTRIBUTION FUNCTIONS

4.1 Introduction

Unlike other optical methods using light scattering or extinction described in Section 1.3.2, each single spot corresponding to a particle was resolved and processed separately. One of the advantages of this particle-by-particle treatment is that the particle size distributions can be rigorously evaluated without any additional assumptions on the shape of the distribution functions. Another advantage is that in the images one can differentiate light scattering by the turbulent RESS flow from the scattering by the particles. In this chapter, the details of the experiment procedure for the *in situ* characterization are described, and the resulting size distribution functions of RDX particles formed by RESS are discussed. The particle sizes determined by the *in situ* method are also compared to those obtained by the SEM and TEM analysis.

In order to determined the RDX particle size from the light scattering measurement, the index of refraction of RDX at 248 nm is required. Although there are several methods to measure the index of refraction of RDX, the attempt for the desired wavelength was not successful due to lack of precision and instrumental ability. Instead, the index of refraction of RDX at 248 nm was evaluated based on the reflection spectrum available in the literature.

4.2 Experimental

The RESS system is schematically shown in Figure 2.5. Liquid CO_2 (CD 3.0, Praxair Inc.) was taken from a cylinder and pumped to the desired pressure by a high-pressure dual piston pump (Model P-50, Thar Design Inc.). Then it was heated to a supercritical extraction temperature and flowed through the extractor loaded with glass beads of 3 mm in diameter coated by RDX. The saturated solution was heated to a desired pre-expansion temperature by the nozzle and throttled across the expansion unit that consisted of a sapphire capillary nozzle with the diameter of 0.102 mm and the length of 0.254 mm (Figure 4.1). The nozzle was mounted in a holder with the holder outlet coaxial with the nozzle with the diameter of 1 mm and thickness of 1.5 mm. The heating by the nozzle was required to avoid nozzle clogging. Solid nano-scale particles of RDX are formed downstream the jet and measured in the sampling zone of the experimental setup shown in Figure 2.5.

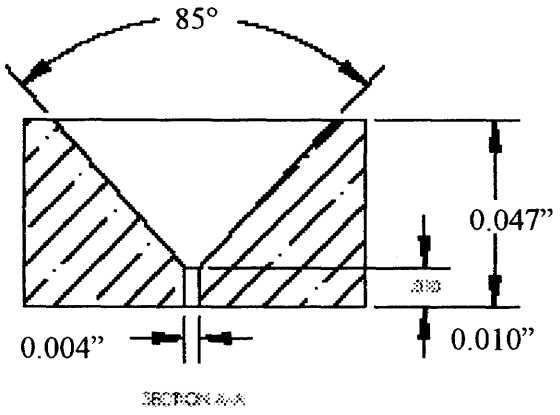

Figure 4.1 The geometry of the sapphire capillary nozzle.

Temperature profiles in the RESS jet were determined using a K-type thermocouple made of chromel and alumel wires with the diameter of 0.1 mm. Both wires were connected to the multimeter to measure the voltages at the different position along the jet. As the voltage was measured relative to the reference junction at room temperature, it was corrected to the values for 0° reference junction. Then, the temperature was determined from the tabulated data of temperature – voltage at 0 °C reference junction.[47]

4.3 Results and Discussion

4.3.1 Scattering in Pure CO_2 RESS and RDX-CO_2 RESS

The scattering images from pure CO_2 RESS jet at the pre-expansion pressure of 140 bar, the saturator temperature of 80 °C, and the nozzle temperature of 140 °C are shown in Figure 4.2 (a)-(c). The RESS jet is seen as the bright area spreading horizontally at 2.5 mm distance from the nozzle, which is caused by scattering from turbulent flow of CO_2 (Figure 4.2 (a)). Because pure CO_2 RESS jet has a strong and dense turbulent flow of CO_2, the turbulence is still recognized at 12.5 mm from the nozzle accompanied with a few particles (Figure 4.2 (b)). When the jet proceeds downstream farther (Figure 4.2 (c)), most of the condensed CO_2 evaporates and almost no particles are observed at this RESS conditions.

Figure 4.3 shows the images of scattered light from particles in RDX-CO_2 RESS at the pre-expansion pressure of 140 bar, the saturator temperature of 80 °C, and the nozzle temperature of 140 °C. The images were captured at 2.5 mm from the nozzle (Figure 4.3 (a)), 17.5 mm from the nozzle (Figure 4.3 (b)), and 39.5 mm from the nozzle

(Figure 4.3 (c)). In Figure 4.3 (a), the turbulent flow of the RESS jet as well as the particles are observed at 2.5 mm from the nozzle. The CO_2 turbulence disappears downstream the jet leaving the particles still observable (Figure 4.3 (b) and (c)). Thus the particles observed in Figure 4.3 can be considered to be RDX or mixture of RDX and CO_2.

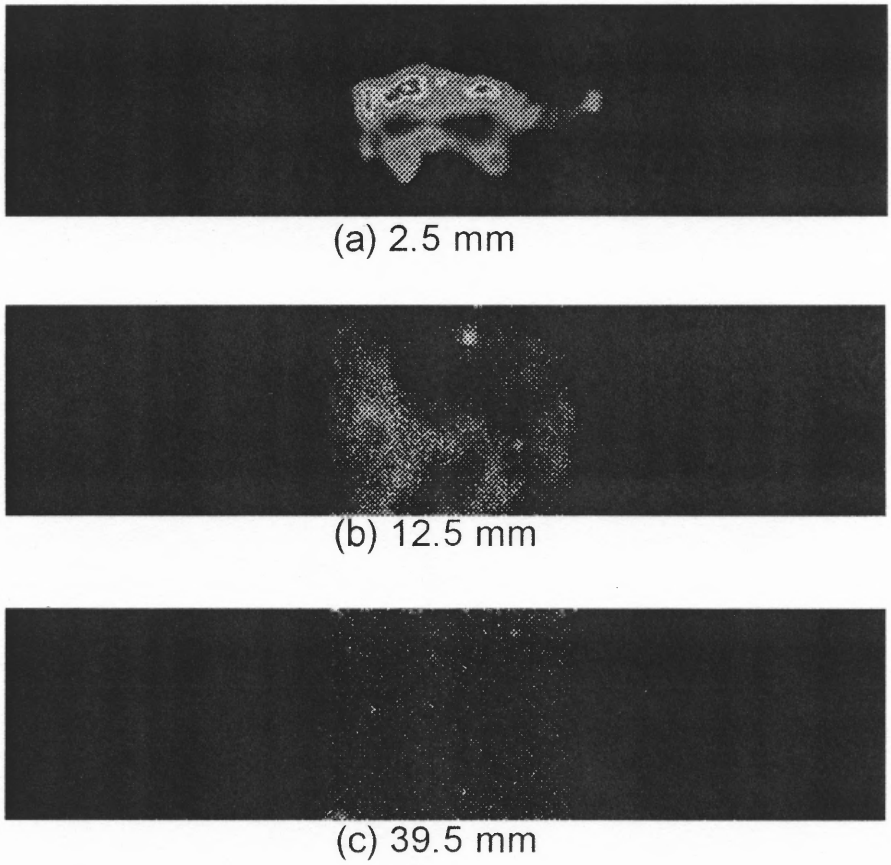

Figure 4.2 The images of scattering from particles in pure CO_2 RESS at pre-expansion pressure 140 bar, saturator temperature 80 °C and nozzle temperature 140 °C. The image captured at axial distance (a) 2.5 mm down from the nozzle; (b) 12.5 mm down from the nozzle; (c) 39.5 mm down from the nozzle.

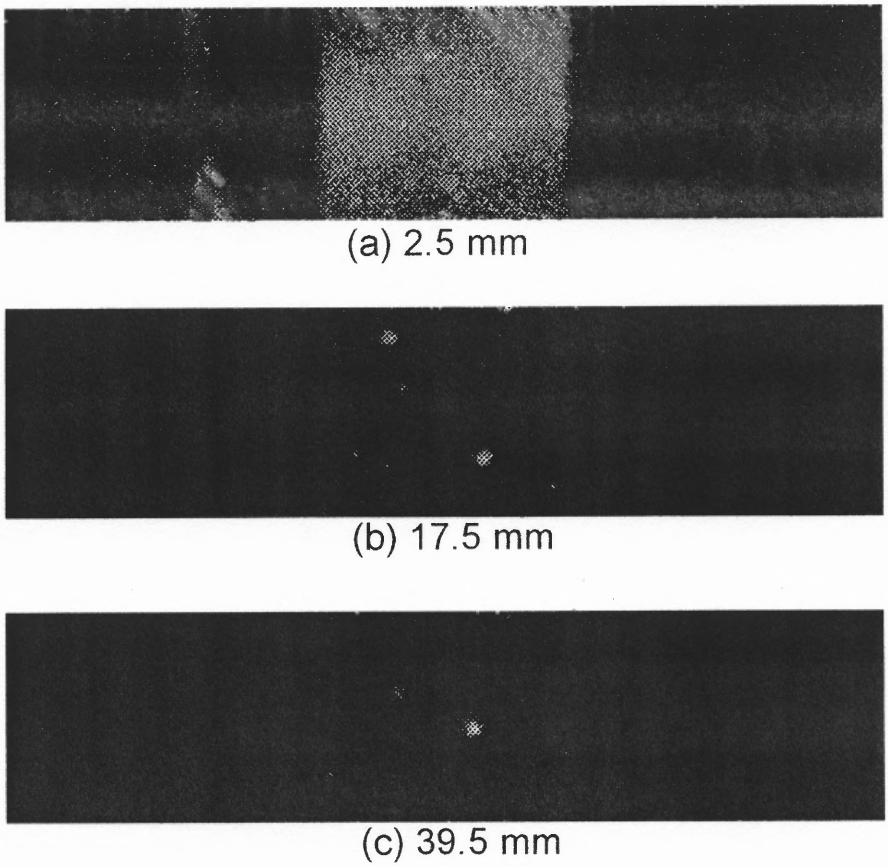

Figure 4.3 The images of scattering from particles in RDX-CO_2 RESS at pre-expansion pressure 140 bar, saturator temperature 80 °C and nozzle temperature 140 °C. The image captured at axial distance (a) 2.5 mm down from the nozzle; (b) 17.5 mm down from the nozzle; (c) 39.5 mm down from the nozzle.

Figures 4.4 and 4.5 show the scattering images at different positions in pure CO_2 RESS and RDX-CO_2 RESS, respectively, at the pre-expansion pressure of 180 bar, the saturator temperature of 80 °C and the nozzle temperature of 140 °C. The scattering images of RESS jet of pure CO_2 at the pre-expansion pressure of 180 bar show huge turbulence of CO_2 which remains even at 39.5 mm from the nozzle (Figure 4.4 (c)). It was not possible to obtain the distribution of scattered light from the particles under the

turbulent flow because the scattered light intensity from the turbulent flow is too strong to differentiate it from the scattered light from particles. The number of particles per frame in RDX-CO_2 RESS increased at the pre-expansion pressure of 180 bar (Figure 4.5), compared to the RESS at 140 bar in Figure 4.3, as the solubility of RDX in supercritical CO_2 increases with pressure.

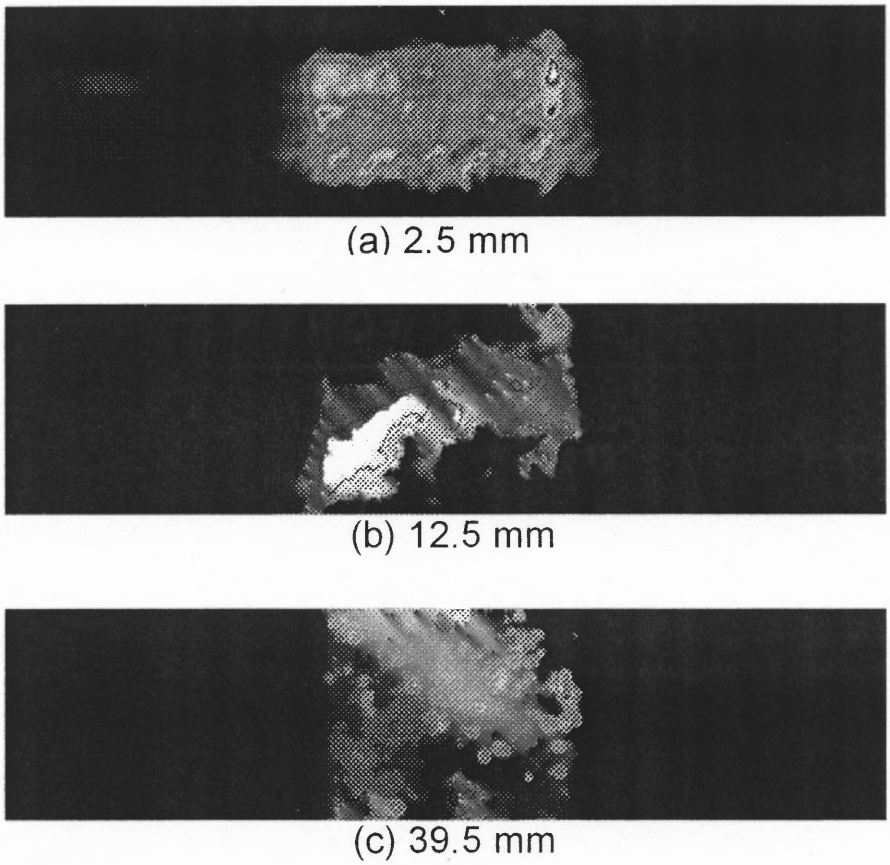

Figure 4.4 The images of scattering from particles in pure CO_2 RESS at pre-expansion pressure 180 bar, saturator temperature 80 °C and nozzle temperature 140 °C. The image captured at axial distance (a) 2.5 mm down from the nozzle; (b) 12.5 mm down from the nozzle; (c) 39.5 mm down from the nozzle.

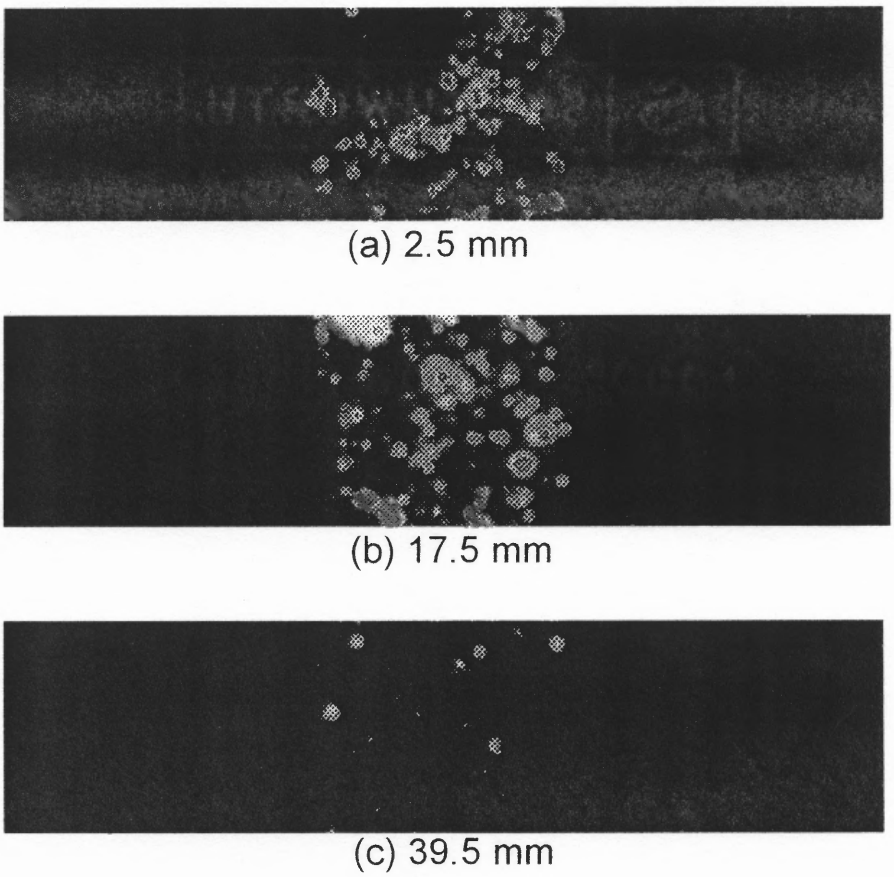

Figure 4.5 The images of scattering from particles in RDX-CO_2 RESS at pre-expansion pressure 180 bar, saturator temperature 80 °C and nozzle temperature 140 °C. The image captured at axial distance (a) 2.5 mm down from the nozzle; (b) 17.5 mm down from the nozzle; (c) 39.5 mm down from the nozzle.

The difference of the scattering images from the jets of RDX-CO_2 and pure CO_2 correlates with temperature profiles in these jets. The temperature profiles of the RDX-CO_2 and pure CO_2 RESS jets are shown in Figure 4.6. The higher temperature of the RDX-CO_2 RESS jet could be caused by condensation of larger amount of CO_2 in RDX-CO_2 RESS, where RDX molecules can act as nucleation centers.

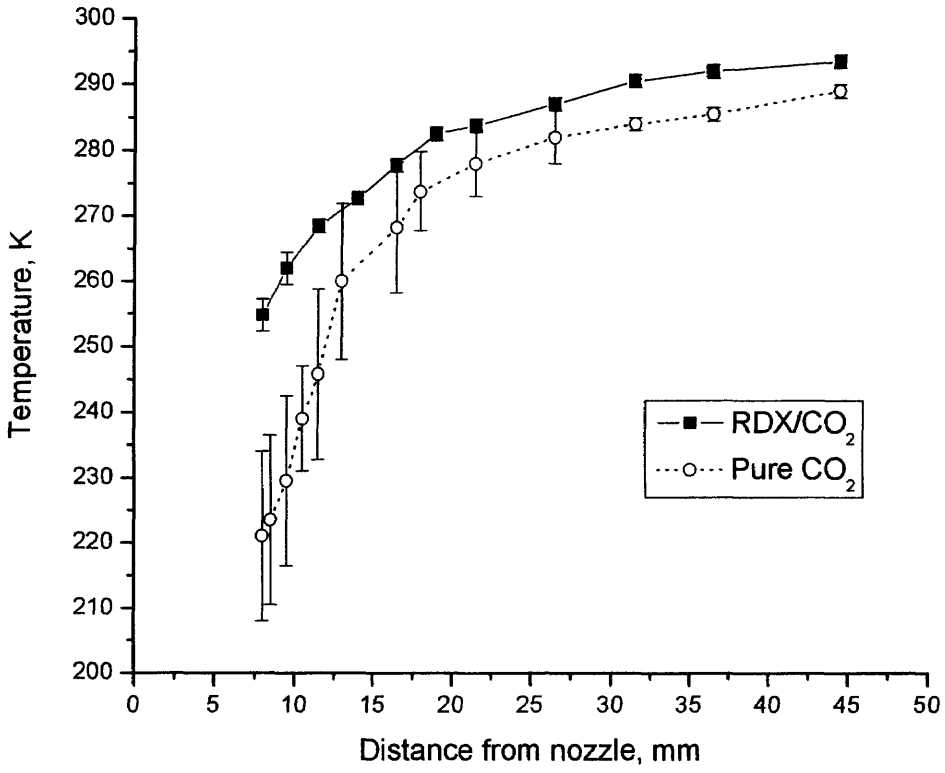

Figure 4.6 Axial temperature profiles along RESS jet of RDX/CO_2 and pure CO_2.

4.3.2 Distributions Profiles of the Scattered Light Intensity along RESS Jet

Figure 4.7 shows the comparison between the distribution functions of the scattered light intensity when the doublet and the single lens were used. The images were collected at 49.5 mm from the nozzle for the doublet, and at 45.5 mm for the single lens. The distribution function determined with the single lens used is not complete, as seen by the sharp edge in the left hand side of the function. The solid line and dashed line represent the particle detection limits with the single lens and the doublet lens, respectively. The sensitivity cut-off is not perfectly steep, because in the image processing software, "Spot Counter", the total intensity of a spot was not used as the cut-off criteria but the

maximum amplitude in a spot was used instead. Therefore, if there was a single pixel which has the intensity exceeding the criteria, this will be counted as a particle, however, with a small integral intensity.

Using the doublet, the detection limit was improved by a factor of four for the scattered light intensity, although the solid angle was 14 times larger than that when the single lens was used. The reason for the lesser improvement in the sensitivity is the contribution of the background noise enhanced by the doublet.

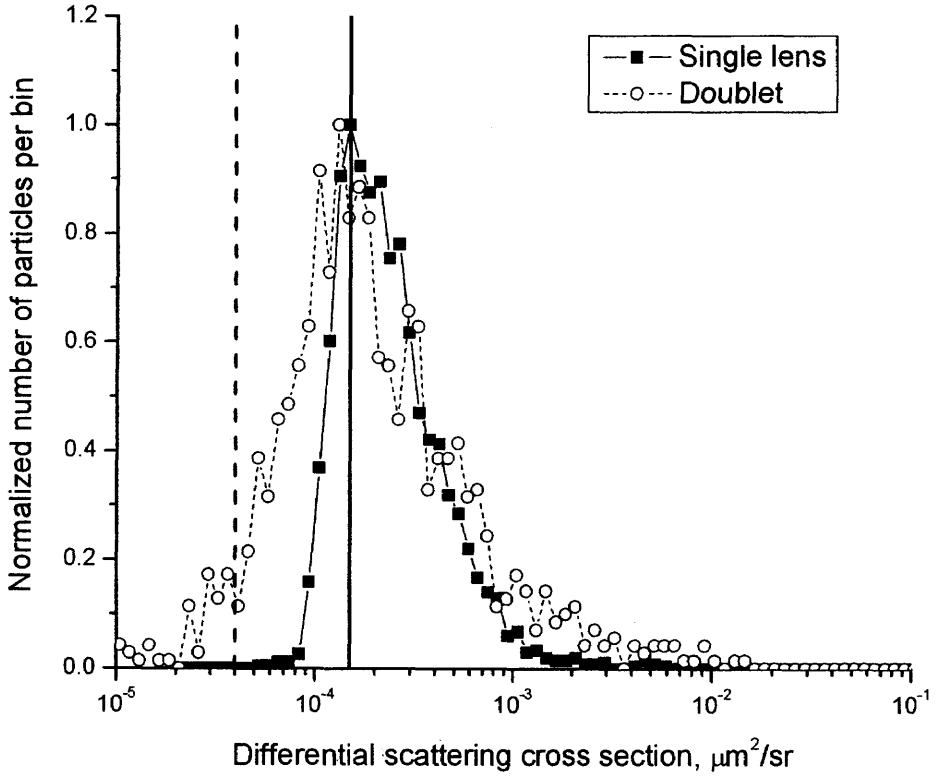

Figure 4.7 The comparison between the distribution functions of the scattered light intensity measured at 49.5 mm from the nozzle when the doublet was used and 45.5 mm when the single lens was used. The particles were formed at pre-expansion pressure 180 bar, saturator temperature 80 °C, and nozzle temperature 140 °C. Filled squares – single lens; open circles – doublet lens. Solid line – the detection limit when the single lens was used; dashed line – when the doublet was used.

The detection limit in terms of the particle diameter was improved from 80 nm with the single lens to 60 nm with the doublet.

The scattered light intensity distribution functions at different distances along the RDX-CO_2 RESS at the pre-expansion pressure of 180 bar are presented in Figure 4.8. The integral intensities of the spots decreased when going downstream along the jet. There is no other possible explanation for the decrease in the intensities but that the particles initially formed near the nozzle consisted mainly of CO_2, which subsequently evaporated downstream the jet leaving only RDX in the particles.

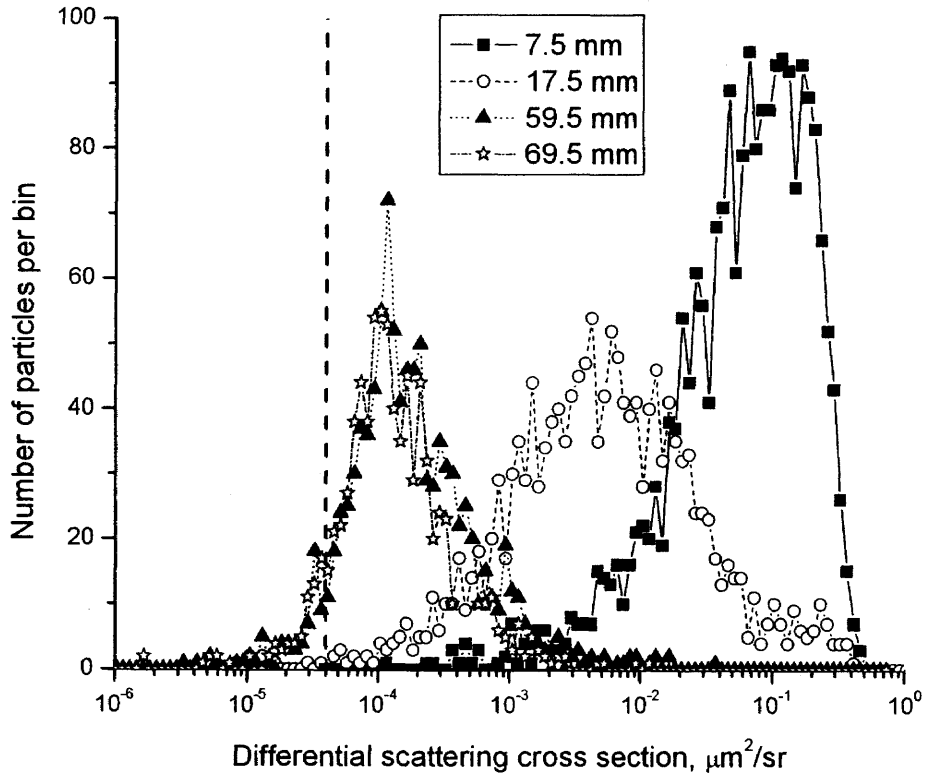

Figure 4.8 The distribution functions of the differential scattering cross sections of the particles along the RESS jet of pre-expansion pressure 180 bar, saturator temperature 80, and nozzle temperature 140 bar. Filled squares – 7.5 mm from the nozzle; open circles – 17.5 mm; filled triangles – 59.5 mm; open stars – 69.5 mm. The dashed line represents the detection limit of particles.

Since the shape of the intensity distribution functions after 59.5 mm from the nozzle does not change much, most of the condensed CO_2 seems to evaporate and the particles at these distances are considered to be pure RDX particles.

4.3.3 Non-sphericity of RDX Particles

Figure 4.9 shows an example of SEM image of RDX particles produced in the experiments. To collect the samples for the SEM analysis, the nozzle was oriented to generate the RESS jet horizontally. Glass substrates were placed at the distance of 10 cm from the nozzle and ca. 1.2 cm from the jet axis to deposit particles by sedimentation. The image shows individual particles with almost spherical shape.

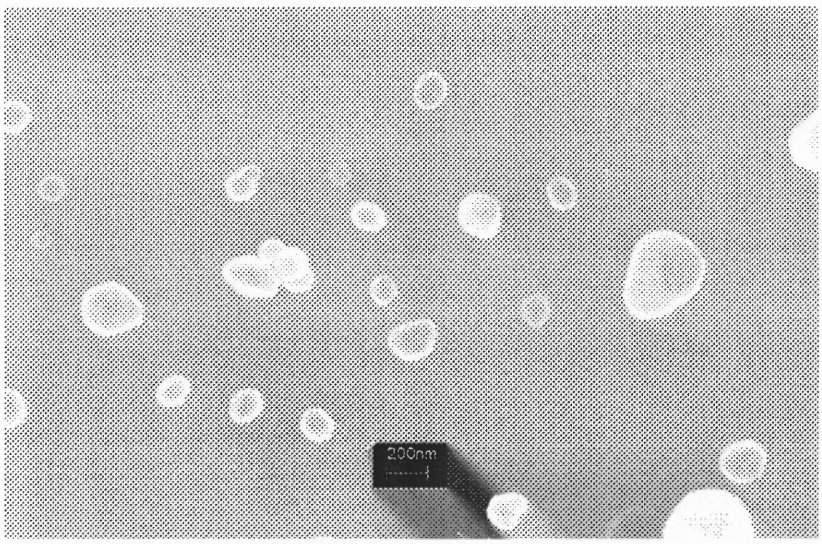

Figure 4.9 Sample SEM image of RDX particles obtained by RESS (pre-expansion pressure 180 bar).

The effect of non-sphericity of RDX particles on the scattered light intensity was estimated assuming that their shape can be approximated by a spheroid with the aspect ratio 1.2. For the estimates, a T-matrix method[48] was used, and considered all possible

orientations of the spheroids relative to the incident laser beam. The results are presented in Figure 4.10.

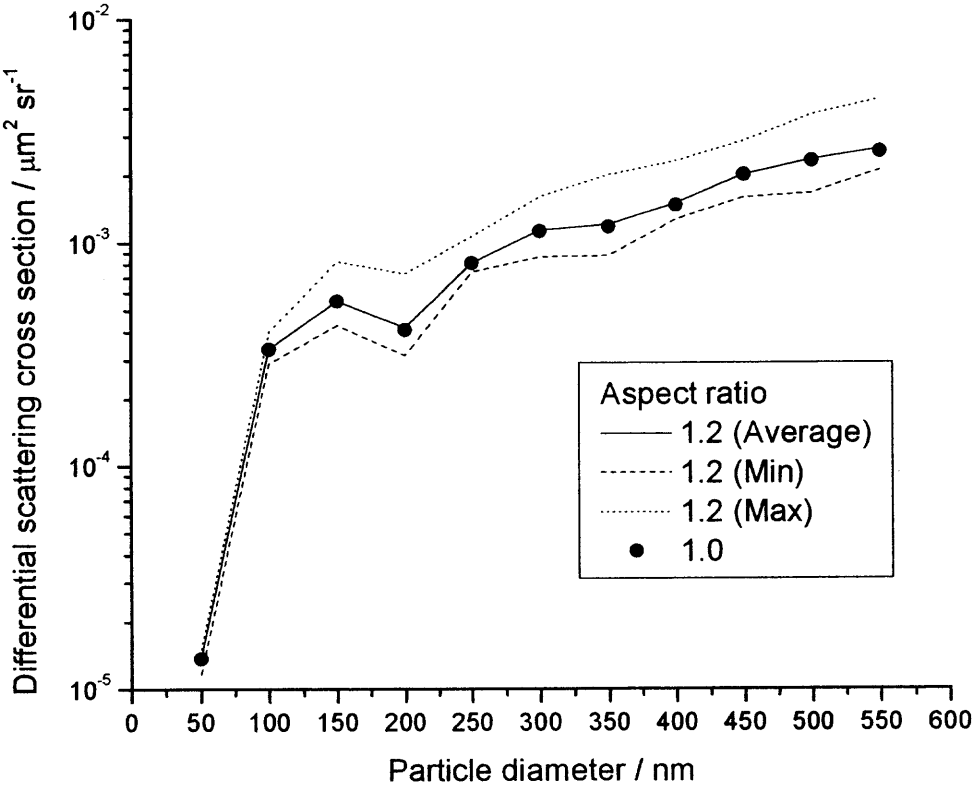

Figure 4.10 Light scattering cross section from non-spherical (spheroid) RDX particles at 90° for unpolarized incident light as a function of the equal-volume-sphere particle diameter. Solid line – the average differential scattering cross sections of all possible orientations for spheroids with the aspect ratio 1.2; dashed line – the minimum differential scattering cross sections at the aspect ratio 1.2; dotted line – the maximum differential scattering cross sections at the aspect ratio 1.2; filled circles – the differential scattering cross sections of spheres (aspect ratio of 1.0).

As it can be seen from Figure 4.10, the differential scattering cross sections averaged over the orientations of the spheroids with the aspect ratio of 1.2 can be approximated as those of a sphere. The error associated with the replacement of the spheroid with a spherical particle of equal volume is insignificant below 100 nm (less

than ± 5 % of the particle size). Above 100 nm the error becomes larger (about a factor of 2). Therefore, Mie theory for spherical particles gives relatively accurate results of the size distributions of RDX particles below 100 nm, and size distributions close to the average in the possible orientations of RDX spheroid particles above 100 nm.

4.3.4 Size Distribution Functions of RDX Particles

The differential scattering cross sections as a function of size shown in Figure 2.1 were used to convert the intensity distributions (*i.e.*, the distributions of the experimental differential scattering cross section) to the particle size distributions, when the data were outside the oscillating regions. The size distribution of RDX particles formed at the pre-expansion pressure of 180 bar was determined using this approach (Figure 4.11). The dash-dot line represents the minimum particle size to be determined by this method, which is 60 nm of diameter. The range between the two dotted lines labeled as "ambiguous region" in Figure 4.11 corresponds to the oscillation range in the differential scattering cross section between 110 nm and 230 nm diameters of RDX particles. Due to the impossibility of unambiguous assignment of the differential scattering cross section to the particle diameter in this region, the shape of the distribution function in this region cannot be determined.

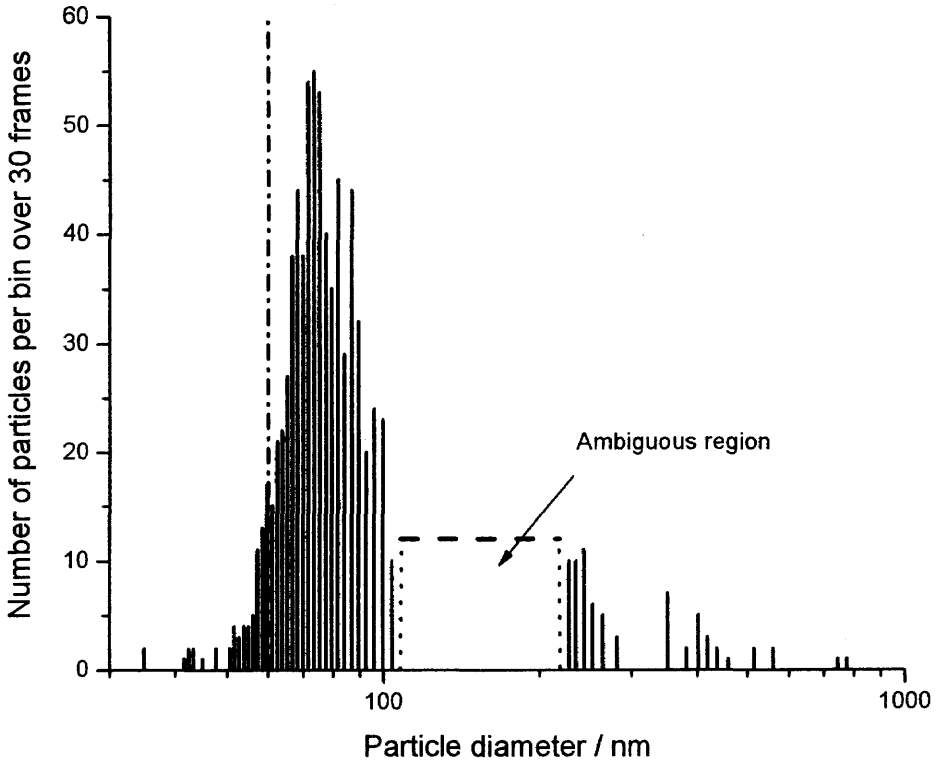

Figure 4.11 Size distribution of RDX monitored at the distance 69.5 mm from the nozzle. The dashed line represents the averaged number of particles per bin in the "ambiguous region". The RESS conditions: pre-expansion pressure 180 bar; saturation temperature 80 °C; nozzle temperature 140 °C.

However, the total number of particles in this size region still can be determined with certainty. The horizontal dashed line in Figure 4.11 shows the total number of particles in the "ambiguous region" divided by the total number of bins in this region. One of the conclusions made from Figure 4.11 is that the particle size at the maximum of the distribution is 73 nm. The particle sizes obtained from the *in situ* measurement are somewhat smaller compared to the typical particle sizes measured using SEM. For example, the mean diameter of RDX particles collected by sedimentation inside a RESS

chamber was 150 - 200 nm as determined by SEM (Figure 4.12). This discrepancy could be due to the size discrimination when the particles were collected for the SEM analysis.

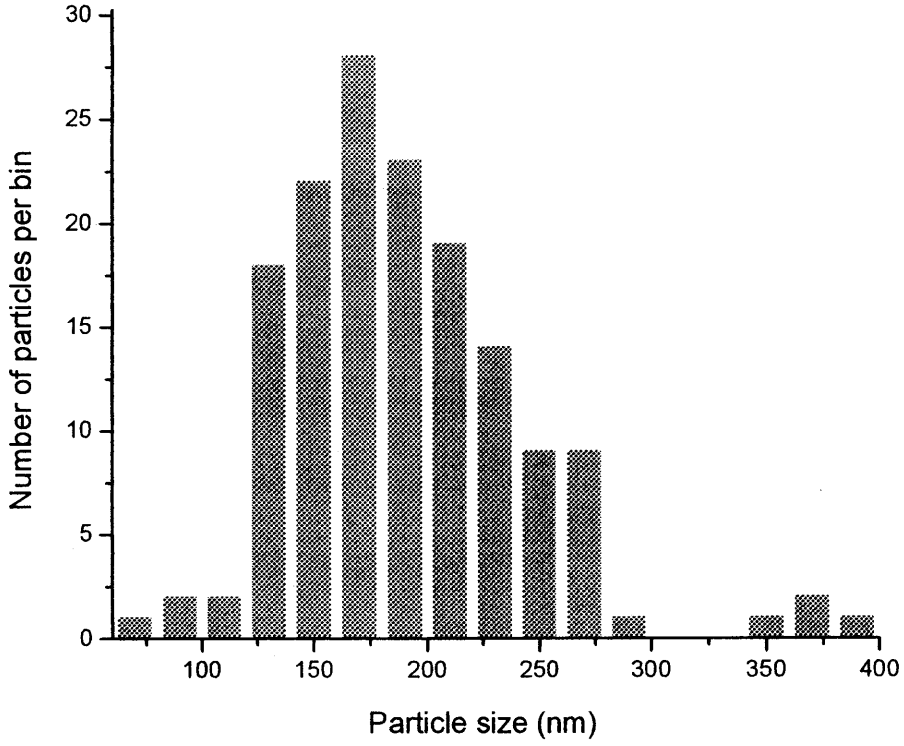

Figure 4.12 Size distribution of RDX particles formed by RESS determined by the SEM images.

4.3.5 Effect of Pre-expansion Pressure and Temperature of Saturator

So far the particle formation in RESS has been considered as a consequence of homogeneous nucleation. The homogenous nucleation takes place in supersaturated conditions. According to the homogeneous nucleation theory, the critical nucleus size becomes smaller at higher supersaturations, which results in smaller size of the final particles. Because the solubility of RDX in supercritical CO_2 changes with temperature

and pressure, the degree of supersaturation and the final particle size would also depend upon temperature and pressure.

The saturator temperature dependence was investigated at 180 bar pre-expansion pressure. The resulting size distribution functions are shown in Figure 4.13. The curves shown in Figure 4.13 were obtained by smoothing the original plots by averaging of five adjacent points. The shapes of the size distribution functions are almost the same in this saturator temperature range. The particle size at the maximum of the distribution functions slightly increases when the saturator temperature increases from 80 °C to 110 °C at the pre-expansion pressure of 180 bar.

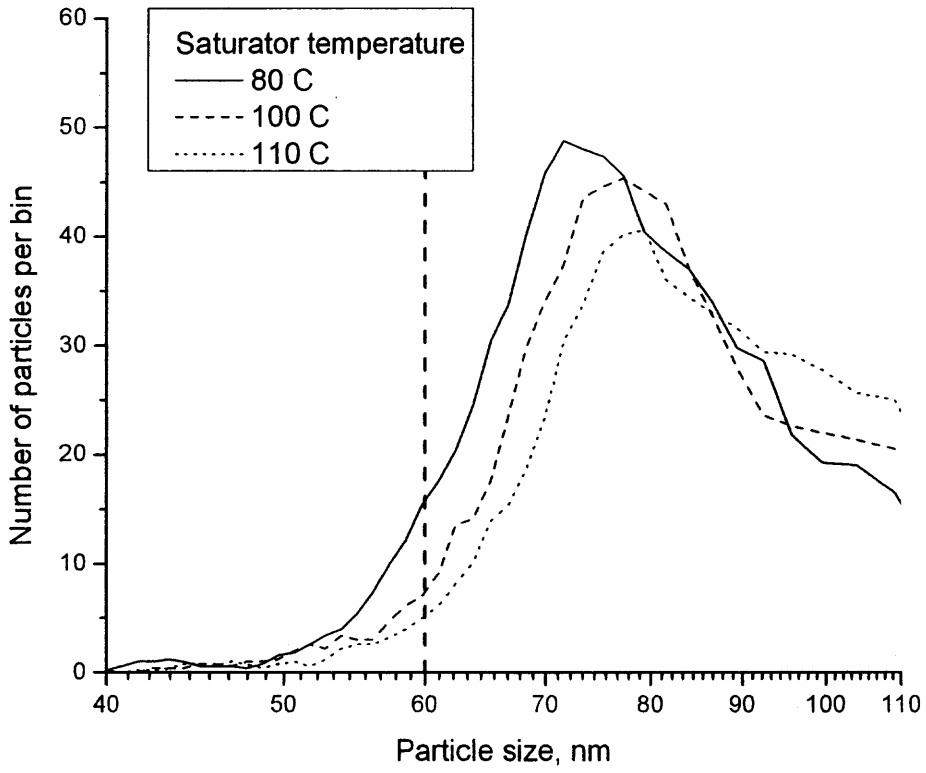

Figure 4.13 The size distribution functions of RDX particles at 69.5 mm from the nozzle along the RESS jet of the pre-expansion pressure of 180 bar and the different saturator temperatures. Solid line – 80 °C; dashed line – 100 °C; dotted line – 110 °C.

The intensity distributions of scattered light from particles formed at the pre-expansion pressure of 120 bar and a different saturation temperature are shown in Figure 4.14 (a)-(c). When the saturator temperature was 60 °C, the distribution functions were still changing and the peak is shifting toward lower intensity (Figure 4.14 (a)). This indicates that condensed CO_2 continues to evaporate even at 69.5 mm distance from the nozzle at these conditions. When the saturator temperature was 80 °C and 100 °C, only a few particles were observed in a frame (Figure 4.14 (b) and (c)). In fact, the number of particles per frame at the saturator temperature of 100 °C was approximately equal to the number of particles observed in the experiment on Rayleigh scattering from air, which means there was almost no observable RDX or RDX/CO_2 particle at the saturator temperature of 100 °C. This could be due to the negative temperature dependence of the solubility of RDX in supercritical CO_2 under such a low pressure, which means that the higher the temperature, the lower the solubility at constant pressure.[49,50] Therefore, the recovery of a reliable size distribution functions of RDX particles formed at 120 bar was not possible.

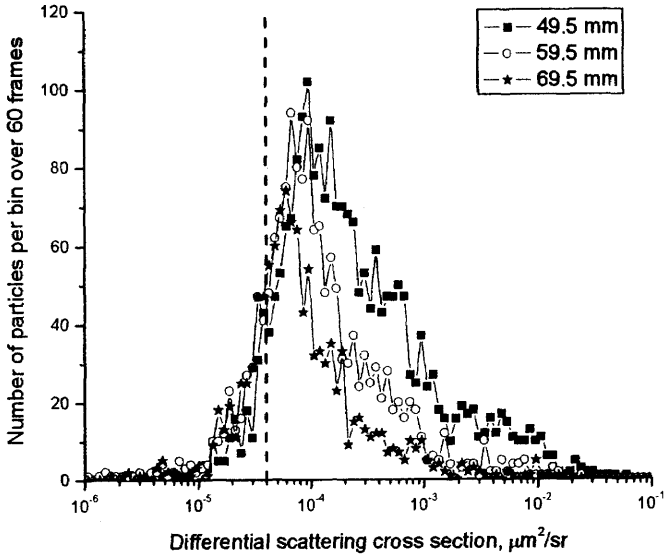

(a) Saturator temperature 60 °C

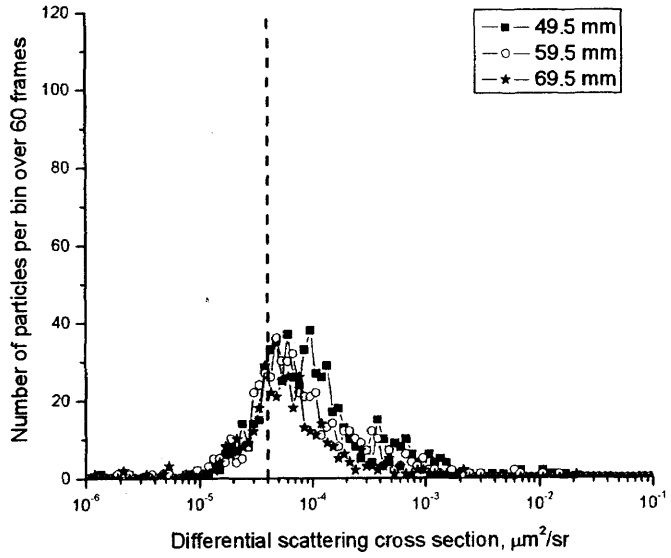

(b) Saturator temperature 80 °C

Figure 4.14 The intensity distributions of scattered light from particles formed at pre-expansion pressure 120 bar. (a) saturator temperature 60 °C; (b) saturator temperature 80 °C; (c) saturator temperature 100 °C.

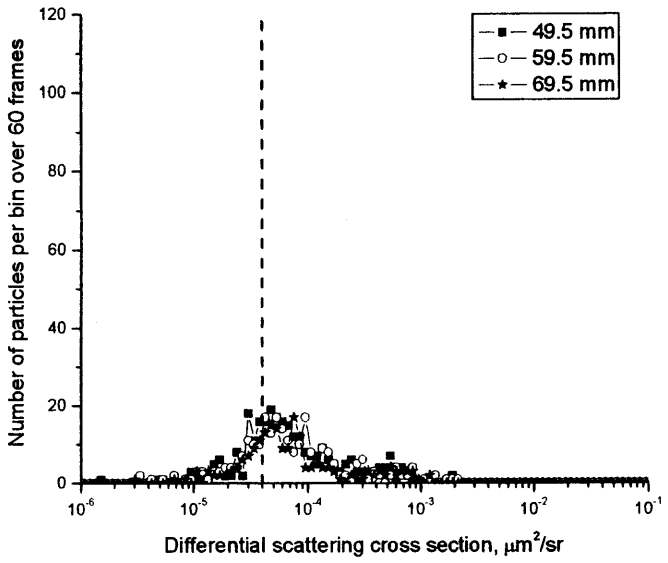

(C) Saturator temperature 100 °C

Figure 4.14 The intensity distributions of scattered light from particles formed at pre-expansion pressure 120 bar. (a) saturator temperature 60 °C; (b) saturator temperature 80 °C; (c) saturator temperature 100 °C. (Continued)

The intensity distribution functions of scattered light from RDX particles formed at pre-expansion pressure 140 bar are shown in Figure 4.15 (a)-(c). Although the "tails" on the right hand side of the distribution functions at these three conditions still change with the distance, the scattered intensities at the maximum of the functions remain constant.

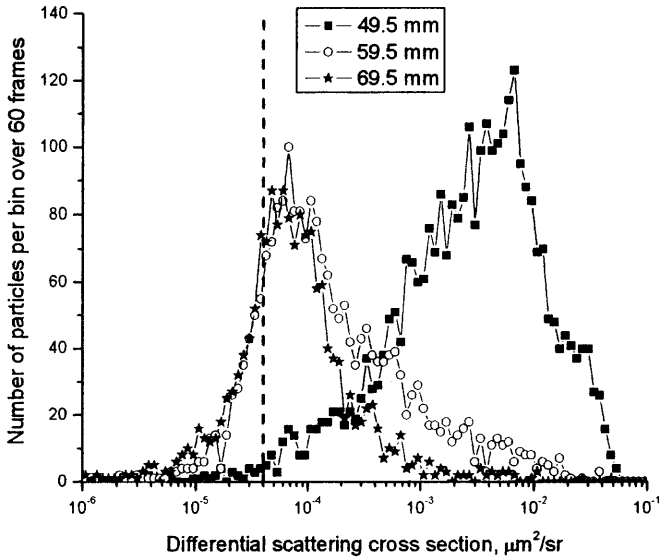

(a) Saturator temperature 60 °C

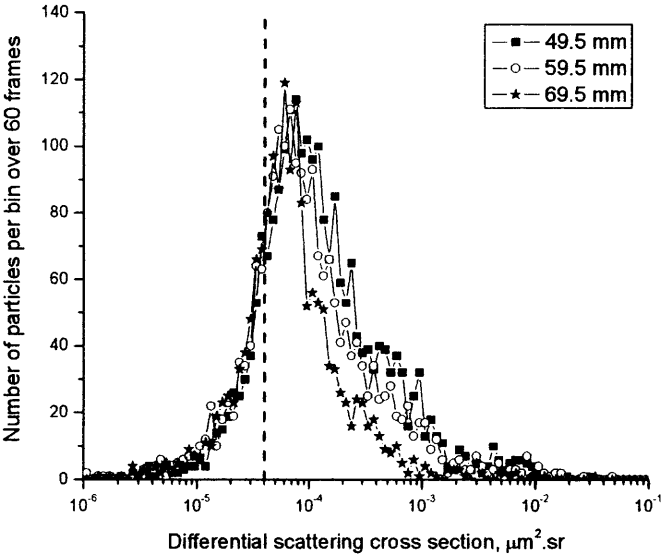

(b) Saturator temperature 80 °C

Figure 4.15 The intensity distributions of scattered light from particles formed at pre-expansion pressure 140 bar. (a) saturator temperature 60 °C; (b) saturator temperature 80 °C; (c) saturator temperature 100 °C.

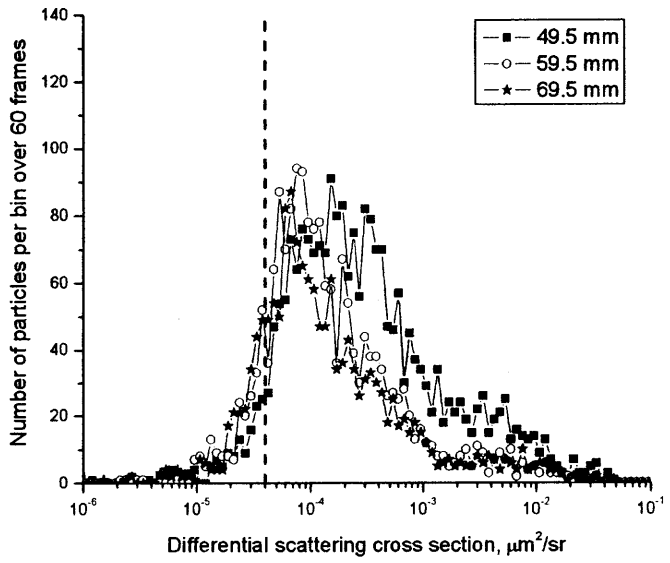

(C) Saturator temperature 100 °C

Figure 4.15 The intensity distributions of scattered light from particles formed at pre-expansion pressure 140 bar. (a) saturator temperature 60 °C; (b) saturator temperature 80 °C; (c) saturator temperature 100 °C. (Continued)

The particle diameters at the maximum of the size distribution functions determined in this study are listed in Table 4.1. The particle size increases with the saturation temperature and pre-expansion pressure of the RESS conditions investigated. However, the changes in the particle size are not large and comparable with the experimental error.

Table 4.1 Diameter of RDX Nanoparticles Determined by the *in situ* Method

	60 °C	80 °C	100 °C	110 °C
120 bar	< 60 nm	< 60 nm	< 60 nm	
140 bar	64 nm	66 nm	69 nm	
180 bar		72 nm	77 nm	79 nm

There are several sources of errors in the particle size determination. The major contributions to the errors are the sensitivity determination and the fluctuations of laser energy. The sensitivity error has already been evaluated in Chapter 3 as ± 20 %. The fluctuation of laser energy was assessed by statistically analyzing 30 frames of Rayleigh scattering images. The error associated with the fluctuation of laser energy was ± 18 %. Taking into account both errors using the equation given as

$$\frac{E_{sca}}{I_{sca}} = \sqrt{\left(\frac{E_m}{m}\right)^2 + \left(\frac{E_i}{I_i}\right)^2} \tag{4.1}$$

where E_{sca}, E_m, and E_i are absolute errors for scattered light intensity I_{sca}, sensitivity m, and energy of incident laser I_i, respectively, the error of the scattered light intensity was estimated to be ± 27 %. This is equivalent to ± 4 nm for RDX nanoparticles of 70 nm diameter. The trend of the particle size with the pre-expansion pressure is still recognized even after considering the systematic error in the size determination process. This trend will be explained based on the particle formation mechanism suggested in Chapter 7.

4.3.6 The Monte-Carlo Approach for Modelling an Ensemble of Particles

The size distribution of particles formed near the nozzle (particles of condensed CO_2 particles) could not be recovered from the optical measurements by the method described above because the oscillations in the differential scattering cross sections become much more significant for the large particle sizes (Figure 2.1 (b)) (the inverse light scattering problem). Therefore, a different approach described below was used.

Since the inverse light scattering problem has non-unique solution in a particular region of diameters, the parameters of the distribution function were determined assuming a particular shape of the distribution function, namely the log-normal distribution $L(d)$:

$$L(d) = \frac{A}{\Omega\sqrt{2\pi}} \exp\left(-\frac{(\ln d - \ln \mathrm{M})^2}{2\Omega^2} \right)\left(\frac{1}{d}\right) \tag{4.2}$$

where M and Ω are the parameters of the log-normal distribution, A is area below the curve, and d is the particle diameter. An ensemble of particles could be modeled using either the method of histograms[51] or the Monte-Carlo approach.[52] In this study the Monte-Carlo approach was chosen because it is much faster and the precision of the method is not limited by the number and the size of bins in the histograms. The theoretical statistical error can be easily estimated by simulating several independent random ensembles and compared with the statistical error of the experimental data obtained by repeated experiments.

The Monte-Carlo approach was used as follows. An ensemble of 10^5 particles with the same refractive index and random diameters was simulated using an uniform random number generator. Then, for given values of M and Ω, Equation 4.2 was used to

assign statistical weights to each particle. This statistical weight was taken into account when building the distribution of the particles with respect to their differential scattering cross sections. Varying the values of M and Ω and using the Levenberg-Marquardt non-linear least squares fitting algorithm,[53] the best fit to the experimental data was performed.

4.3.7 The Size Distributions Determined by Monte-Carlo Approach

The theoretical distributions of differential scattering cross section of particles determined using the Monte-Carlo approach were compared with the experimental data from the measurements near the nozzle (7.5 mm from the nozzle) and far from the nozzle (69.5 mm from the nozzle) (Figure 4.16). The tails of the experimental distribution function obtained near the nozzle as well as far from the nozzle could not be fitted by log-normal functions. It means that the true particle size distributions were not exactly lognormal distributions.

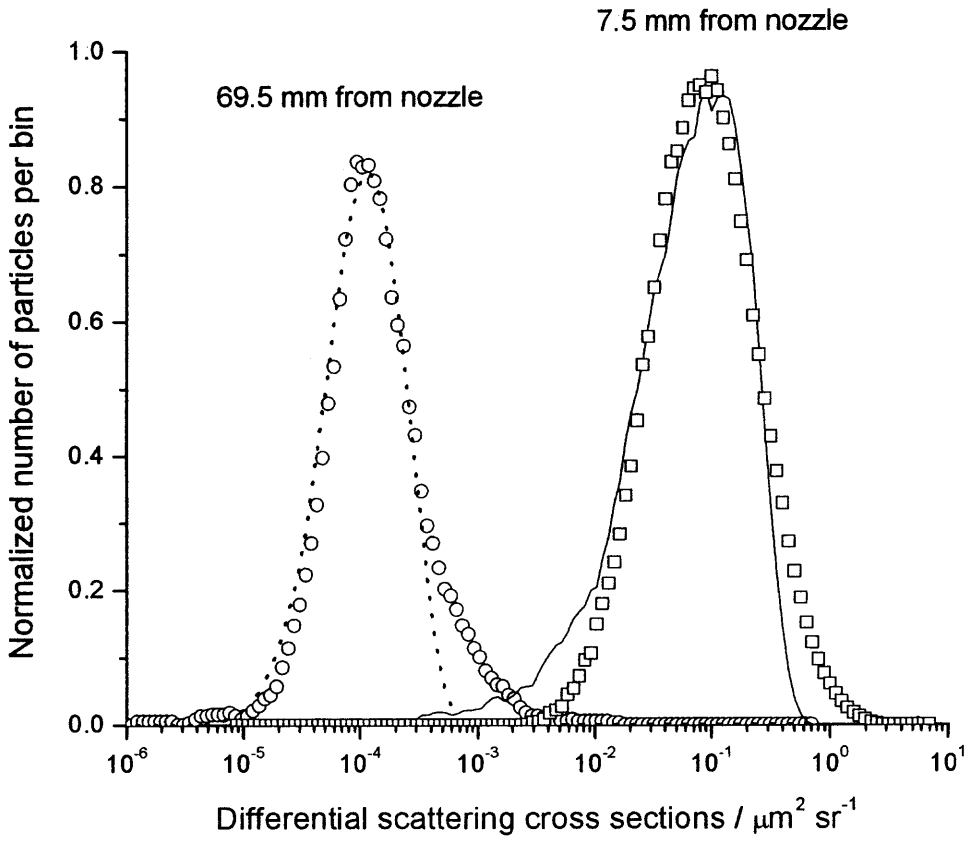

Figure 4.16 Comparison of the experimental distributions of the differential scattering cross section with the theoretical distributions using the Monte-Carlo approach. Open squares – the experimental data at the distance of 7.5 mm from the nozzle; open circles – the experimental data at the distance of 69.5 mm from the nozzle; solid line – the fitting curve to the experimental data at the distance of 7.5 mm from the nozzle; dotted line – the fitting curve at the distance of 69.5 mm from the nozzle.

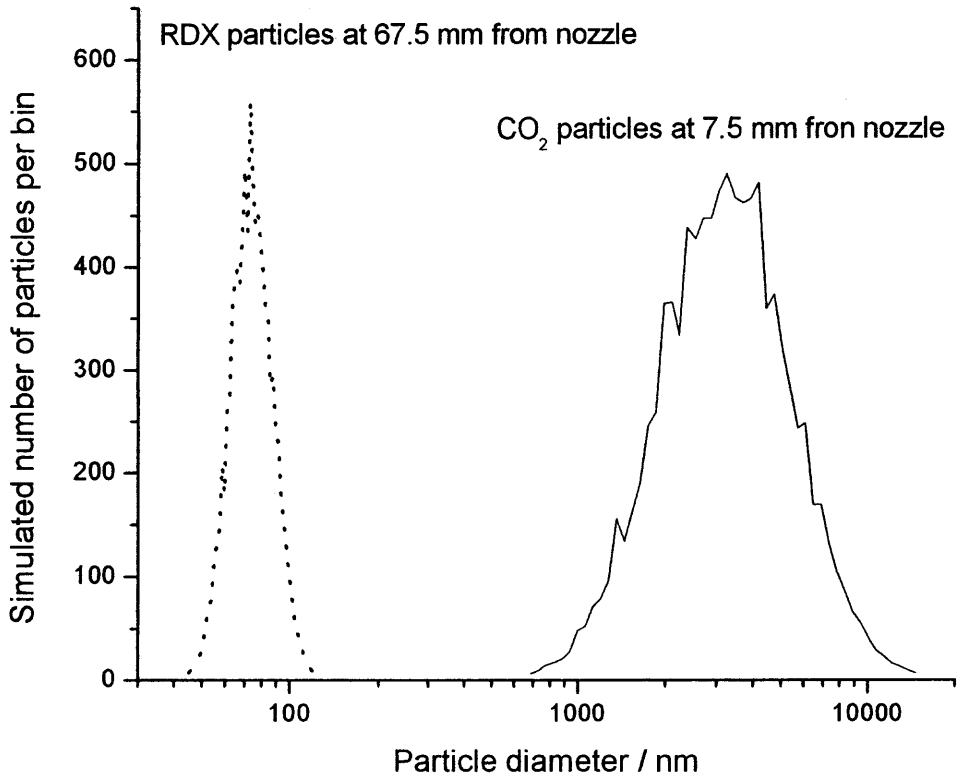

Figure 4.17 The particle size distributions determined using the Monte-Carlo approach for CO_2 particles at the distance of 7.5 mm from the nozzle (solid line) and RDX particles at the distance of 69.5 mm from the nozzle (dotted line).

Nevertheless, as the particle sizes at the maximums of the distributions were still valid, it was estimated that the particle size consisting of CO_2 with small amount of RDX at the maximum in the distribution was 3.3 μm in diameter at the 180 bar RESS pre-expansion pressure and the RDX particle size at the maximum was 73 nm (Figure 4.17). The RDX particle size determined using the Monte-Carlo approach is in agreement with the particle size determined using the direct method in Figure 4.11.

4.3.8 TEM Analysis of RDX Nanoparticles Formed by RESS

The RDX nanoparticles formed by RESS were characterized by transmission electron microscopy (TEM) using 200 kV accelerating voltage. Figure 4.18 presents the TEM image for RDX nanoparticles prepared by RESS at the pre-expansion pressure of 180 bar, the saturator temperature of 80 °C and the nozzle temperature of 140 °C.

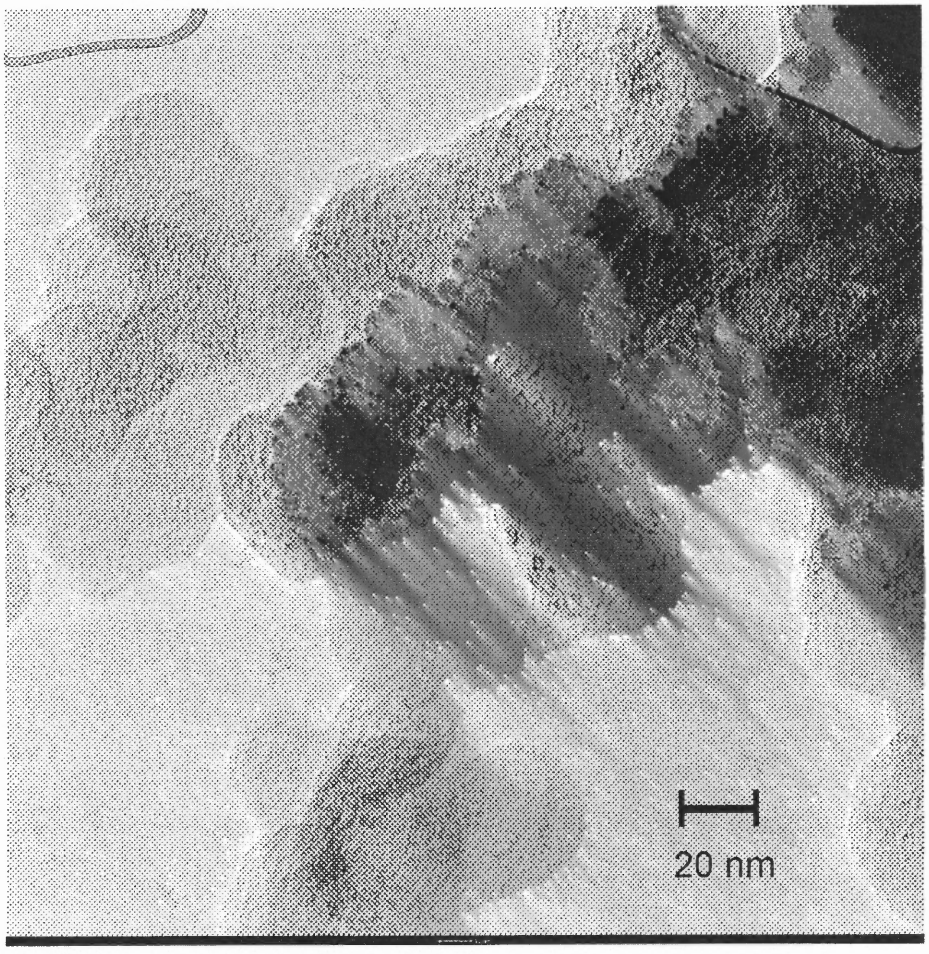

Figure 4.18 A sample of TEM image of RDX particles formed by the RESS at pre-expansion pressure 180 bar, saturator temperature 80 °C and nozzle temperature 140 °C.

The image shows agglomeration of ellipsoidal or quasi-hexagonal shaped particles with the aspect ratio approximately of 3:4. The hexagonal shape is often seen as (200) plane of RDX crystals grown from some liquid (Figure 4.19).[5] The average lengths on the long axis and the short axis were 63 ± 4 nm and 44 ± 5 nm, respectively. The particle size observed in Figure 4.18 is somehow smaller than the size determined by the *in situ* characterization. Because of the very limited number of particles in the TEM image, the comparison with the *in situ* method was not conclusive. Still, based on this TEM image, it becomes clear that the RDX particles around 60 nm diameter are formed by RESS, and these particles participate in formation of larger clusters.

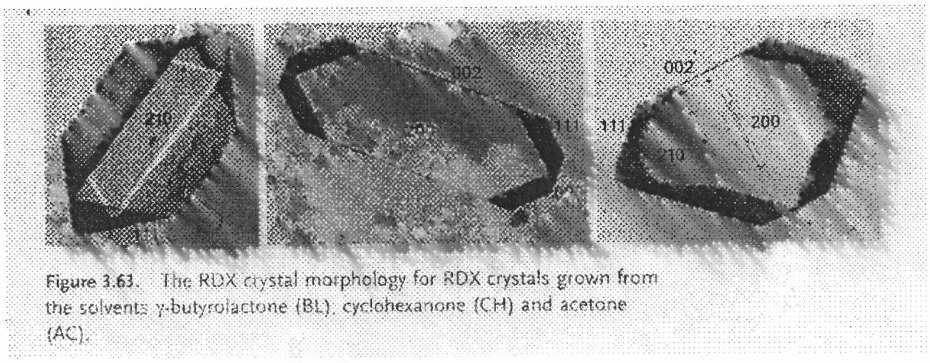

Figure 3.63. The RDX crystal morphology for RDX crystals grown from the solvents γ-butyrolactone (BL), cyclohexanone (CH) and acetone (AC).

Figure 4.19 RDX single crystals grown from different solvents.[5]

4.4 Summary

Using the light scattering imaging system, the particles formed in RESS jet were successfully *in situ* monitored. The decrease in the scattering intensity along the RESS jet was assumed to be due to the evaporation of CO_2 downstream the jet. The particle size distribution functions for RDX particles were determined from the intensity distributions. The particle sizes at the maximum of the distribution functions approximately ranged

from 60 nm to 80 nm at the pre-expansion pressure of 140 bar and 180 bar, the conditions at which all condensed CO_2 are thought to be evaporated. Although the particle size does not change much over the range of the pre-expansion pressures and the saturator temperatures investigated in this research, it becomes slightly smaller at lower pre-expansion pressures.

The comparison to the particle sizes determined from SEM images gives the discrepancy of the mean RDX particle size, which may be due to the sampling size discrimination in the sample collection for SEM analysis. Although no particles smaller than 70 nm observed in the SEM images, the TEM image shows the agglomeration of particles of about 60 nm length. The result of TEM analysis supports existence of such small particles comparable with those observed by the *in situ* optical method.

CHAPTER 5

NUMBER DENSITY OF RDX PARTICLES IN THE RESS JET

5.1 Introduction

The number density of particles formed by RESS has not been previously determined experimentally, to the best of our knowledge. The approach used in this research makes it possible to determine the number density of particles based on the particle-by-particle treatment of the images. It is important to know the number density profile of particles in the RESS jet for establishing the mechanism of particle formation in the RESS process, which is generally assumed to be homogeneous nucleation with subsequent particle agglomeration.

As seen in Chapter 4, the decrease in the particle size downstream the jet was observed but no particle growth. If the subsequent particle agglomeration occurs as suggested in the literature, the number density of the particles should be decreased downstream the jet. There are three possible factors to influence the profile of the number density of particles: new particle formation, particle agglomeration, and dilution by air (the air entrainment). In this chapter, the number density of RDX particles was determined by processing the data described in Chapter 4. Then the air entrainment effect was evaluated based on the temperature measurements and Raman scattering spectroscopy.

5.2 Determination of Number Density of RDX Particles in RESS Jet

5.2.1 Procedure

The number densities of particles along the RESS jet at two different conditions were investigated: (1) at the pre-expansion pressure of 180 bar; the saturator temperature of 80 °C; the nozzle temperature of 140 °C, and (2) the pre-expansion pressure of 90 bar; the saturator temperature of 60 °C; the nozzle temperature of 80 °C. The number densities were determined by dividing the number of particles per frame by the sampling volume of the laser light scattering. Near the nozzle, the spot counting software underestimated the number of particles (due to the partial overlap of the spots) as compared to manual counting. The correction factor as a function of the distance along the jet was introduced to correct for this effect.

5.2.2 Results and Discussion

The number densities for the RESS at the 180 bar and 90 bar pre-expansion pressures were given in Figure 5.1. In both cases the observed number densities decreased rapidly downstream the jet. This could be partially or completely due to the air entrainment into the jet. For the 180 bar pre-expansion RESS the number density became almost constant after 40 mm distance from the nozzle, while for the 90 bar the number density became close to zero. This is because the particles observed in the RESS at the 90 bar pre-expansion pressure are too small to be detected after the distance 35 mm from the nozzle.

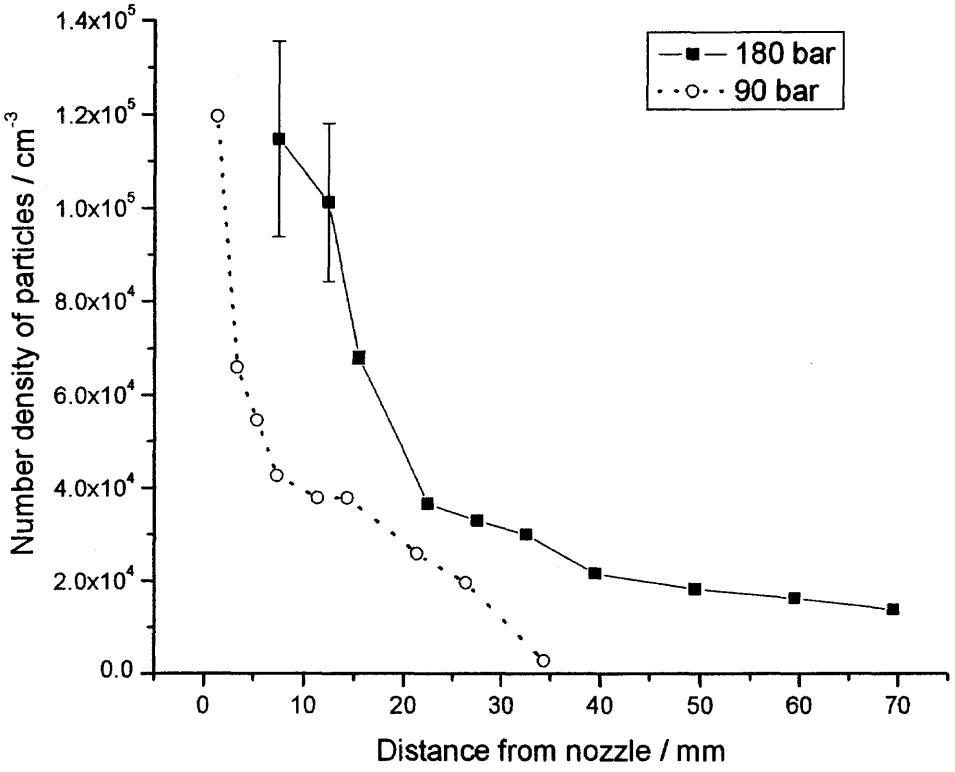

Figure 5.1 The number density of particles as a function of distance from the nozzle along the jet. Filled squares – pre-expansion pressure 180 bar; saturator temperature 80 °C; nozzle temperature 140 °C. Open circles – pre-expansion pressure 90 bar; saturator temperature 60 °C; nozzle temperature 80 °C.

5.3 Temperature Profiles in RESS Jet

5.3.1 Experimental

Temperature in the RESS jet was determined using a K-type thermocouple made of chromel and alumel wires with the diameter of 0.1 mm as described in Chapter 4. Both wires were connected to the multimeter to measure the voltages at the different positions along the jet. The voltage relative to the reference junction at room temperature was

measured. Then, the temperature was determined from the tabulated dada of temperature – voltage at 0 °C reference junction.[47]

5.3.2 Results and Discussion

Figure 5.2 presents temperature profiles of RESS jets at the pre-expansion pressure of 180 bar and 90 bar. In both profiles the temperature rises downstream the jets. This trend in the temperature profiles can be explained based on the air entrainment by the jets.

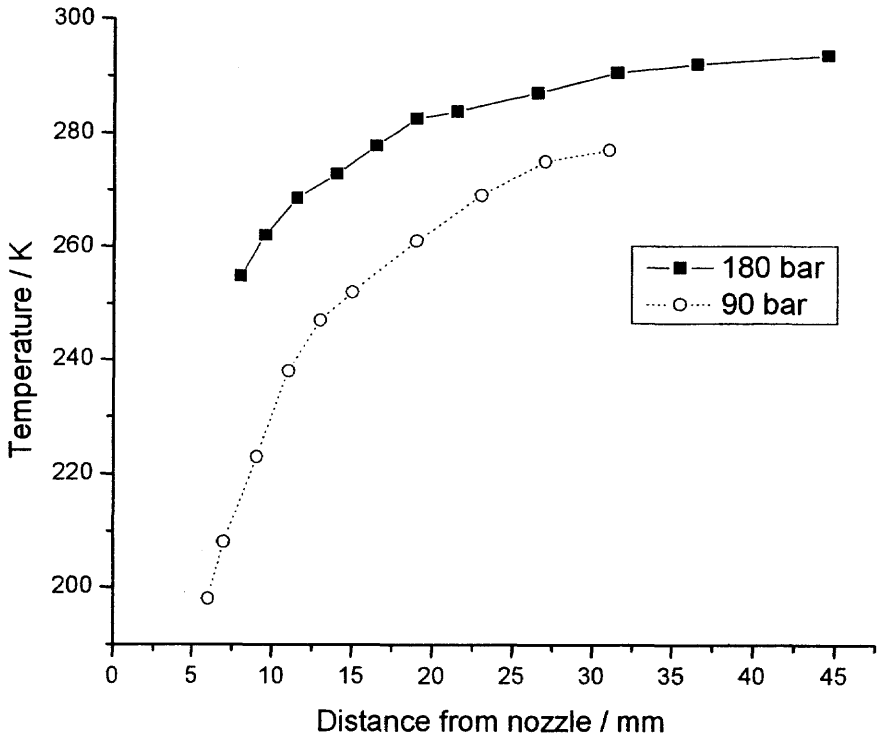

Figure 5.2 The temperature profiles along the RESS jet with RDX under two conditions. Filled squares – pre-expansion pressure 180 bar; saturator temperature 80 °C; nozzle temperature 140 °C. Open circles – pre-expansion pressure 90 bar; saturator temperature 60 °C; nozzle temperature 80 °C.

5.4 Raman Scattering Spectroscopy

5.4.1 Rayleigh Scattering and Raman Scattering

When photons are scattered by molecules elastically, the process is called Rayleigh scattering. On the other hand, when photons are scattered by molecules inelastically, the process is called Raman scattering. In Raman spectroscopy, frequencies corresponding to the energy gap between an incident photon and a scattered photon are measured. Figure 5.3 shows an illustration of vibrational and rotational energy level diagram. The thick lines in Figure 5.3 depict the excitation and de-excitation of a molecule to a virtual state when the molecule elastically interacts with a photon (Rayleigh scattering). In Raman scattering, the excited molecule falls down to the first excited vibrational state.

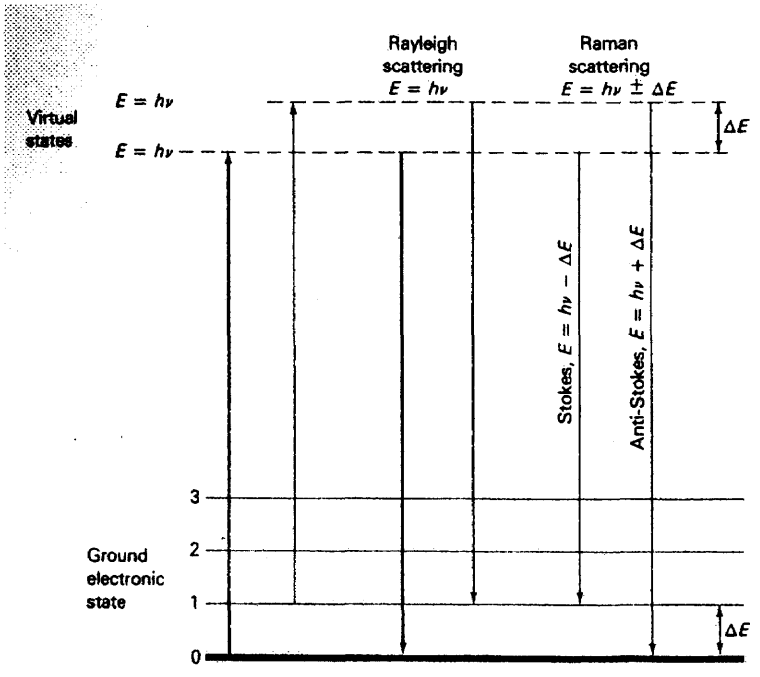

Figure 5.3 Origin of Rayleigh and Raman scattering.[54]

The scattered photon produced in this case has energy equal to the incident photon energy minus the energy gap between the ground state and the first excited vibrational state. The energy gap is called the Raman shift, which is usually expressed in frequency units. This process is known as Stokes scattering.

There is also another case that a molecule which is originally in the first excited vibrational state is excited to the virtual state by the incident photon and falls down to the ground vibrational state producing a photon with the energy equal to the incident photon energy plus the energy gap. This is known as anti-Stokes scattering. The anti-Stokes scattering is weak compared to the Stokes scattering at room temperature. In this study, Stokes scattering was used to evaluate air entrainment into the jet.

5.4.2 Raman Scattering from CO_2 Gas

There are three vibration modes in CO_2 molecules: C-O asymmetric stretching, C-O symmetric stretching, and doubly degenerate O-C-O bending. Only the C-O symmetric stretching mode is active in Raman scattering, which is split into 1388.15 cm^{-1} and 1285.40 cm^{-1} of Raman shift.[55] The split of the C-O symmetric stretching is due to Fermi resonance[56] (the vibrational state of C-O symmetric stretching splits into two different energy states due to a resonance with the overtone of the O-C-O bending).

5.4.3 Experimental

The experimental setup for the Raman measurements was slightly modified compared to the setup shown in Figure 5.4. In these experiments the ICCD camera was mounted on a spectrograph (SpectraPro-300i, Acton Research Corporation). The light scattered in the

jet was guided into the spectrograph. A laser light rejection filter (UV steep edge filter, Barr Associates, Inc.) which blocks more than 99.99 % of light at 248 nm was installed before the entrance slit of the spectrograph. The slit width was 50 μm, which corresponds to the spectral resolution of 1.1 nm.

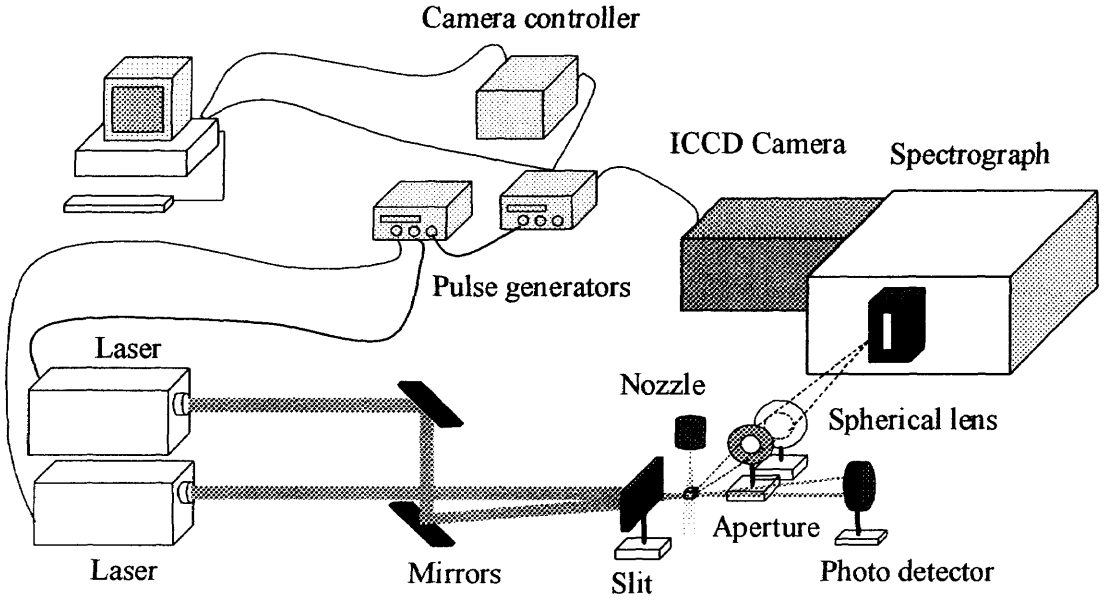

Figure 5.4 Experimental set up for Raman scattering.

5.4.4 Results and Discussion

The Raman spectra of CO_2 (Q-branches) at different locations downstream the RESS jet are shown in Figure 5.5. The Raman shift for CO_2 is 1388 cm^{-1} and 1285 cm^{-1}, which correspond to the vibration mode of C-O symmetric stretching split by the Fermi resonance.[55]

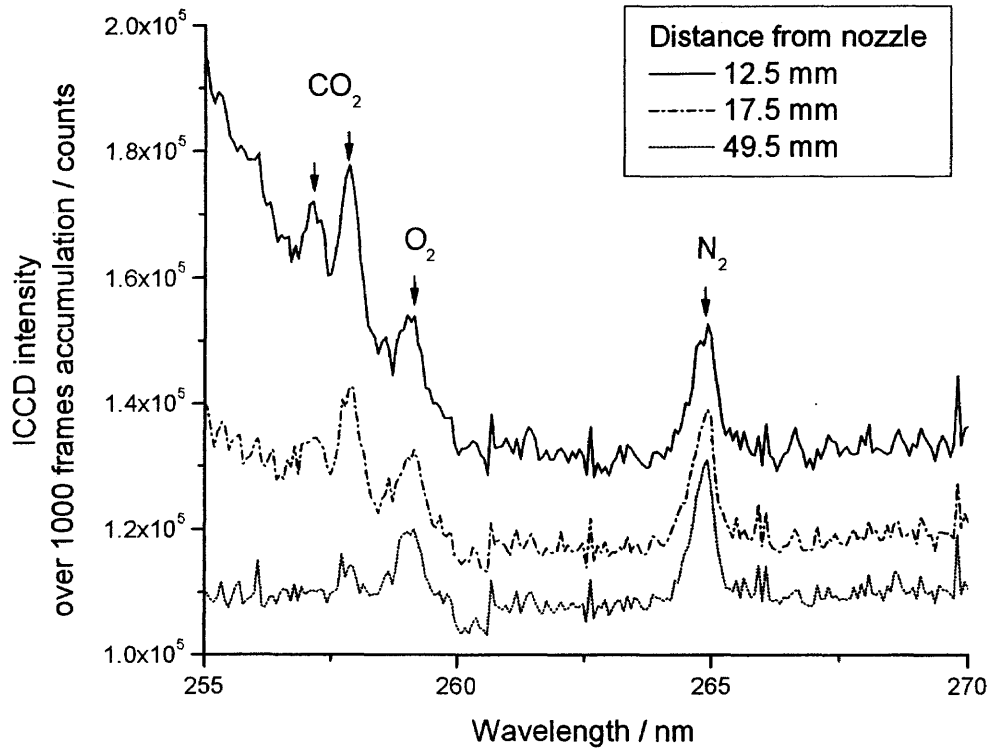

Figure 5.5 Raman spectra at the different positions from the nozzle. Solid line – 12.5 mm from the nozzle; dash-dotted line – 17.5 mm from the nozzle; dotted line – 49.5 mm from the nozzle.

5.5 Correction of the Number Density of Particles by Air Entrainment

5.5.1 Mole Fractions of CO_2

Estimates show that the jet "heating" due to the thermal conductivity could be neglected. Assuming pressure in the jet equal to ambient (1 atm) and the temperature rise solely due to the air entrainment, the mole fraction of CO_2 is given by:

$$x_{CO_2} = \frac{T_0 - T(z)}{T_0 - T_i} \tag{5.1}$$

where T_0, T_i, and $T(z)$ are the temperature of surrounding air, the initial temperature (temperature right after the nozzle), and the temperature of the jet at the axial point z, respectively (Appendix C). Taking into account the volume change due to the

temperature rise by the ratio of T_i to $T(z)$, the number density of particles corrected for the air entrainment is given by

$$n_{cor}(z) = \frac{n(z)}{x_{CO_2}}\left(\frac{T(z)}{T_i}\right) = n(z)\left(\frac{T(z)}{T_i}\right)\left(\frac{T_0 - T_i}{T_0 - T(z)}\right) \tag{5.2}$$

where $n(z)$ is the observed number density. The corrected number density defined by Equation 5.2 refers to the hypothetical number density of particles at $z = 0$ (where the jet consists of pure CO_2 with no air entrainment yet).

Based on the Raman spectroscopy of the RESS jet, the mole fraction of CO_2 is:

$$x_{CO_2} = \frac{I^{Raman}(z)}{I_0^{Raman}}\left(\frac{T(z)}{T_0}\right) \tag{5.3}$$

where $I^{Raman}(z)$ and I_0^{Raman} are the intensities of Raman peaks of CO_2 at the axial point z along the jet and in pure CO_2 at room temperature T_0, respectively. Equation 5.3 also incorporates the temperature correction factor for the number density based on the ideal gas law. The temperature dependence of the differential Raman scattering cross sections in the Q-branch in the temperature range of these experiments was neglected.

Figure 5.6 shows the mole fractions of CO_2 along the RESS jet at the pre-expansion pressure of 180 bar calculated from Equations 5.1 and 5.3. Both results are in good agreement after 17.5 mm from the nozzle. There is a discrepancy between the two results near the nozzle. The reason for this discrepancy was not established with certainty. One reason could be that at short distances from the nozzle, a significant fraction of CO_2 could be in condensed phase. Another reason could be the error caused by the overwhelming tail of the Rayleigh scattering by the turbulence flow at these distances. Nevertheless, at the distances longer than 17.5 mm, the results of Raman measurements agree with the conclusion that the temperature rise in the jet is due almost solely to the dilution of CO_2 by air entrainment downstream the jet.

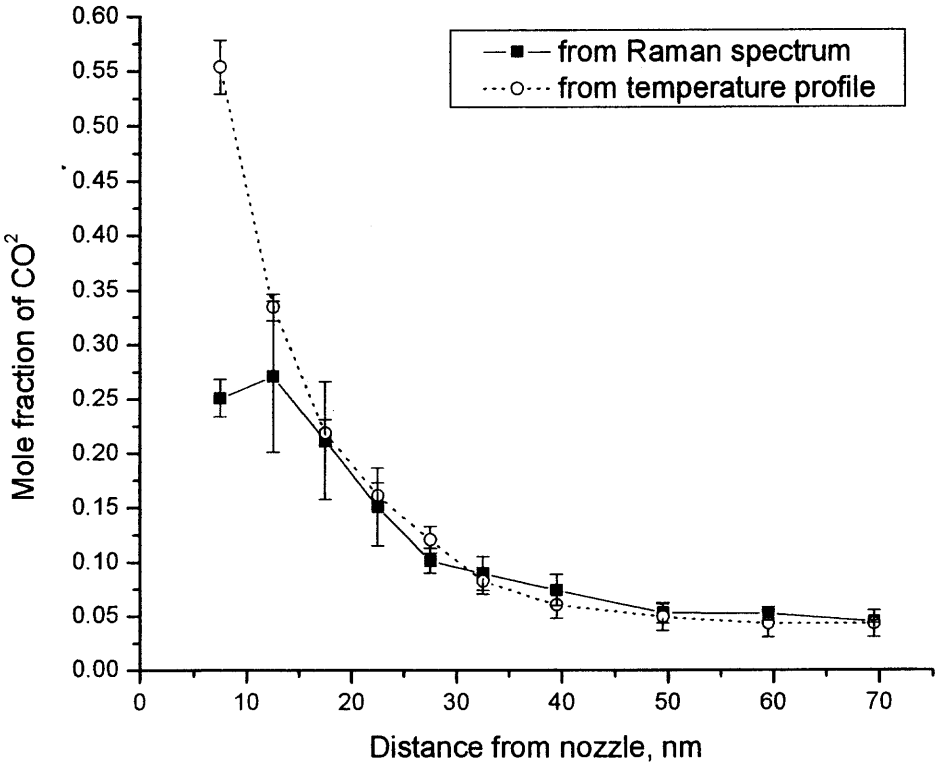

Figure 5.6 The mole fraction of CO_2 as a function of distance from the nozzle along the RESS jet. Filled squares – the mole fraction of CO_2 determined from Raman scattering measurements; open circles – the mole fraction of CO_2 determined from the temperature measurements along the RESS jet.

5.5.2 Correction of the Number Density of Particles in the RESS Jet

It was found that the corrected number densities calculated using Equation 5.2 do not change along the RESS jet, as shown in Figure 5.7. As described in Section 5.5.1, the treatment of Raman scattering peaks for CO_2 at 7.5 mm from the nozzle is not reliable enough to correct the number density of particles by the mole fraction of CO_2. From the independence of the corrected number density along the jet, it is concluded that there is no noticeable particle-particle agglomeration occurring in the region investigated and the decrease of the apparent number density along the stream is due to the air entrainment.

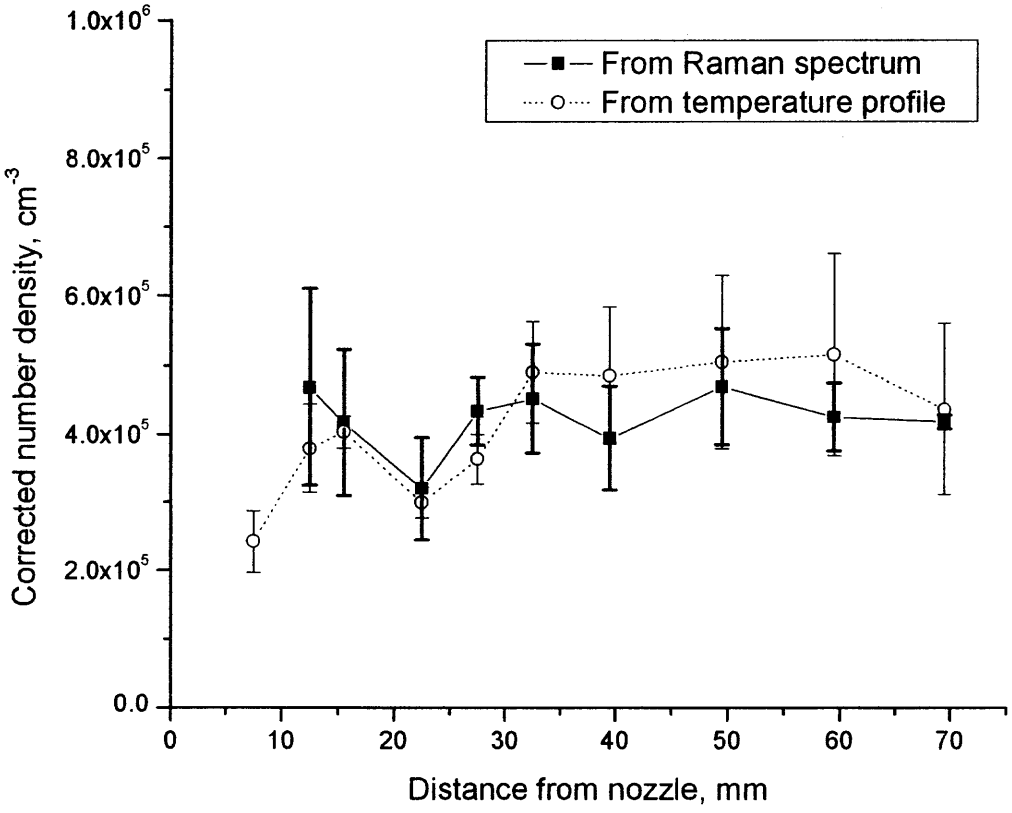

Figure 5.7 The corrected number density of particles as a function of the distance from the nozzle along the RESS jet at pre-expansion pressure 180 bar. Filled squares – the number densities corrected based on the Raman spectroscopy; open circles – the number densities corrected based on the temperature profile of the jet.

5.6 Summary

To the best of our knowledge, the experiments described above are the first direct determination of the number density of particles along the RESS jet without any assumptions. The decrease in the number density of particles was attributed to the air

entrainment by the jet leading to the dilution of the jet and, subsequently, reduction of the particle concentration. This was confirmed by assessing the number density of the particles via the temperature measurement and the Raman spectroscopy along the RESS jet. There is no variation of the number density along the jet after correction for the air entrainment. This is one of the most important conclusions of this research because it gives us a hint of a particle formation mechanism in the RESS. As described in Chapter 1, theoretical studies of the particle formation in RESS were based on homogeneous nucleation. To explain the discrepancy between the experimental results and the model, the subsequent coagulation of particles was suggested. According to the results described here, such interactions between particles that can change the number of particles are not occurring at least in the observation range investigated (7.5 mm – 69.5 mm from the nozzle).

CHAPTER 6

CRYSTALLOGRAPHIC ANALYSIS FOR RDX NANOPARTICLES

6.1 Basic Concept of X-ray Diffraction Analysis

6.1.1 Bragg's Equation

X-ray diffraction (XRD) is a useful characterization method for crystallography of materials. X-rays are electromagnetic radiation of wavelength about 1 Å, which is comparable to the length of several unit cells. Usually X-ray used in analysis is emitted by copper (Kα emission 1.5418 Å). One of the most important information obtained from XRD analysis is the distance between crystallographic planes. The distance between atomic layers in a crystal is related to the angle θ and wavelength λ of the incident X-ray according to Bragg's law:

$$n\lambda = 2d\sin\theta. \tag{6.1}$$

Bragg's law can be derived by considering the geometry of reflection of X-ray beam from the crystallographic plane (Figure 6.1). The second beam travels the extra distance AB+BC. For the two beams to be in phase, the extra distance must be a whole multiple of the wavelength λ:

$$n\lambda = \mathrm{AB} + \mathrm{BC} \tag{6.2}$$

Now that $\mathrm{AB} = \mathrm{BC} = d\sin\theta$, the Equation 6.1 is obtained.

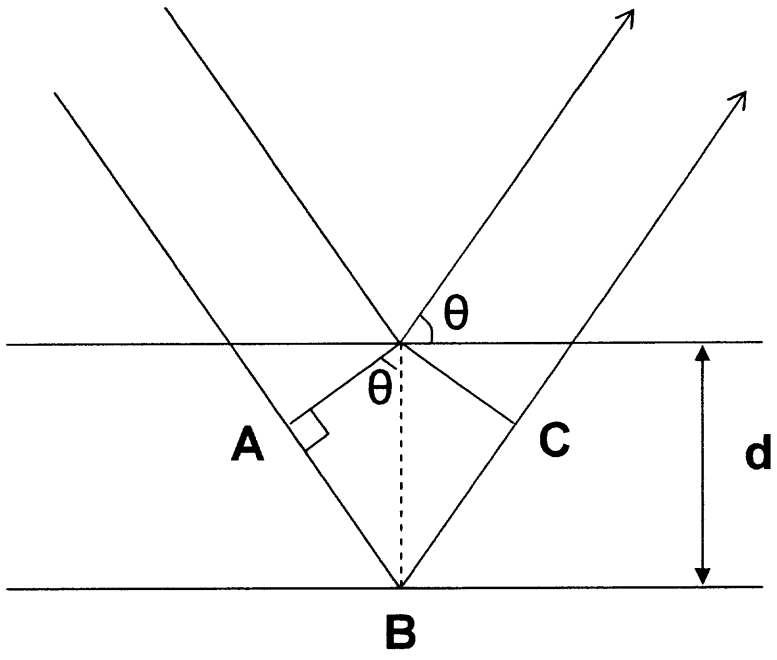

Figure 6.1 The geometry of reflection of X-ray beams.

6.1.2 Line Broadening in XRD Patterns

Scherrer observed first the broadening of diffraction lines caused by small size of crystallites.[57] According to his study, the relationship between the crystallite size and the broadening is expressed by the following formula:

$$D_v = \frac{K\lambda}{\beta_s \cos\theta} \tag{6.3}$$

where D_v is volume weighted crystallite size (column length), K is Scherrer constant, β_s is the contribution to the integral breadth in radians of a reflection at the diffraction angle 2θ due to the small size of the crystallite. K is usually taken 1. Stokes and Wilson studied the diffraction line broadening due to the strain field in imperfect crystals.[58] The contribution to the integral breadth β_{str} due to microstrain in crystals, based on their study, can be approximated as

$$\beta_{str} = 4\varepsilon \tan\theta \tag{6.4}$$

where ε is a measure of the microstrain. The microstrain usually originates from imperfection of crystals (defects). Assuming that the shapes of broadened diffraction patterns for both the size and the strain components are Lorentzian, the total integral breadth (defined as the ratio peak area / peak height) is obtained by adding the two contributions:

$$\beta_t = \beta_s + \beta_{str}\,. \tag{6.5}$$

From Equations 6.3 - 6.5, the following equation is obtained

$$\frac{\beta_t \cos\theta}{\lambda} = \frac{1}{D_v} + \frac{4\varepsilon \sin\theta}{\lambda} \tag{6.6}$$

It should be noted that β_t is the integral breadth of the broadening purely due to the crystallite size and the microstrain in crystals and should be determined by subtracting the contribution due to the instrument broadening from the actual diffraction profile measured by a diffractometer. The instrument broadening is usually evaluated by measuring an X-ray diffraction pattern of a standard material such as lanthanum hexaboride (LaB_6) and is subtracted linearly from the integral breadth determined from the X-ray diffraction pattern of sample crystals. By plotting $\beta_t \cos\theta/\lambda$ versus $4\sin\theta/\lambda$, the volume weighted crystallite size D_v and the microstrain ε are determined. This is called the William-Hall plot.[59]

6.1.3 RDX Crystallographic Data and X-ray Diffraction Data

RDX forms orthorhombic crystals having the cell dimensions: a=11.61 Å, b=13.18 Å, c=10.72 Å.[60] The X-ray diffraction angle and corresponding Miller indices of RDX crystal are listed in Table 6.1.

Table 6.1 X-ray Diffraction Data of RDX[61]

2θobs	dobs	Ical	Iobs	h	k	l
13.085	6.7604	55	86	1	1	1
13.487	6.5987	23	22	2	0	0
15.251	5.8048	4	4	0	2	0
15.437	5.7353	25	26	2	1	0
16.539	5.3555	15	15	0	0	2
17.387	5.0952	48	49	0	2	1
17.865	4.9609	63	64	1	0	2
18.664	4.7503	2	2			
20.389	4.3521	40	41	2	2	0
21.361	4.1562	4	4	2	0	2
22.008	4.0355	35	34	2	2	1
22.581	3.9343	6	9	0	2	2
		4		2	1	2
23.576	3.7705	7	7	1	2	2
25.360	3.5092	38	40	1	3	1
26.194	3.3999	2	2	3	0	2
26.721	3.3334	7	7	3	2	1
26.957	3.3048	24	38	1	1	3
		14	14	4	0	0
27.304	3.2636	9		3	1	2
29.291	3.0465	33	100	1	3	2
		46		4	1	1
		21		0	2	3
30.423	2.9357	18	18	3	2	2
30.779	2.9026	8	7	0	4	0
31.135	2.8702	12	10	4	2	0
31.544	2.8339	4	2	2	3	2
31.904	2.8027	7	8	0	4	1
32.328	2.7669	17	39	4	2	1
		22		2	2	3
32.726	2.7342	2	4	4	1	2
		1		1	4	1
33.191	2.6969	12	11	3	1	3
34.109	2.6264	2	2	1	0	4
34.810	2.5751	5	18	2	4	1
		13		1	3	3
35.111	2.5537	16	21	3	3	2
		4		0	4	2
35.743	2.51	6	6	4	3	0
36.865	2.4362	6	18	2	3	3
		11		0	2	4
38.014	2.3651	4	15	5	0	2
		12		3	4	1
39.450	2.2823	4	3	2	2	4
40.094	2.2471	3	2	3	1	4
40.961	2.2015	3	2	6	0	0
41.787	2.1599	3	2	6	1	0
42.353	2.1318	2	4	2	4	3
		2		3	2	4

6.2 X-ray Diffraction Analysis for RDX Nanoparticles

6.2.1 Experimental

The RDX nanoparticles were prepared by RESS process at the pre-expansion pressure of 280 bars, the saturator temperature of 80 °C, and the nozzle temperature of 120 °C. The production grade RDX was used as the precursor material. Figure 6.2 presents typical RDX crystals used in this research.

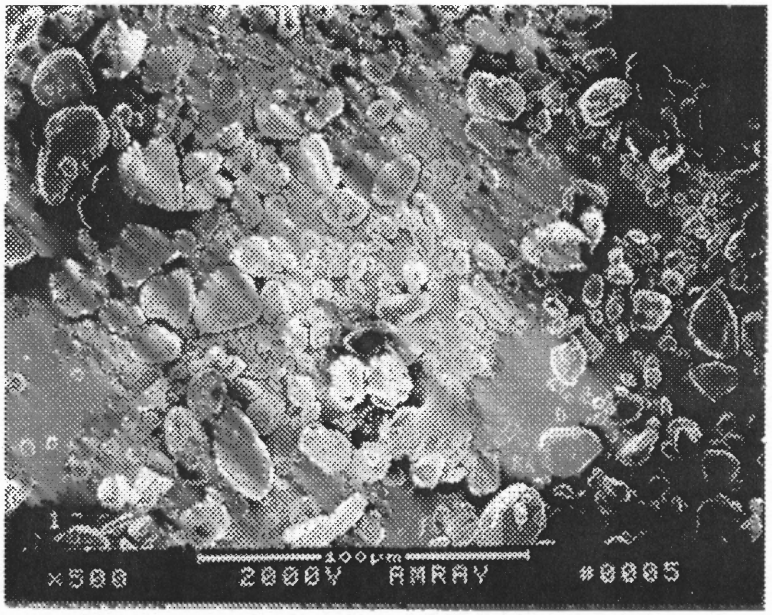

Figure 6.2 Typical production grade RDX crystal (SEM).

The crystallographic structure of RDX nanoparticles formed by RESS was characterized by X-ray diffraction using Scintag 2000 diffractometer. The X-ray pattern was recorded in the range of diffraction angle 2θ from 5° to 50° and with the step of 0.02°. Each peak in the diffraction patterns was fitted with Lorentzian function:

$$I(\theta) = I_0 + \left(\frac{2A}{\pi}\right)\left[\frac{W}{4(\theta-\theta_c)^2 + W^2}\right] \tag{6.7}$$

where I_0 is the background, A is the area of a peak, W is the full width at half maximum of peak (FWHM), and θ_c is the center of the distribution function. The integral breadth of the Lorentzian function was calculated from

$$\beta = \frac{\pi}{2} W \tag{6.8}$$

6.2.2 Results and Discussion

Figure 6.3 (a) and (b) present the X-ray diffraction patterns of RDX precursor and RDX nanoparticles produced by RESS, respectively.

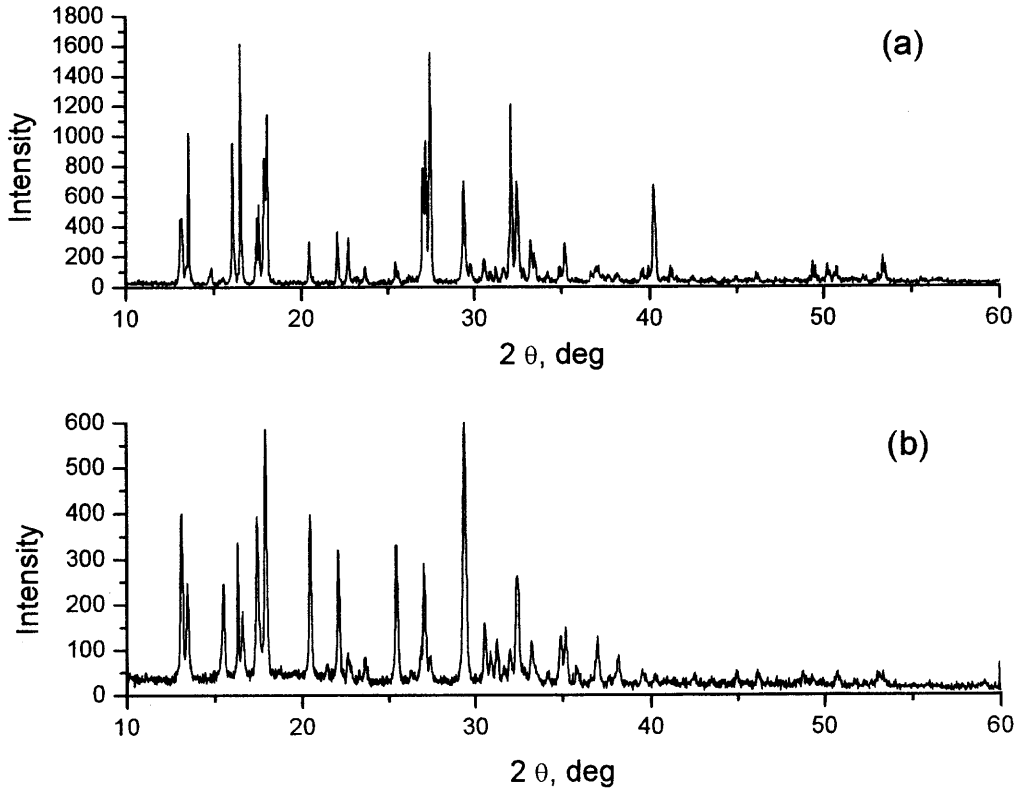

Figure 6.3 X-ray diffraction patterns of RDX crystals: (a) precursor; (b) nanoparticles prepared by RESS.

Using the patterns in Figure 6.3, the William-Hall plots were constructed for both precursor and nanoparticles (Figure 6.4). The plots were made without considering the instrument broadening.

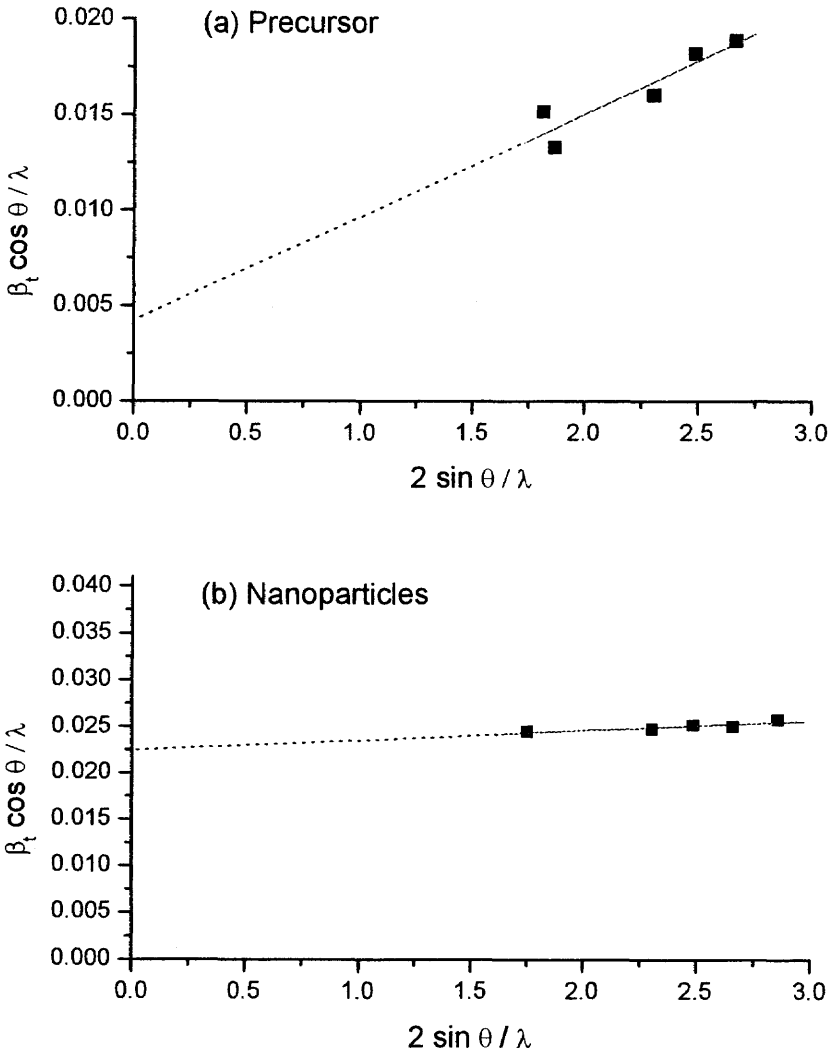

Figure 6.4 The William-Hall plot of RDX crystals: (a) precursor; (b) nanoparticles prepared by RESS.

If the instrument component of integral breadth β_{inst} is added to Equation 6.6 at θ =0, it becomes

$$\frac{\beta_t(\theta \to 0) + \beta_{inst}}{\lambda} = \frac{1}{D_v'} \tag{6.9}$$

where D_v' is the apparent volume weighted crystallite size and is determined from the extrapolation to 0 on the x-axis in Figure 6.4. Since $\frac{1}{D_v} \leq \frac{1}{D_v'}$, D_v' is the smallest number among all possible values of D_v. From Figure 6.4 (b), the apparent volume weighted crystallite size for the RDX nanoparticles $D_v'^{(RESS)}$ is 44 nm. Subtraction of Equation 6.9 for the precursor from that for the RDX nanoparticles gives

$$\frac{\beta_t^{(RESS)} - \beta_t^{(PRE)}}{\lambda} = \frac{1}{D_v'^{(RESS)}} - \frac{1}{D_v'^{(PRE)}}. \tag{6.10}$$

The left hand side of Equation 6.10 is equivalent to $\frac{1}{D_v^{(RESS)}} - \frac{1}{D_v^{(PRE)}}$.

Therefore, Equation 6.10 can be rewritten as

$$\frac{1}{D_v^{(RESS)}} - \frac{1}{D_v^{(PRE)}} = \frac{1}{D_v'^{(RESS)}} - \frac{1}{D_v'^{(PRE)}}. \tag{6.11}$$

If $D_v^{(PRE)} >> D_v^{(RESS)}$,

$$\frac{1}{D_v^{(RESS)}} \approx \frac{1}{D_v'^{(RESS)}} - \frac{1}{D_v'^{(PRE)}} = \frac{1}{D_v''^{(RESS)}} \tag{6.12}$$

where $D_v''^{(RESS)}$ is the largest size of RDX nano-crystal among all possible vales of $D_v^{(RESS)}$. Based on Figure 6.4 (b), $\frac{1}{D_v'^{(PRE)}}$ is taken as 0.01 for the maximum contribution. From the Equation 6.12, $D_v''^{(RESS)}$ was estimated as 80 nm. Based on this rough estimate, the volume weighted crystallite size of the RDX nanoparticles formed by RESS ranges

from 44 nm to 80 nm. If the shape of crystallites is assumed to be spherical, the volume weighted crystallite size (column length) D_v is related to the volume weighted crystallite diameter d_v by $d_v = 4/3D_v$. Finally the crystallite diameter range of the RDX nanoparticles is estimated as 60 nm < d_v < 110 nm. The crystallite size range covers the particle size determined by the *in situ* method in Chapter 4.

According to the size distribution functions in Figure 6.5, the majority of particles are in the size range from 100 nm to 200 nm, which is larger than the estimate from the X-ray broadening analysis.

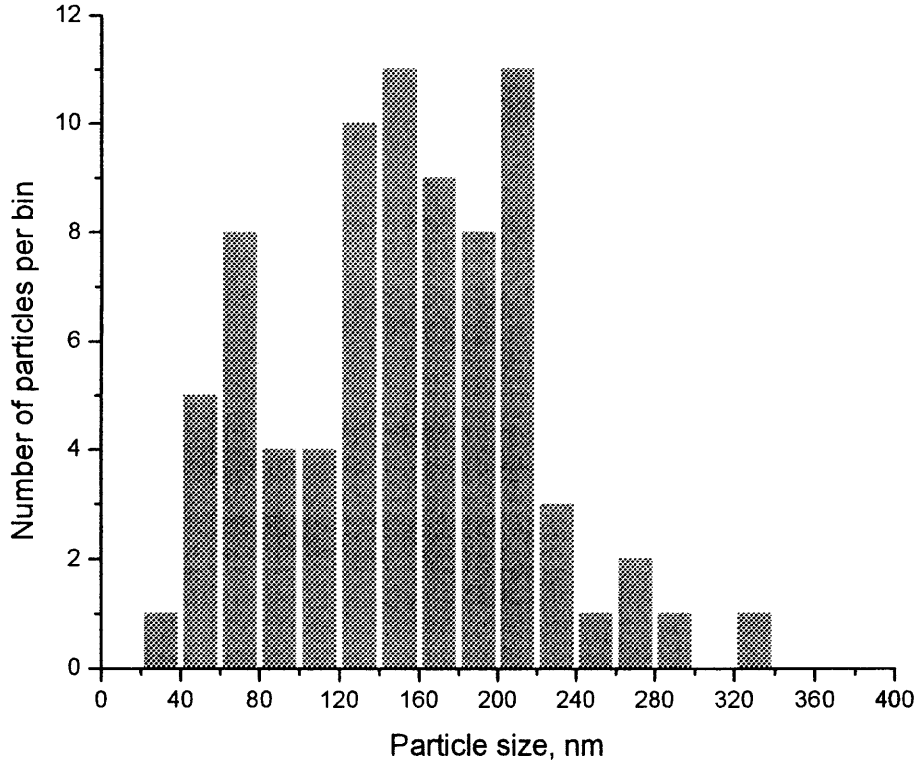

Figure 6.5 The size distribution histogram of RDX particles formed by RESS determined by the SEM images.

The difference of the results from the XRD line broadening analysis with the SEM determination could be due to the size discrimination inherent in the sampling procedure for SEM analysis. Particles below 100 nm diameter were definitely observed, but such small particles may be lost somewhere. Another possible reason for this discrepancy is that some of small particles below 100 nm agglomerate to form larger clusters as observed in the TEM image in Figure 4.18. Further TEM studies are needed to clarify the observed discrepancies.

The slopes of the straight line in Figure 6.4 give the microstrains in the crystallites as shown in Equation 6.6. There is a remarkable difference between the microstrains of the precursor materials and the nanoparticles. The root mean square strain $\varepsilon_{r.m.s}$ was calculated by $\varepsilon_{r.m.s}=(2/\pi)^{1/2}\,\varepsilon$. The $\varepsilon_{r.m.s}$ for the RDX nanoparticles and the precursor are 4×10^{-4} and 2×10^{-3}, respectively. If the surface tension of RDX is assumed to be 40 dyn/cm and the Young's modulus of RDX is taken as 18 GPa,[62] the strain induced by the surface energy of a RDX nano-crystal of 80 nm diameter is obtained using the following formula:

$$\varepsilon_s = \frac{\sigma}{E} \tag{6.13}$$

where σ is the stress due to the surface energy, and E is the Young's modulus. The stress, σ, is calculated as

$$\sigma = \frac{2\gamma}{r} \tag{6.14}$$

where γ is the surface tension of RDX, and r is the radius of a RDX crystal. The strain ε_s was calculated as 1×10^{-4}, which is four times smaller than the root mean square strain determined based on the William-Hall plot. For the large RDX precursor crystal, the

contribution of the strain due to the surface energy to the root mean square strain based on the William-Hall plot is negligibly small.

The root mean square strain in RDX nano-crystals is 5 times smaller than that in the precursor. This result shows the smaller number of crystal defects in the RDX nanoparticles formed by RESS, which might be associated with the low impact sensitivity of the RDX nanoparticles for explosion initiation.

6.3 Summary

The crystalline structure of the RDX nanoparticles was confirmed by X-ray diffraction analysis. Based on the diffraction patterns, the William-Hall plots for the RDX nanoparticles and the precursor were constructed. According to the William-Hall analysis, the crystallite size of the RDX nanoparticles formed at the pre-expansion pressure of 280 bar, the saturator temperature of 80 °C, and the nozzle temperature of 120 °C, ranged from 60 nm to 110 nm including the errors associated with the curve fitting. On the other hand, the mean particle size determined from SEM analysis of the RDX nanoparticles formed in the same RESS experiment was larger than the size range determined from the line broadening analysis of the X-ray diffraction lines. The discrepancy could be due to the sampling size discrimination for the SEM analysis. The other important conclusion derived from the William-Hall plots is that the microstrain of the RDX nano-crystals is much smaller compared to that of the precursor. This is associated with the smaller number of defects in the crystalline structure of the RDX nano-crystals.

CHAPTER 7

MECHANISM OF PARTICLE FORMATION IN RESS

7.1 Homogenous Nucleation

7.1.1 Homogeneous Nucleation Theory

Homogenous nucleation is a spontaneous nucleation occurring in supersaturated solutions. Many studies were devoted to homogeneous nucleation.[63-69] The nucleation theory predicts the nucleation rate, which is the net rate of formation of nuclei of the critical size. The simplest approach for the nucleation problem is known as the classical nucleation theory. In the classical nucleation theory, the elementary processes occurring in the nucleation process are assumed to be in the steady state by introducing the equilibrium concentration of nuclei written as[70]

$$N(n) = N_0 \exp\left[-\frac{W(n)}{kT}\right] \tag{7.1}$$

where N_0 is the normalization constant, and $W(n)$ is the reversible work required to form a nucleus containing n monomers. Using the chemical potential difference between the forming phase and metastable phase $\Delta\mu$, $W(n)$ can be written as

$$W(n) = \sigma F + n\Delta\mu \tag{7.2}$$

where σ is the surface tension, and F is the surface area of a nuclei.

However, the classical nucleation theory is not always applicable to actual nucleation events because at certain condition the steady state of nucleation is never achieved. For example, for highly supersaturated system like RESS, the critical size of nucleus would be as small as or even smaller than the size of a single molecule. In this

case the rapid condensation might occur immediately after the supersaturation created, and therefore, the classical nucleation theory cannot be used.

7.1.2 Prediction of Particle Size by Homogenous Nucleation

A numerical kinetic model for homogenous nucleation was used to predict the distribution functions and the particle size.[71] In the model, all possible reactions associated with particle formation (monomer-monomer, monomer-cluster, and cluster-cluster) as well as processes of evaporation of monomers and clusters were included. To estimate the maximum predicted particle size, all processes were assumed to be irreversible, *i.e.*, no evaporation of monomer and clusters were taken into account.

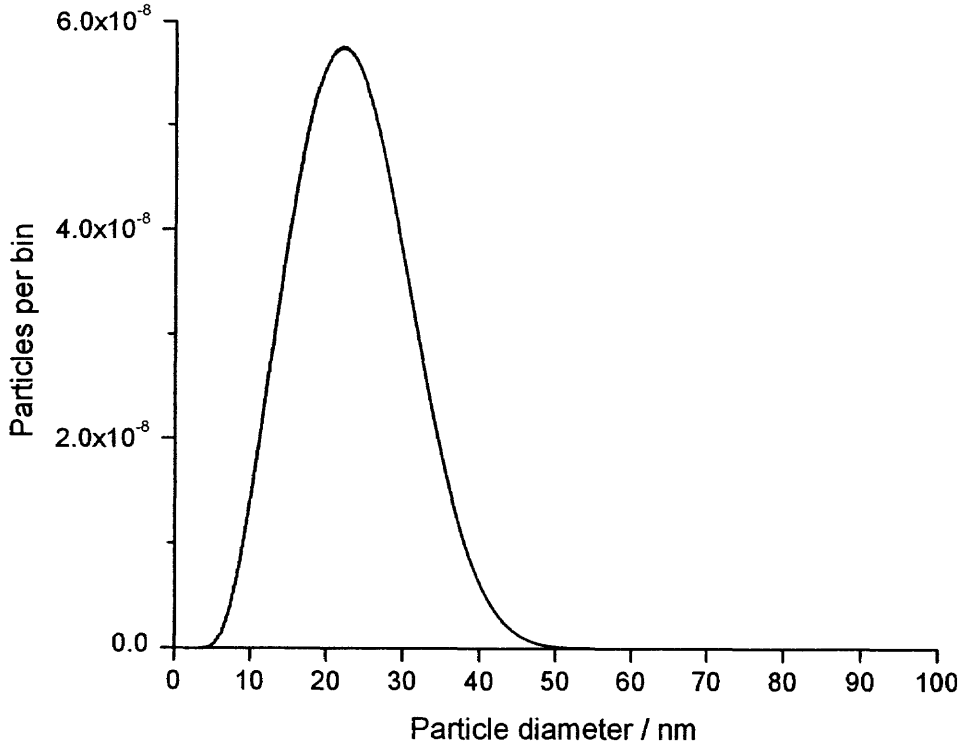

Figure 7.1 The particle size distribution function predicted by the kinetic model of homogeneous nucleation theory.

The maximum possible particle diameter of RDX calculated in this way was about 25 nm as shown in Figure B1. Obviously, the homogeneous nucleation theory cannot explain the particle formation in RESS.

7.2 Alternative Mechanism

7.2.1 Spray-drying Model

Another possible mechanism is similar to the spray-drying technique.[72,73] The spray-drying process is a very common method to produce micronized particles in food and pharmaceutical industry. The spray-drying process can be separated into two primary parts: atomization and drying. The atomization is a process of break-up of liquid solution along a stream or jet. When the jet is slow, the break-up of the liquid solution is considered to follow Rayleigh break-up mechanism.[73] In this atomization mechanism, a disturbance of circular shape of jet cross section perpendicular to the jet axis is analyzed. If the amplitude of the disturbance reaches one half of the undisturbed diameter, the break-up would occur.[73] When the jet speed is high, the atomization process depends upon the type of the flow. For instance, if the jet flow is turbulent, the break-up takes place without any external force to cause a disturbance. If the jet is a laminar flow, some external disturbance such as friction by air plays a role for the break-up. The drying process of the liquid droplet involves a heat and mass transfer of vapor. A particle starts to form when the concentration of a solute at the surface reaches the critical level, which may vary for different solute materials and liquid solvents. Because the precipitation occurs first at the surface of a droplet, a skin layer is often formed and eventually becomes a hollow particle.[74,75]

7.2.2 Tentative Mechanism Based on the Experimental Results

An RDX particle of 73 nm diameter as a final particle size has 2×10^{-18} moles of RDX if the density of RDX particles is assumed to be as the density of bulk RDX, 1.8 g/cm^3. Therefore, a single CO_2 particle of 3.3 μm diameter near the nozzle (7.5 mm from the nozzle) contains 2×10^{-18} moles of RDX assuming that a single RDX particle is produced from a single CO_2 particle. On the other hand, there are 6×10^{-13} moles of CO_2 in a single CO_2 particle of 3.3 μm diameter, if CO_2 particles are assumed to be solid with the density of 1.4 g/cm^3. Then the molar ratio of RDX to CO_2 in a 3.3 μm CO_2 particle is calculated to be 3×10^{-6}. The molar ratio in the saturated supercritical solution was also calculated from the solubility of RDX[20] in supercritical CO_2. The solubility of RDX at pressure 180 bar and temperature 80 °C was estimated as 0.035 mg/gCO_2 by interpolation of the solubility data available in the reference.[49] The molar ratio calculated based on the solubility is 7×10^{-6}, which agrees with the above estimate within a factor of three. Based on this estimate, it is speculated that initially CO_2 particles, that entrap RDX, are formed. RDX molecules also serve as nucleation centers in this mechanism.

Tentatively, the following particle formation mechanism is suggested. First, condensation of CO_2 occurs where RDX molecules serve as nucleation centers. During the condensation process, all RDX molecules which were within CO_2 volume to be condensed are entrapped in the formed particles. Therefore, the mole fraction of RDX in the particle reflects the mole fraction of RDX in the supercritical solution. Upon the subsequent evaporation of CO_2, RDX crystallizes forming particles. Essentially, this model is the spray-drying mechanism[72] in which traditional solution in a liquid solvent is replaced with a supercritical solution. According to this model, under the conditions with

lower solubility of RDX in supercritical CO_2, smaller particles are expected. The temperature and pressure dependence of RDX particle size described in Chapter 4 can be explained by this mechanism. The solubility of RDX in supercritical CO_2 increases with the pressure. Thus the particle size also increases with the pressure. At the high pressure condition RDX has the positive temperature dependence of solubility in supercritical CO_2. Therefore, the particle size increases with the saturation temperature. This is consistent with the inability to detect the final particles in the pre-expansion pressure 90 bar and 120 bar, presumably due to the smaller particle size below the sensitivity limit of the experiment.

CHAPTER 8

CONCLUSIONS

In this research, the technique for the *in situ* characterization of RDX nanoparticles formed in RESS was developed by combining laser light scattering with the imaging technique. The combination of the two techniques improved the reliability of the size distribution functions of particles formed by RESS determined by the conventional methods such as a SEM analysis or the other *in situ* methods. The *in situ* particle-by-particle treatment in the technique is the key to overcome the shortcoming of the conventional methods such as the sampling effect in the SEM analysis and the blind assumptions in the other *in situ* methods. In order to maximize the reliability of the technique developed in this research, the optical system was carefully calibrated using Rayleigh scattering from air and the scattering from the standard latex spheres. Both calibration results were in excellent agreement with each other. Moreover, the linearity of the ICCD camera was established from the Rayleigh scattering calibration.

The particle size distribution functions were determined *in situ* from the scattered intensity distribution functions. The evaluation of the scattered intensity distribution functions revealed the decrease in the particle size downstream the jet. This observation is explained as being due to the evaporation of condensed CO_2. The sizes of RDX particles at the maximum of the distribution functions were smaller than the particle size determined by the SEM analysis, which indicates the size discrimination in the sampling for the SEM analysis. The particle size obtained by the *in situ* technique was comparable

to the particle observed in the TEM image, suggesting the presence of RDX nanoparticles of the diameter around 60 nm.

The X-ray diffraction analysis for the RDX nanoparticles proved the crystalline structure. The XRD pattern of the RDX nanoparticles does not significantly differ from that of the RDX precursor. The line broadening analysis of the XRD patterns based on the William-Hall plot revealed that the size range of RDX nano-crystals is comparable with the particle size determined by the *in situ* optical method. It was also found that RDX nano-crystals have much less microstrain than the precursor. The lesser microstrain of the RDX nano-crystals could be associated with the smaller amounts of crystalline defects in the nano-crystals, which is considered to be the reason why RDX nanoparticles formed by RESS have the low impact sensitivity.

The number densities of the particles formed in the RESS jet determined by the *in situ* optical method decreased downstream the jet. The number densities corrected by the air entrainment were constant along the jet. Based on these results, it was concluded that there is no noticeable particle formation and growth associated with coagulation of RDX along the RESS jet. The data obtained do not support the homogeneous nucleation for particle formation in the RESS. The experimental results on the variation of the particle size and the number density along the jet support the concept of modified spray-drying formation mechanism for RDX particles in RESS process. The estimated molar ratio of RDX to CO_2 from the particle sizes and the number densities was consistent with the solubility of RDX in supercritical CO_2 within a factor of three.

CHAPTER 9

SUGGESTED FUTURE WORK

In this research the pressure dependence of the size of RDX particles produced by RESS was investigated up to 180 bar by the *in situ* technique and the particle size was determined only above 140 bar because of the detection limit. However, the pre-expansion pressure used in the practical condition of RESS is usually 300 bar or more. So the *in situ* characterization of RESS at higher pre-expansion pressure is more interesting in practical applications to generalize the technique as monitoring technology for particle production lines using RESS. Furthermore, the pressure dependence of the RDX particle size in the pressure range investigated is not significant enough to prove the mechanism of particle formation in RESS suggested in this research. Therefore, the characterization at high pressures where the solubility of RDX into supercritical CO_2 is significantly higher should be assessed.

Development of a new model for particle formation in RESS is suggested as a future work. It was shown in this research that the spray-drying-like process can explain the observation during RESS. However, the experimental approach is limited to the analysis at certain distances below the nozzle. Therefore, in order to understand the very initial stage of the particle formation and strengthen the speculations on the mechanism, an appropriate model correlating to the spray-drying process must be developed. The possible new model could deal with the nucleation of solute materials accompanied with heterogeneous nucleation and condensation of CO_2.

APPENDIX A

LIGHT SCATTERING FROM A SPHERE

Light scattering is a secondary radiation released from dipole oscillations in a particle induced by an incident electromagnetic wave. A time-harmonic electromagnetic field (E, H) in a homogeneous medium must satisfy the Maxwell Equations

$$\nabla \cdot \mathbf{E} = 0 \tag{A.1}$$

$$\nabla \cdot \mathbf{H} = 0 \tag{A.2}$$

$$\nabla \times \mathbf{E} = i\omega\mu\mathbf{H} \tag{A.3}$$

$$\nabla \times \mathbf{H} = -i\omega\varepsilon\mathbf{E} \tag{A.4}$$

where ε and μ are permittivity and permeability.

Based on the Equation A.1 – A.4, the vector wave equations are obtained:

$$\nabla^2\mathbf{E} + k^2\mathbf{E} = 0, \tag{A.5}$$

and

$$\nabla^2\mathbf{H} + k^2\mathbf{H} = 0, \tag{A.6}$$

where $k^2 = \omega^2\varepsilon\mu$.

In order to find the solution of vector wave equation, the following vector functions are introduced:

$$\mathbf{M} = \nabla \times (\mathbf{r}\psi), \tag{A.7}$$

and

$$\mathbf{N} = \frac{\nabla \times \mathbf{M}}{k} \tag{A.8}$$

where **r** is the radius vector in spherical coordinates and ψ is an arbitrary scalar function of position. If ψ satisfies the scalar wave function

$$\nabla^2\psi + k^2\psi = 0, \tag{A.9}$$

M and **N** satisfy the vector wave equation

$$\nabla^2\mathbf{M} + k^2\mathbf{M} = 0 \tag{A.10}$$

and

$$\nabla^2\mathbf{N} + k^2\mathbf{N} = 0. \tag{A.11}$$

The Equation A.9 can be written as in spherical coordinates,

$$\frac{1}{r^2}\frac{\partial}{\partial r}\left(r^2\frac{\partial\psi}{\partial r}\right)+\frac{1}{r^2\sin\theta}\frac{\partial}{\partial\theta}\left(\sin\theta\frac{\partial\psi}{\partial\theta}\right)+\frac{1}{r^2\sin^2\theta}\frac{\partial^2\psi}{\partial\phi^2}+k^2\psi=0. \tag{A.12}$$

In order to find **M** and **N**, Equation A.12 needs to be solved for the scalar function ψ using separation of variables $\psi(r,\theta,\phi) = R(r)\Theta(\theta)\Phi(\phi)$. Then, three separated equations are obtained

$$\frac{\partial^2\Phi}{\partial\phi^2} + m^2\Phi = 0 \tag{A.13}$$

$$\frac{1}{\sin\theta}\frac{\partial}{\partial\theta}\left(\sin\theta\frac{\partial\Theta}{\partial\theta}\right)+\left[n(n+1)-\frac{m^2}{\sin^2\theta}\right]\Theta=0 \tag{A.14}$$

$$\frac{\partial}{\partial r}\left(r^2\frac{\partial R}{\partial r}\right)+\left[k^2r^2-n(n+1)\right]R=0 \tag{A.15}$$

where m and n are separation constants. The linearly independent solutions of Equation A.13 are

$$\Phi_e = \cos m\phi \text{ and } \Phi_o = \sin m\phi, \tag{A.16}$$

where subscripts e and o denote even and odd.

The solutions of Equation A.14 are the associated Legendre functions of the first kind $P_n^m(\cos\theta)$ of degree n and order m. When $m = 0$ the associated Legendre functions are the Legendre polynomials. Introducing the dimensionless variable $\rho = kr$, the solutions of The solution of Equation A.15 are the Bessel functions of first and second kind:

$$j_n(\rho) = \sqrt{\frac{\pi}{2\rho}} J_{n+1/2}(\rho) \tag{A.17}$$

$$y_n(\rho) = \sqrt{\frac{\pi}{2\rho}} Y_{n+1/2}(\rho). \tag{A.18}$$

Then, the scalar functions are

$$\psi_e = \cos m\phi \cdot P_n^m(\cos\theta) \cdot j_n(kr) \text{ or } \cos m\phi \cdot P_n^m(\cos\theta) \cdot y_n(kr) \tag{A.19}$$

$$\psi_o = \sin m\phi \cdot P_n^m(\cos\theta) \cdot j_n(kr) \text{ or } \sin m\phi \cdot P_n^m(\cos\theta) \cdot y_n(kr), \tag{A.20}$$

where m is required to be a positive integer.

From the definition of the vector functions **M** and **N**,

$$\mathbf{M}_{emn} = -\frac{m}{\sin\theta}\sin(m\phi)P_n^m(\cos\theta)j_n(\rho)\mathbf{e}_\theta - \cos(m\phi)\frac{dP_n^m(\cos\theta)}{d\theta}j_n(\rho)\mathbf{e}_\phi, \tag{A.21}$$

$$\mathbf{M}_{omn} = \frac{m}{\sin\theta}\sin(m\phi)P_n^m(\cos\theta)j_n(\rho)\mathbf{e}_\theta - \sin(m\phi)\frac{dP_n^m(\cos\theta)}{d\theta}j_n(\rho)\mathbf{e}_\phi \tag{A.22}$$

for M, and

$$\mathbf{N}_{emn} = \frac{j_n(\rho)}{\rho}\cos(m\phi)n(n+1)P_n^m(\cos\theta)\mathbf{e}_r + \cos(m\phi)\frac{dP_n^m(\cos\theta)}{d\theta}\frac{1}{\rho}\frac{d}{d\rho}[\rho j_n(\rho)]\mathbf{e}_\theta$$
$$-m\sin(m\phi)\frac{P_n^m(\cos\theta)}{\sin(\theta)}\frac{1}{\rho}\frac{d}{d\rho}[\rho j_n(\rho)]\mathbf{e}_\phi \tag{A.23}$$

$$\mathbf{N}_{omn} = \frac{j_n(\rho)}{\rho}\sin(m\phi)n(n+1)P_n^m(\cos\theta)\mathbf{e}_r + \sin(m\phi)\frac{dP_n^m(\cos\theta)}{d\theta}\frac{1}{\rho}\frac{d}{d\rho}[\rho j_n(\rho)]\mathbf{e}_\theta$$
$$+m\cos(m\phi)\frac{P_n^m(\cos\theta)}{\sin(\theta)}\frac{1}{\rho}\frac{d}{d\rho}[\rho j_n(\rho)]\mathbf{e}_\phi \tag{A.24}$$

where the Bessel function j_n can be replaced by y_n.

Now the incoming plane wave in spherical coordinate is written as

$$\mathbf{E}_i = E_0 \exp(ikr\cos\theta)\mathbf{e}_x, \tag{A.25}$$

$$e_x = \sin\theta\cos\phi\mathbf{e}_r + \cos\theta\cos\phi\mathbf{e}_\theta - \sin\phi\mathbf{e}_\phi. \tag{A.26}$$

Expanding Equation A.25 in vector spherical harmonics,

$$\mathbf{E}_i = \sum_{m=0}^{\infty}\sum_{n=0}^{\infty}\left(B_{emn}\mathbf{M}_{emn} + B_{omn}\mathbf{M}_{omn} + A_{emn}\mathbf{N}_{emn} + A_{omn}\mathbf{N}_{omn}\right). \tag{A.27}$$

Using the orthogonality of the vector spherical harmonics of different order m, the expansion for $\mathbf{E}_i$ can be simplified as

$$\mathbf{E}_i = E_0\sum_{n=1}^{\infty} i^n \frac{2n+1}{n(n+1)}(\mathbf{M}_{o1n}^{(1)} - i\mathbf{N}_{e1n}^{(1)}), \tag{A.28}$$

noting that the coefficients B_{emn} and A_{omn} vanish for all m and n, and all coefficients with $m\neq1$ vanish. The superscript (1) denotes a radial dependence given by the spherical Bessel function of the first kind.

Now the incident field determined above is used to solve the internal and scattered fields. First, the boundary conditions must be imposed on the fields at the surface of the spheres:

$$(\mathbf{E}_i + \mathbf{E}_s - \mathbf{E}_1)\times\mathbf{e}_r = (\mathbf{H}_i + \mathbf{H}_s - \mathbf{H}_1)\times\mathbf{e}_r = 0 \tag{A.29}$$

where $\mathbf{E}_1$ and $\mathbf{H}_1$ is the internal electric and magnetic field inside the sphere, respectively. These conditions require the field components tangential to the boundary to be continuous. Because it must be finite at the origin, only jn is taken as the spherical Bessel functions in the vector harmonics inside the sphere. The boundary conditions and the form of the incident wave also require that the coefficients of the scattered and internal fields must vanish for $m\neq1$. The internal filed, then, is given as

$$\mathbf{E}_1 = \sum_{n=1}^{\infty} E_n (c_n \mathbf{M}_{o1n}^{(1)} - ib \setminus d_n \mathbf{N}_{e1n}^{(3)})$$
$$\mathbf{H}_1 = \frac{-k_1}{\omega \mu_1} \sum_{n=1}^{\infty} E_n (d_n \mathbf{M}_{e1n}^{(1)} + ic_n \mathbf{N}_{o1n}^{(1)}) \tag{A.30}$$

where $E_n = E_0 i^n (2n+1)/n(n+1)$, and c_n and d_n are coefficients to be determined. In order to treat the fields outside the sphere and simplify the functions, the spherical Hankel functions are introduced, which is defined by

$$h_n^{(1)}(x) = j_n(x) + iy_n(x)$$
$$h_n^{(2)}(x) = j_n(x) - iy_n(x) \tag{A.31}$$

Asymptotically the Hankel functions for kr >> n2 corresponding to an outgoing and incoming spherical wave are written as

$$h_n^{(1)}(kr) \rightarrow \frac{(-i)^n \exp(ikr)}{ikr}$$
$$h_n^{(2)}(kr) \rightarrow \frac{-i^n \exp(-ikr)}{ikr} \tag{A.32}$$

Then the scattered field is given by

$$\mathbf{E}_s = \sum_{n=1}^{\infty} E_n (ia_n \mathbf{N}_{e1n}^{(3)} - b_n \mathbf{M}_{o1n}^{(3)})$$
$$\mathbf{H}_s = \frac{k}{\omega \mu} \sum_{n=1}^{\infty} E_n (ib_n \mathbf{N}_{o1n}^{(3)} + a_n \mathbf{M}_{e1n}^{(3)}) \tag{A.33}$$

where the superscript (3) denotes a radial dependence given by the first Hankel function. The coefficients a_n and b_n are given by

$$a_n = \frac{\mu m^2 j_n(mx)[xj_n(x)]' - \mu_1 j_n(x)[mxj_n(mx)]'}{\mu m^2 j_n(mx)[xh_n^{(1)}(x)]' - \mu_1 h_n^{(1)}(x)[mxj_n(mx)]'}, \tag{A.34}$$

and

$$b_n = \frac{\mu_1 j_n(mx)[xj_n(x)]' - \mu j_n(x)[mxj_n(mx)]'}{\mu_1 j_n(mx)[xh_n^{(1)}(x)]' - \mu h_n^{(1)}(x)[mxj_n(mx)]'}. \tag{A.35}$$

where μ_1 is the permeability of particle, x is the size parameter and m is the relative index of refraction given by

$$x = \frac{2\pi N_1 a}{\lambda}, \text{ and } m = \frac{N_1}{N_2}. \tag{A.36}$$

N_1 and N_2 are the indices of refraction of particle and medium, respectively. a is the radius of particle.

APPENDIX B

DETERMINATION OF INDEX OF REFRACTION

B.1 Index of Refraction of Polystyrene at 248 nm

The complex index of refraction m for a non-magnetic material is given by

$$m = n + ki = \sqrt{\varepsilon_r} \tag{B.1}$$

where ε_r is the relative complex dielectric constant of the material, and n and k are the real and the imaginary parts of the index of refraction, respectively. The complex dielectric constant of polystyrene at 248 nm wavelength is $\varepsilon_r(248nm) = 3.251 + 0.260i$ as obtained from the literature data.[46] From Equation B.1, n and k are 1.803 and 0.0072, respectively. Figure B.2 presents the real and imaginary parts of dielectric constant of polystyrene as a function of photon energy.

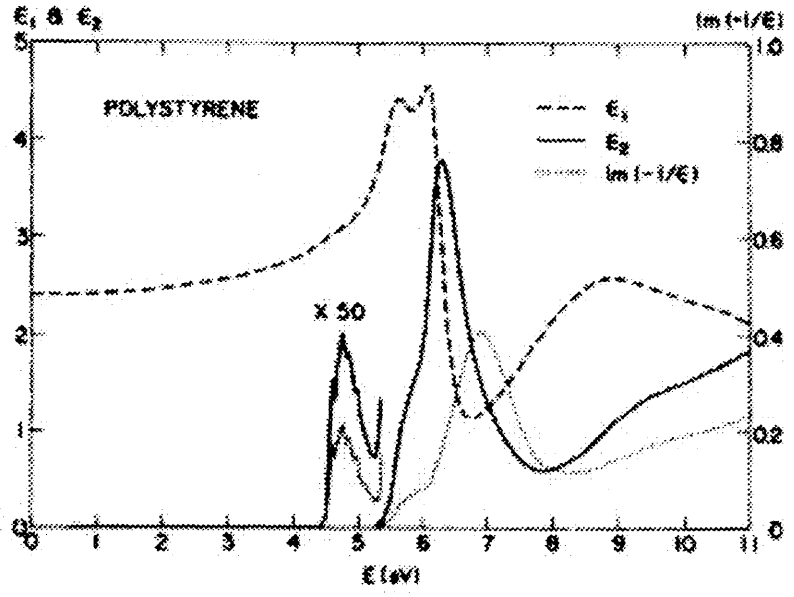

Figure B.1 The real and imaginary parts of dielectric constant of polystyrene as a function of photon energy.[46]

B.2 Index of Refraction of RDX at 248 nm

The experimentally obtained reflection spectrum of RDX measured over the wavelength range from 185 nm to 525 nm by Marinkas et al.,[76] was used as the basis of the index of refraction determination. The spectrum was fitted with the theoretical curve based on the Lorentz model with several oscillators.[77]

Using Equation B.1 the real and the imaginary indices of refraction are written as:

$$n = \sqrt{\frac{1}{2}\left(\varepsilon_r' + \sqrt{\varepsilon_r'^2 + \varepsilon_r''^2}\right)} \tag{B.2}$$

and

$$k = \frac{\varepsilon_r''}{2n} \tag{B.3}$$

where ε_r' and ε_r'' are the real and imaginary parts of the dielectric constant, respectively. According to the Lorentz model with several oscillators, the complex dielectric constant is expressed as

$$\varepsilon_r(\omega) = 1 - \sum_{j=1}^{N} \frac{f_j \omega_p^{\,2}}{\left(\omega^2 - \omega_j^{\,2}\right) + i\omega\gamma_j} \tag{B.4}$$

where N is the number of oscillators, f_j is the oscillator strength, ω_p is the plasma frequency, ω_j is the oscillator frequency (resonance frequency), and γ_j is the damping constant. In the calculations, three oscillators ($N = 3$) were used to fit the experimental data.[76] After Modifying Equation B.4, the real and imaginary parts of the dielectric constant become:

$$\varepsilon_r'(\omega) = 1 - \sum_{j=1}^{N} \frac{f_j \omega_p{}^2 \left(\omega^2 - \omega_j{}^2\right)}{\left(\omega^2 - \omega_j{}^2\right)^2 + \omega^2 \gamma_j{}^2} \tag{B.5}$$

and

$$\varepsilon_r''(\omega) = \sum_{j=1}^{N} \frac{f_j \omega_p{}^2 \omega \gamma_j}{\left(\omega^2 - \omega_j{}^2\right)^2 + \omega^2 \gamma_j{}^2}. \tag{B.6}$$

Using the real and the imaginary indices of refraction, the reflectance of the material R is given by

$$R = \frac{(n-1)^2 + k^2}{(n+1)^2 + k^2} \tag{B.7}$$

for normal incident light. From Equations B.2, B.3 and B.5 - B.7, R is expressed as a function of frequency ω . The experimental RDX reflection curve[76] was fitted using $f_j \omega_p{}^2$, ω_j, and γ_j as fitting parameters, and ω as an independent variable. Figure B.2 shows the reflection spectrum of RDX obtained experimentally and the fitting results from the optimum values of parameters: $f_1 \omega_p{}^2 = 2.05 \times 10^{-3} nm^{-2}$; $\omega_1 = 2.29 \times 10^{-2} nm^{-1}$; $f_2 \omega_p{}^2 = 8.26 \times 10^{-6} nm^{-2}$; $\omega_2 = 4.87 \times 10^{-3} nm^{-1}$; $\gamma_2 = 1.22 \times 10^{-3}$; $f_3 \omega_p{}^2 = 5.11 \times 10^{-6} nm^{-2}$; $\omega_3 = 3.95 \times 10^{-3} nm^{-1}$; $\gamma_3 = 7.28$. Using the optimum values of the parameters, the complex index of refraction of RDX at the wavelength 248 nm was calculated as $m = 1.678 + 0.645i$.

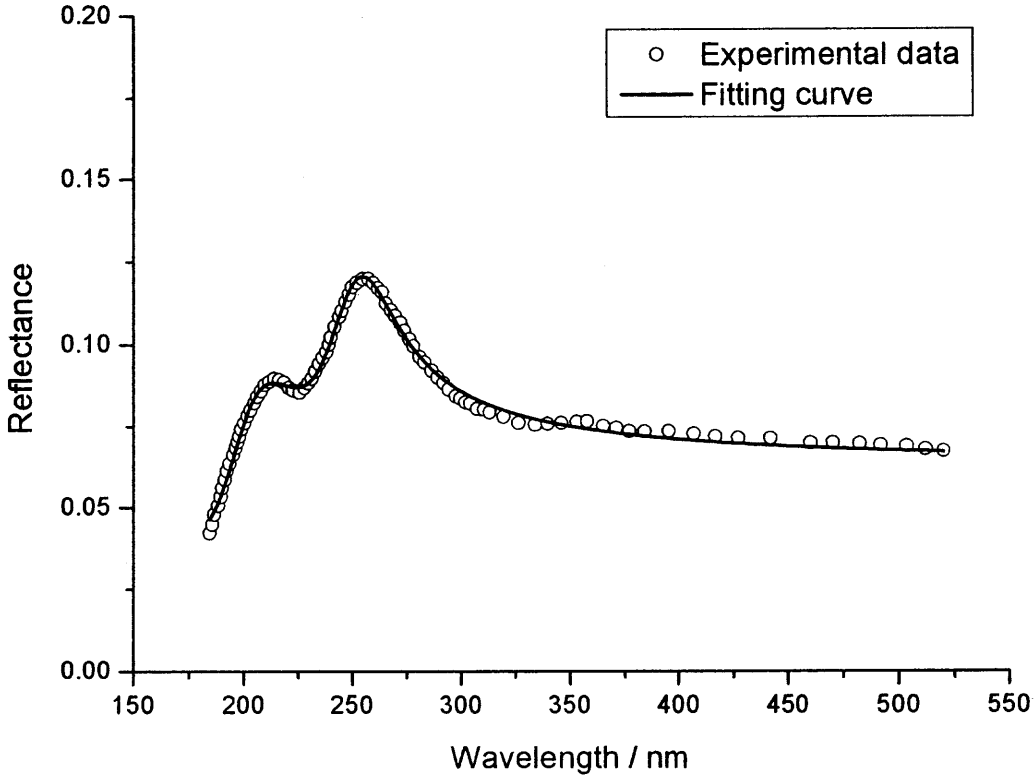

Figure B.2 Reflection spectrum of RDX obtained experimentally (open circles) and the fitting curve (solid line).

APPENDIX C

DILUTION BY AIR ENTRAINMENT ESTIMATED BASED ON TEMPERATURE PROFILES

In the derivation below, it was assumed that the entrained air has ambient temperature (298 K), and that the heat exchange by conduction can be neglected. The molar enthalpy of the mixture H at the vertical point z along the jet is given by

$$H = T(z)c_{p,mix} = T_i c_{p,CO_2} x_{CO_2} + T_0 c_{p,air} x_{air} \quad \text{(C.1)}$$

where $T(z)$, T_i, and T_0 are the temperatures of the jet, the initial temperature, and the temperature of surrounding air, respectively; $c_{p,mix}$, c_{p,CO_2}, and $c_{p,air}$ are the molar heat capacities of the mixture, CO_2, and air, respectively; x_{CO_2} and x_{air} are the molar fractions of CO_2 and air in the jet, respectively. Since the molar heat capacities, $c_{p,mix}$, c_{p,CO_2}, and $c_{p,air}$, are all approximately equal, Equation C.1 is rewritten as

$$x_{CO_2} = \frac{T_0 - T(z)}{T_0 - T_i}. \quad \text{(C.2)}$$

Equation C.2 was used to evaluate the jet dilution caused by the air entrainment based on the temperature profiles $T(z)$.

REFERENCES

[1] P. W. Cooper and S. R. Kurowski, *Introduction to the Technology of Explosives.* (Wiley-VCH, Inc, 1996).

[2] S. N. Heavens and J. E. Field, Proceedings of Royal Society of London **A338**, 77 (1974).

[3] R. W. Armstrong, C. S. Coffey, and W. L. Elban, Acta Metallurgica **30**, 2111 (1982).

[4] R. W. Armstrong, presented at the Proceedings of the Eighth International Seminar: New Trends in Research of Energetic Materials, The Czech Republic, 2005 (unpublished).

[5] U. Teipel, *Energetic materials: Particle processing and characterization.* (Wiley-VCH Verlag GmbH&Co. KGaA, Weiheim, 2005).

[6] V. Stepanov, P. Samuels, I. B. Elkina et al., presented at the 36th International ICT Conference, Karlsruhe, 2005 (unpublished).

[7] C. Domingo, E. Berends, and G. M. v. Rosmalen, Journal of Supercritical Fluids **10**, 39 (1997).

[8] H. Kröber, U. Teipei, and H. Krause, presented at the Proceedings of the 5th International Symposium on Supercritical Fluids, 2000 (unpublished).

[9] E. M. Phillips and V. J. Stella, International Journal of Pharmaceutics **94**, 1 (1993).

[10] D. W. Matson, J. L. Fulton, R. C. Petersen et al., Industrial & Engineering Chemistry Research **26**, 2298 (1987).

[11] R. C. Petersen, D. W. Matson, and R. D. Smith, Polymer Engineering Science **27**, 1693 (1987).

[12] J. Jung and M. Perrut, Journal of Supercritical Fluids **20**, 179 (2001).

[13] K. Vasukumar and A. K. Bansal, Current Research and Information on Pharmaceutical Sciences **4** (2), 8 (2003).

[14] S. M. Pourmortazavi and S. S. Hajimirsadeghi, Industrial & Engineering Chemistry Research **44**, 6523 (2005).

[15] P. M. Gallagher, M. P. Coffey, V. J. Krukonis et al., The Journal of Supercritical Fluids **5**, 130 (1992).

[16] J. Cai, Z. Zhou, and X. Deng, Chinese Journal of Chemical Engineering **9**, 258 (2001).

[17] U. Teipei, U. Förter-Barth, P. Gerber et al., Propellants, Explosives, Pyrotechnics **22**, 165 (1997).

[18] U. Teipel, Propellants, Explosives, Pyrotechnics **24**, 134 (1999).

[19] U. Teipei, H. Kröber, and H. H. Krause, Propellants, Explosives, Pyrotech **26**, 168 (2001).

[20] V. Stepanov, L. N. Krasnoperov, I. B. Elkina et al., Propellants, Explosives, Pyrotechnics **30**, 178 (2005).

[21] P. G. Debenedetti, American Institute of Chemical Engineers Journals **36** (9), 1289 (1990).

[22] X. Kwauk and P. G. Debenedetti, Journal of Aerosol Science **24** (4), 445 (1993).

[23] R. S. Mohamed, P. G. Debenedetti, and R. K. Prude'homme, American Institute of Chemical Engineers Journals **35** (2), 325 (1989).

[24] G. R. Shaub, J. F. Brennecke, and M. J. McCready, Journal of Supercritical Fluids **8** (4), 318 (1995).

[25] J. W. Tom and P. G. Debenedetti, Journal of Aerosol Science **22** (5), 555 (1991).
[26] M. Türk, Journal of Supercritical Fluids **18** (3), 169 (2000).
[27] M. Weber, L. M. Russell, and P. G. Debenedetti, Journal of Supercritical Fluids **23** (1), 65 (2002).
[28] B. Helfgen, M. Türk, and K. Schaber, Journal of Supercritical Fluids **26** (3), 225 (2003).
[29] B. Helfgen, P. Hils, C. Holzknecht et al., Journal of Aerosol Science **32**, 295 (2001).
[30] P. G. Safmann and J. S. Turner, Journal of Fluid Mechanics **1**, 16 (1956).
[31] M. B. Pinsky and A. P. Khain, Journal of Aerosol Science **28** (7), 1177 (1997).
[32] K. Oum, J. J. Harrison, C. Lee et al., Physical Chemistry Chemical Physics **5** (24), 5467 (2003).
[33] D. Hermsdorf, A. Bonnamy, M. A. Suhm et al., Physical Chemistry Chemical Physics **6** (19), 4652 (2004).
[34] A. Bonnamy, D. Hermsdorf, R. Ueberschaer et al., Review of Scientific Instruments **76**, 53904 (2005).
[35] R. B. Miles, W. R. Lempert, and J. N. Forkey, Measurement Science and Technology **12**, R33 (2001).
[36] C. F. Bohren and D. R. Huffman, *Absorption and Scattering of Light by Small Particles*. (Wiley-Interscience, New York, 1988).
[37] G. C. Stokes, Transactions of the Cambridge Philosophical Society **9**, 399 (1852).
[38] T. Wriedt, http://www.iwt-bremen.de/vt/laser/wriedt/index_ns.html.
[39] S. G. Warren, Applied Optics **25** (16), 2650 (1986).
[40] F. A. Jenkins and H. E. White, *Fundamentals of Optics*, 3 ed. (McGraw-Hill, New York, 1976).
[41] M. R. Jones, B. P. Curry, Q. Brewster et al., Applied Optics **33** (18), 4025 (1994).
[42] V. P. Maltsev and V. N. Lopatin, Applied Optics **36** (24), 6102 (1997).
[43] I. K. Ludlow and J. Everitt, Journal of Optical Society of America A **17** (12), 2229 (2000).
[44] http://www.dukescientific.com/pdfs/sales/Bul09214Web.pdf.
[45] C.-Y. Wang, S.-P. Pan, G.-S. Peng et al., in *Photon Cross Correlations Spectroscopy Publications* (Sympatec GmbH, 2006).
[46] T. Inagaki, E. T. Arakawa, R. N. Hamm et al., Physical Review B **15** (6), 3243 (1977).
[47] R. C. Weast, *CRC Handbook of Chemistry and Physics*, 57th ed. (CRC Press, 1976-1977).
[48] M. I. Mishchenko and L. D. Travis, Optics Communications **109** (1-2), 16 (1994).
[49] P. M. Agrawal, D. C. Sorescu, B. M. Rice et al., Fluid Phase Equilibria **155**, 177 (1999).
[50] P. M. Agrawal, B. M. Rice, D. C. Sorescu et al., Fluid Phase Equilibria **187-188**, 139 (2001).
[51] E. Gulari, E. Gulari, Y. Tsunashima et al., Journal of Chemical Physics **70**, 3965 (1979).
[52] J. M. Hammersley and D. C. Handscomb, *Monte Carlo Methods*. (Wiley, New York, 1964).
[53] D. M. Bates and D. G. Watts, *Nonlinear regression analysis and its applications*. (Wiley, New York, 1988).

[54] D. A. Skoog and J. J. Leary, *Principles of Instrumental Analysis*, 4 ed. (Saunders College Publishing, 1992).
[55] T. Shimanouchi, Tables of Molecular Vibrational Frequencies Consolidated Volume I, National Bureau of Standards, 1 (1972).
[56] G. Amat and M. Pimbert, Journal of Molecular Spectroscopy **16** (2), 278 (1965).
[57] P. Scherrer, Nachr. Ges. Wiss. Göttingen **2**, 98 (1918).
[58] A. R. Stokes and A. J. C. Wilson, Proceedings of the Physical Society **56**, 174 (1944).
[59] G. K. Williamson and W. H. Hall, Acta Metallica **1**, 22 (1953).
[60] W. C. McCrone, Analytical Chemistry **22** (7), 954 (1950).
[61] O. Cerclier and J. Estienne, presented at the Third Europian Powder Diffraction Conference, 1994 (unpublished).
[62] R. W. Armstrong and W. L. Elban, Materials Science and Technology **22** (4), 381 (2006).
[63] J. E. McDonald, American Journal of Physics **30**, 870 (1962).
[64] J. E. McDonald, American Journal of Physics **31**, 31 (1963).
[65] R. P. Andres, Industrial and Engineering Chemistry **57**, 24 (1965).
[66] S. K. Friedlander, *Smoke, Dust, and Haze: Fundamentals of Aerosol Behavior*. (Wiley, New York, 1977).
[67] J. L. Katz, Pure & Applied Chemistry **64** (11), 1661 (1992).
[68] J. Wölk and R. Strey, Journal of Physical Chemistry B **105**, 11683 (2001).
[69] M. I. Zeifman, J. Zhong, and D. A. Levin, presented at the Rarefied Gas Dynamics: 24th International Symposium, 2005 (unpublished).
[70] P. G. Debenedetti, *Metastable Liquids*. (Princeton University Press, Princeton, 1996).
[71] E. N. Chesnokov and L. N. Krasnoperov, Journal of Chemical Physics **126** (2007).
[72] K. Masters, *Spray drying: an introduction to principles, operational practice, and applications*, 2nd ed. (Wiley, New York, 1976).
[73] J. W. R. Marshall, *Atomization and Spray Drying*. (American Institute of Chemical Engineers, New York, 1954).
[74] J. Elversson, A. Millqvist-Fureby, G. Alderborn et al., Journal of Pharmaceutical Sciences **92** (4), 900 (2003).
[75] J. Elversson and A. Millqvist-Fureby, Journal of Pharmaceutical Sciences **94** (9), 2049 (2005).
[76] P. L. Marinkas, J. E. Mapes, D. S. Downs et al., Molecular Crystals and Liquid Crystals **35**, 15 (1976).
[77] A. B. Djurišić and B. V. Stanić, Applied Optics **37** (13), 2696 (1998).